NASA

National Aeronautics and
Space Administration

NASA CR-135428

(NASA-CR-135428) PRELIMINARY DESIGN STUDY OF AN ALTERNATE HEAT SOURCE ASSEMBLY FOR A BRAYTON ISOTOPE POWER SYSTEM Final Report, Oct. 1977 - Apr. 1978 (AiResearch Mfg. Co., Torrance, Calif.) 112 p HC A06/MF A01 G3/44

N78-28608

Unclas
27131

PRELIMINARY DESIGN STUDY OF AN ALTERNATE HEAT SOURCE ASSEMBLY FOR A BRAYTON ISOTOPE POWER SYSTEM

Final Report

May 1978

by Hal J. Strumpf

AIRESEARCH MANUFACTURING COMPANY OF CALIFORNIA
A DIVISION OF THE GARRETT CORPORATION
2525 W. 190th Street
Torrance, California 90509

Prepared for
NATIONAL AERONAUTICS AND SPACE ADMINISTRATION

Lewis Research Center
Cleveland, Ohio 44135

Contract NAS 3-20816

FOREWORD

The assistance of J. H. Dunn, the NASA Lewis Research Center project manager for this study, is gratefully acknowledged. The following AiResearch Manufacturing Company of California personnel made significant contributions to the study effort: O. Buchmann, R. Graves, J. Killackey, S. Nicastro, and H. Warren.

CONTENTS

CONTENTS (Continued)

ILLUSTRATIONS

ILLUSTRATIONS (Continued)

TABLES

TABLES (Continued)

SUMMARY

This final report presents the results of a study conducted by the AiResearch Manufacturing Company of California of the preliminary design of an alternate heat source assembly (HSA) intended for use in the Brayton isotope power system (BIPS) presently under development by the AiResearch Manufacturing Company of Arizona under a Department of Energy contract. The BIPS converts thermal energy emitted by a radioactive heat source into electrical energy by means of a closed Brayton cycle. The HSA, a major component of the BIPS, accomplishes the transfer of thermal energy from the heat source to the Brayton cycle working fluid.

The study effort involved the selection and optimization of a heat source heat exchanger (HSHX) configuration and material with enhanced reliability and fabricability as compared with the original concept. The thermal performance of the entire HSA was analyzed for various modes of system operation. Particular emphasis was placed on the predicted temperature of the iridium post-impact containment shell (PICS), the protective housing for the radioactive fuel. Required PICS temperatures were specified for the various system operating modes. Structural characteristics, including low-cycle fatigue life, natural frequencies, and dynamic loading, were analyzed for the HSA. Recommendations are made for future analytical and experimental work. A layout drawing was prepared for the HSA.

The study identified a Hastelloy X single-tube helical coil as the HSHX configuration that maximizes reliability and fabricability within the framework of the BIPS requirements. The optimized design, which met performance requirements, was a 10-turn coil made of a tube of 3.96-cm (1.56-in.) outside diameter and 3.703-cm (1.458-in.) inside diameter.

For the auxiliary cooling system, required during nonoperational phases of the BIPS, neon is the recommended fill gas. Transient startup conditions have been analyzed, and a low-cycle fatigue life of 570 cycles (well above the required 100 cycles) has been predicted for the HSHX.

PICS temperature requirements can essentially be met for all modes of operation except for the emergency cooling system, which is required to cool the heat source after a system failure. Analysis indicates that an insufficient number of insulation foils are melted to lower the PICS temperatures sufficiently.

With some minor modifications to the existing HSA structure, natural frequency and dynamic loading requirements can be met.

INTRODUCTION

This final report, submitted by the AiResearch Manufacturing Company of California (AIRLA), a division of The Garrett Corporation, describes the work accomplished under Contract NAS 3-20816 for the Lewis Research Center of the National Aeronautics and Space Administration. The study was conducted during the period of October 1977 through April 1978.

The program, entitled "Preliminary Design Study of an Alternate Heat Source Assembly for a Brayton Isotope Power System," encompassed the design of an alternate heat source assembly (HSA) intended for use on the Brayton isotope power system (BIPS) now under development by the AiResearch Manufacturing Company of Arizona (AIRPHX) under Department of Energy (DOE) contract EY76-C-03-1123. The BIPS, designed for space application, converts thermal energy emitted by a radioactive material into electrical energy by means of closed Brayton cycle. The HSA, a major component of the BIPS, accomplishes the transfer of the thermal energy from the radioactive heat source to the Brayton cycle working fluid.

A major component of the HSA is the heat source heat exchanger (HSHX). The former concept for the HSHX was a multiple-passage machined fin, constructed of a refractory columbium alloy, C-103. Part of the study consisted of designing an alternate HSHX configuration. The alternate design, a single-tube helical coil made of Hastelloy X, has replaced the C-103 machined fin as the primary HSHX design for the BIPS.

In addition to the redesign of the HSHX, the thermal and structural performance of the remainder of the HSA was analyzed for various modes of system operation. In particular, the temperature of the post-impact containment shell (PICS) was predicted to ensure compliance with DOE-imposed temperature limits. The PICS, constructed of grit-blasted iridium, is the protective housing for the radioactive fuel. The existing HSA design, exclusive of the HSHX, was utilized for this analysis. Minor modifications were recommended where applicable.

The International System of Units (SI) is used throughout this report. Most of the design and analysis was performed using customary engineering units. Conditions specified in the statement of work and the reference cycle are presented in engineering units. Conversion of these specifications to SI units may not reflect the intended accuracy. For this reason, and for manufacturing considerations, the customary engineering units also are presented in the report.

PROGRAM DESCRIPTION AND OBJECTIVES

The function of the HSA is to transfer heat from an isotope heat source (IHS) to the BIPS working fluid, a mixture of xenon and helium with a molecular weight of 83.8. The IHS is similar to the DOE multi-hundred watt heat source with an output power of 2400 W (thermal). The cylindrical IHS is surrounded by the HSHX through which the working fluid flows. Energy is received by the HSHX from the IHS by radiation and transferred to the fluid stream by forced convection. The HSHX is surrounded by the heat source insulation system (HSIS). The IHS, HSHX, and HSIS are installed inside the HSA outer container.

One of the primary goals of the study was the prediction and control of the PICS temperature during the various modes of system operation. The PICS has a maximum temperature requirement set by its rate of grain growth, which ultimately limits its impact capability. The minimum PICS temperature also must be controlled because the reduced ductility of the iridium at lower temperatures degrades the PICS impact capability. The PICS operating temperature ranges assumed for this study were taken from an Energy Research and Development Administration (ERDA-DOE) internal memo. The specified temperature are given in Table 1.

TABLE 1

DOE-SPECIFIED PICS OPERATING TEMPERATURES

Operating mode	Maximum, °C	Minimum, °C
Ground handling	1200	None
Launch and ascent (auxiliary cooling)	1200	1050
Normal operation	1200	1150
Emergency cooling transient	1600	1150
Emergency cooling steady state	1200	1150

The steady-state lower PICS temperature limit of 1150°C may be too restrictive and this requirement should probably be reviewed.

The study program was designed to meet the following objectives:

(1) Selection of an alternate HSHX configuration and material that would provide enhanced reliability and fabricability as compared with the former concept

(2) Optimization of the selected design with respect to weight, pressure drop, and working fluid outlet temperature

(3) Prediction of the performance of the HSA at steady-state reference cycle conditions, including working fluid, HSHX, and PICS temperatures

(4) Analysis of the auxiliary cooling system (ACS) mode of operation, including fill gas selection and PICS temperature prediction

(5) Evaluation of the effect of the BIPS startup transient and prediction of low-cycle fatigue (LCF) life

(6) Analysis of the HSA fueling transient

(7) Study of the emergency cooling system (ECS) operation to predict the PICS temperature excursions

(8) Resonant frequency and dynamic loading analysis of the HSA and the HSHX

(9) Preparation of a detailed layout drawing of the HSA

(10) Recommendations for future work for improvement and verification of the HSA design.

THERMAL ANALYSIS DESCRIPTION AND DISCUSSION OF RESULTS

Heat Source Assembly Thermal Model

The AIRLA general steady-state and transient thermal analyzer computer program, H0910, was utilized to perform the required thermal analysis of the HSA. The program uses the basic laws of conduction, convection, and radiation heat transfer, along with the laws of heat storage and the conservation of energy to solve problems of heat transport and storage. It employs the electrical analog technique to convert a thermal system of arbitrary complexity into a network model consisting of resistance and capacitance elements or nodes. The steady-state solutions of the thermal model are calculated by the method of successive substitution (Gauss-Seidel method), while the transient solutions are calculated by an explicit finite-difference technique. The detailed description of the program and the methods of solution are presented in appendix A. The following are some of the important features of the program:

(1) Calculates thermal resistance and capacitance from the inputs of system geometry and physical properties.

(2) Calculates the convection heat transfer coefficient from the input fluid properties and the flow characteristics.

(3) Reevaluates the fluid properties at specified time intervals based on updated film temperature.

(4) Calculates the fluid stream pressure drop.

(5) Thermal conductivity and specific heat of the material may be input as a function of node temperature.

(6) Heat sources may be input as a function of time or node temperatures.

(7) Fluid stream weight flow or fluid velocity may be input as a function of time.

A detailed thermal model of the entire HSA was set up for use with the thermal analyzer computer program. In setting up the model, each component is divided into an appropriate number of elements in each dimension, and each element is denoted by a node number. The geometric properties (length, area, etc.) and physical properties (density, specific heat, and thermal conductivity) of each element, as well as the heat transfer mechanisms (conduction, convection, and radiation) between the adjacent elements, are input to the program for calculation of the resistance-capacitance network values. The program calculates the temperature distribution and fluid pressure drop of the HSA and HSHX for the imposed boundary conditions and specific configuration.

The detailed thermal model was used for many of the analysis tasks during the study. Modifications were made, where necessary, to reflect the particular requirements of each task. The thermal model was essentially two-dimensional

with elements in the axial and radial planes of the HSA. Elements in the third dimension, the HSA circumferential plane, were added where appropriate. The models will be discussed in detail for each particular task.

Heat Source Insulation System

The HSIS is designed to limit heat losses from the HSA. The HSIS consists of Multi-Foil insulation--numerous parallel layers of a metallic foil interspaced with small particles of a refractory oxide. The foil thickness is approximately 0.013 mm (0.0005 in.), and the spacing is around 0.10 to 0.18 mm (0.004 to 0.007 in.). The oxide particles prevent adjacent layers of foil from contacting each other. The particles offer a low-conductivity thermal path, so the Multi-Foil insulation tends to exhibit the thermal conductivity of the gas between the layers. The thin metal foils are of very low resistance. The foil layers are wrapped on a mandrel outside of the HSHX.

When the space between the layers is evacuated, the conductivity path is only through the oxide particles that contact successive foil layers. Contact resistances between the particles and the foil are quite high. Radiative heat transfer between layers becomes significant. At high temperatures, the amount of heat transferred by radiation is much greater than that transferred by conduction; the Multi-Foil insulation thus resembles a series of radiation shields. At lower temperatures, both radiation and conduction are important.

In the thermal analysis, the heat transfer perpendicular to the plane of the foils is modeled as an effective radiation using the heat flux correlation developed empirically by the Thermo Electron Corporation (TECO), the manufacturer of the foils (BIPS Preliminary Design Review, AIRPHX, July 1976, p. 4.2-10).

$$\phi = \frac{1.06 \times 10^{-12} \left(T^4 - T_{SINK}^4\right)}{0.778\, N + (1.11 \times 10^{-2})\, N^2} \qquad (1)$$

where ϕ is the heat flux perpendicular to the foils, W/cm^2

T is the heat source temperature, K

T_{SINK} is the effective sink temperature seen by the last cold foil, K

N is the number of foil layers

Due to the low heat fluxes and large number of foil layers, the heat source temperature in eq. (1) can be identified with the temperature of the hottest foil and the heat sink temperature can be identified with the coldest foil with little loss of accuracy. Thus for a given number of foils:

$$\phi = \sigma F_{12} \left(T_h^4 - T_c^4\right) \qquad (2)$$

where σ is the Stefan-Boltzmann constant

T_h is the hottest foil temperature

T_c is the coldest foil temperature

F_{12} is the effective radiation exchange factor for the entire foil packet

The use of eq. (2) greatly simplifies the thermal modeling because the individual foil layers need not be divided into nodal elements. Heat transfer parallel to the plane of the foils was not modeled in the thermal analysis.

The Multi-Foil insulation for the HSA is in three separate assemblies--a cylindrical section and two planar end sections. The interface between the sections is a potential heat leak region. In most corner designs, a series of gaps exists at the intersection of the foil assemblies. These gaps act as cavities for radiation heat leak. TECO edge loss data (BIPS Preliminary Design Review, AIRPHX, July, 1976, p. 4.2-11) were utilized in the thermal model to account for the heat leakage. The data were treated in a manner similar to the perpendicular heat flux. Edge losses also were included for the insulation discontinuity in the region of the BIPS ducting. The total heat leak from the HSA can be roughly broken down as follows: 50 percent from the ends, 30 percent from the circumferential surface, and 20 percent from the insulation edges.

Configuration Study and Candidate Selection

The configuration study effort analyzed candidate HSHX designs in sufficient detail to allow comparative evaluation and selection of the configuration of greatest merit. Three basic designs were analyzed for each of two reference cycles representing a high and a low HSHX working fluid outlet temperature. The fluid outlet temperature can be identified with the turbine inlet temperature (TIT); actually there is a difference of a few degrees due to duct heat losses.

The three HSHX configurations chosen for detailed analysis were the single-tube helical coil, the helical-flow tube bank, and the axial-flow tube bank. These are shown in fig. 1. Other configurations were investigated, but not studied in detail due to what were considered to be inherent disadvantages. Some of these alternate concepts are shown in fig. 2. The multitube box manifold configuration has a large "lost area" region, where the IHS would be radiating heat directly to the HSIS. This would tend to increase the HSA heat losses and also increase the HSHX maximum wall temperature. The multitube tangential start configuration exhibits more effective use of the heat transfer surface but would seem to require a quite complex fabrication technique with an attendant reduction in reliability. The double-row configuration has a quite ineffective use of the heat transfer area; the tubes facing the IHS will tend to run considerably hotter than the tubes facing the HSIS.

Material selection.--The proposed material of construction for the high-TIT design was the refractory columbium alloy C-103. The low-TIT design specified a superalloy material. Five superalloys were considered as candidates--Hastelloy

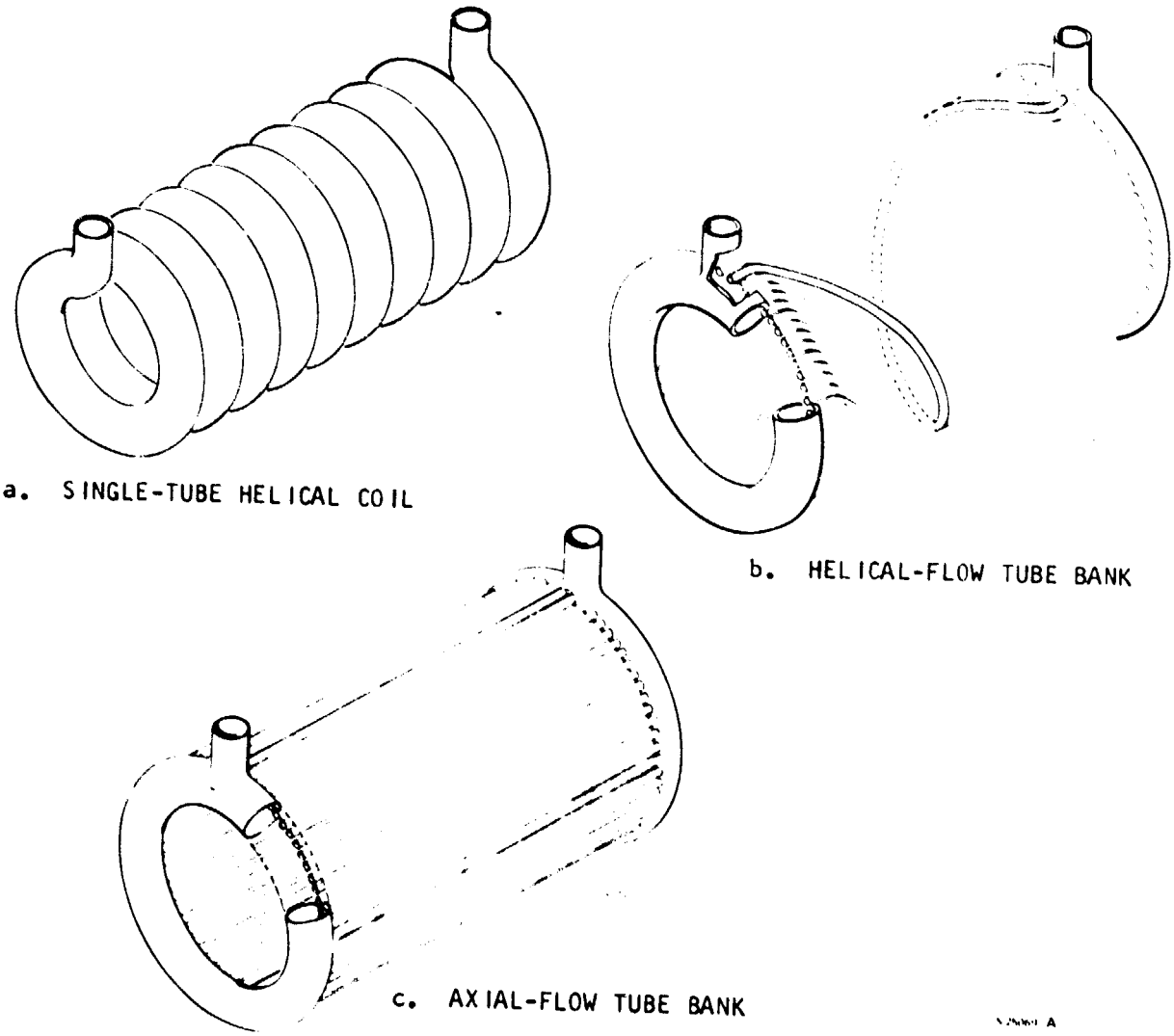

Figure 1.--Candidate HSHX Configurations.

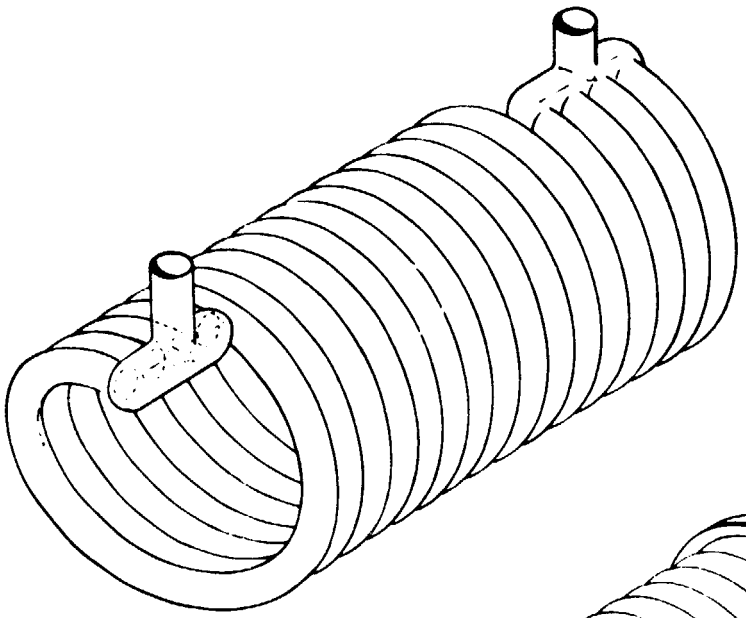

a. MULTI-TUBE WITH BOX MANIFOLDS

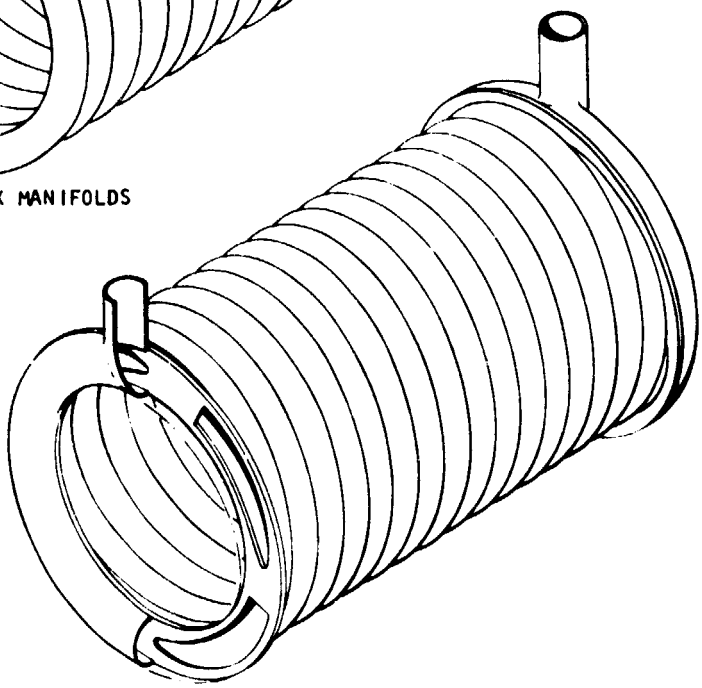

b. MULTI-TUBE WITH TANGENTIAL START

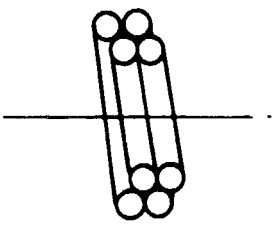

C. 4-TUBE DOUBLE ROW

S-4886-B

Figure 2.--Alternate HSHX Concepts.

X, Inconel 617, Waspaloy, Hastelloy B, and Haynes Alloy 188. Each of these wrought alloys has adequate strength, ductility, weldability, formability, and brazeability to be considered for the HSHX. The materials are discussed briefly below.

(1) Hastelloy X--A widely used nickel-base alloy. Many gas turbines use Hastelloy X as a combustor can and ducting material. It is quite fabricable and weldable and is readily available in a number of forms.

(2) Inconel 617--A relatively new alloy developed to provide high creep strength at temperatures above 815° to 870°C (1500° to 1600°F). It is a nickel-base alloy but has creep strength similar to Haynes Alloy 188, a cobalt-base alloy.

(3) Waspaloy--The only precipitation hardening alloy in the group. At temperatures of 815°C (1500°F) and below, it has substantially higher creep strength than any other alloy in the group. How well it will maintain its strength over long periods of time at the 815°C (1500°F) temperature range is unknown. Overaging may occur.

(4) Hastelloy B--Similar to Hastelloy X in terms of high-temperature strength. Its chromium content is low (1.0 percent), which indicates it may be less susceptible to loss of strength because of chromium evaporation in a high-temperature, high-vacuum environment.

(5) Haynes Alloy 188--A cobalt-base alloy that exhibits a high post-aged ductility after prolonged exposure in the 760° to 870°C (1400° to 1600°F) range. A minute addition of lanthanum to the alloy system helps to maintain a tenacious and impervious oxide film.

Table 2 presents the nominal chemical compositions of these materials.

TABLE 2

NOMINAL COMPOSITION OF SUPERALLOYS

Alloy	C	Mn	Si	Cr	Ni	Co	Mo	W	Cb	Fe	Ti	Al	Zr
Hastelloy X	0.10	0.5	0.5	22	Bal	1.5	9.0	0.6		18.5			
Inconel 617	0.07			22	Bal	12.5	9.0					1.0	
Waspaloy	0.08			19.5	Bal	13.5	4.3				3.0	1.3	.06
Hastelloy B	0.05	1.0	1.0	1.0	Bal	2.5	28			5.0			
Haynes Alloy 188	0.10	1.25	0.35	22	22	Bal		14.5		3.0	(La 0.03-0.15)		

After careful consideration of the superalloys, it was determined that Hastelloy X should be selected as the material of construction for the low-TIT case. The choice was greatly influenced by the availability of adequate

long-term creep data for Hastelloy X. The material has been used successfully for more than two decades in a variety of elevated temperature applications requiring high strength. Waspaloy represents a potentially attractive alternative exhibiting superior structural properties in the temperature range of interest. However, long-term creep data are sparse and extend for only several hundred hours. The lack of a satisfactory data base precludes further consideration of Waspaloy as an HSHX material at this time.

The HSHX will be exposed to a space vacuum during operation. Under high temperature and vacuum conditions, evaporation of the more volatile components of Hastelloy X, such as chromium, may cause subsurface porosity to develop after a period of time. Changes in surface composition can cause formation of compounds and phases that affect surface ductility and consequently fatigue resistance. Based on current knowledge of the evaporation behavior of Hastelloy X, a maximum operating temperature of 788°C (1450°F) has been specified. No maximum operating temperature is specified by the C-103 designs.

Design conditions.--The reference cycle conditions used for the configuration study are presented in table 3. As previously mentioned, separate TIT levels were used for the two HSHX materials. It should be noted that the cycle conditions are for a single HSA in a two-HSA BIPS configuration while the pressure containment requirement is for a three-HSA BIPS configuration. The working fluid is the specified BIPS Xe-He mixture with a molecular weight of 83.8. The overall axial length of the HSHX is fixed by the BIPS duct-to-duct centerline distance of 40.34 cm (15.88 in.). The assumed surface emissivities represent untreated C-103 and roughened and oxidized Hastelloy X.

TABLE 3

DESIGN POINT FOR HSHX CONFIGURATION STUDY

	C-103	Hastelloy X
Flow rate, g/s (lb/s)	44.18 (0.0974)	53.02 (0.1169)
Inlet temperature, °C (°F)	677 (1250)	----
Minimum outlet temperature, °C (°F)	871 (1600)	704 (1300)
Maximum metal temperature, °C (°F)	----	788 (1450)
Inlet pressure, MPa (psia)	0.3796 (55.05)	0.434 (63.0)
Pressure containment requirement, MPa (psia)	0.793 (115)	0.793 (115)
Pressure drop goal (0.3 percent ΔP/P), kPa (psi)	1.14 (0.165)	1.30 (0.189)
HSHX surface emissivity	0.4	0.8

Different approaches were followed in HSHX design for the two materials of construction. For the C-103, a constant fluid inlet temperature was assumed with the goal of minimizing the HSHX wall temperature. For the Hastelloy X, a maximum wall temperature was assumed with the goal of maximizing the HSHX fluid outlet temperature. It should be noted that the fluid temperature rise in the HSHX (and hence, heat transfer rate) is largely dependent on the insulation effectiveness and is relatively insensitive to the heat exchanger design. For the configuration study, the HSIS was assumed to consist of 110 layers of Multi-Foil insulation.

Axial-flow tube bank.--In the axial-flow HSHX, a series of straight tubes is located around the circumference of the IHS. Toroidal type manifolds are required, as shown in fig. 1. The inner toroidal surface has a few mm clearance around the IHS. Sufficient land is required between tubes so that they can be attached to the manifolds and maintain structural integrity. The tube separation results in a direct radiation path between the IHS and the HSIS.

The manifolds are the cause of some of the disadvantages and problems associated with this design. It is necessary to carefully size the manifolds to minimize flow maldistribution. Sizing was performed using the AIRLA manifold design computer program X1000, described in appendix B. Flow distribution considerations are discussed later in this section. The manifolds tend to use up a significant portion of the allowable working fluid pressure drop, while providing little additional heat transfer. In addition to wasting pressure drop, this situation intensifies flow distribution problems since maldistribution is closely related to the ratio of manifold pressure losses to heat exchanger core pressure drop.

The poor heat transfer conductance in the manifolds results in high manifold metal temperatures, with the outlet manifold becoming the HSHX hot spot. For the Hastelloy X design, the outlet manifold was assumed to be insulated, bringing the manifold temperature below the maximum tube wall temperature. The insulation was assumed to be 10 layers of Multi-Foil shielding.

The thermal model constructed for the axial-flow tube bank is shown in fig. 3. Only one heat exchanger tube is shown; the wall temperatures and working fluid temperatures and flows are assumed identical for all tubes. The tube shown is π radians from the duct location, at the region of lowest velocity in the manifold. Each tube is divided into two radial sections--an inner section that faces the IHS, and an outer section that faces the insulation. Fluid nodes are shown in the center of the tube and in the manifolds. The outlet manifold insulation is not shown, but is incorporated in the model for the Hastelloy X design.

Since the PICS temperatures were not investigated in the configuration study task, a simplified model of the IHS was used. The model consisted only of internal and surface nodes. The two IHS end nodes represent the laminated end crush-ups and the graphite support plates. The support plates are not physically part of the IHS.

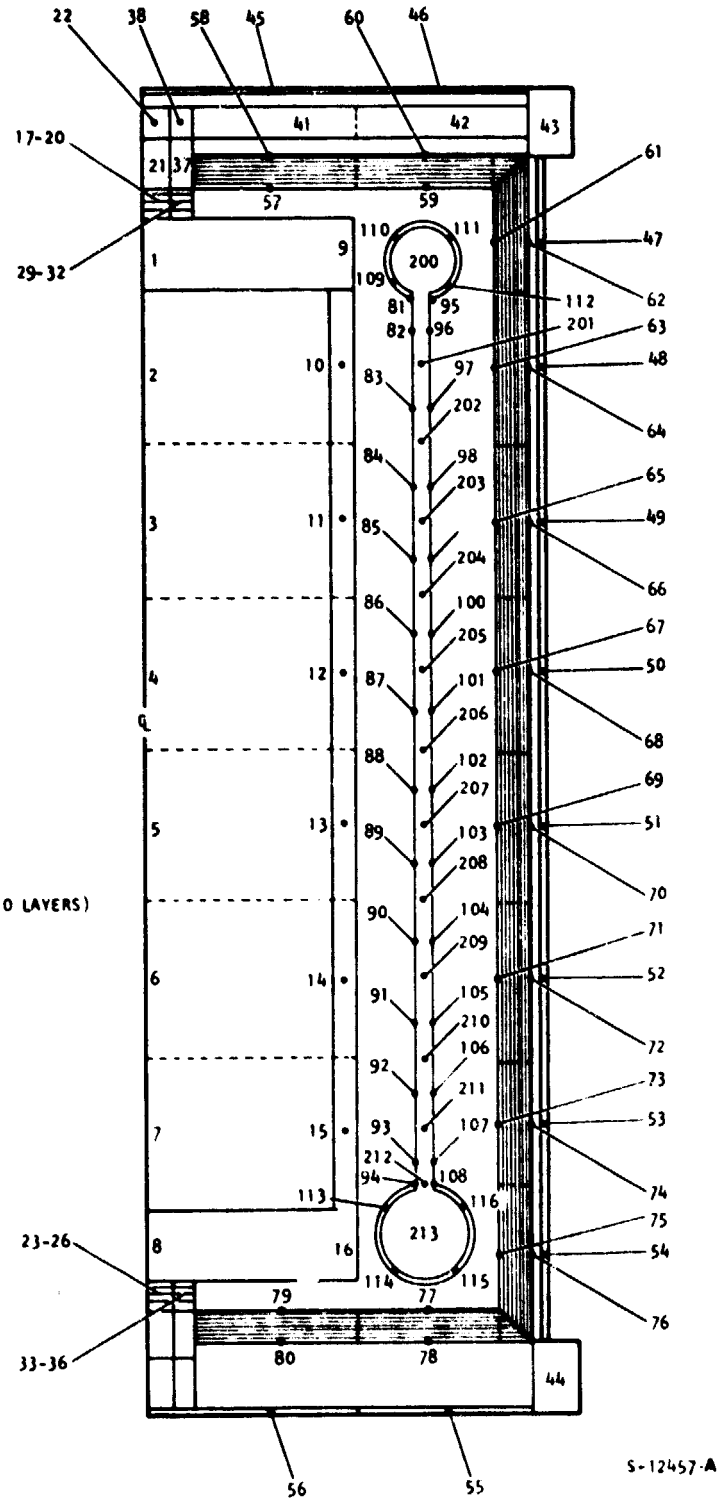

NODES	COMPONENT
1-8	HEAT SOURCE INTERNAL
9-16	GRAPHITE AERO-SHELL
17-28	"ASTRO-QUARTZ" INSULATION
29-36	ZIRCONIA END SPACERS
37-40	INCONEL X-750 PRELOAD NUT
41-42	TITANIUM SUPPORT SPIDERS
43-44	TITANIUM SUPPORT FLANGE
45-56	LOCKALLOY HOUSING
57-80	MULTI-FOIL INSULATION (110 LAYERS)
81-94	INNER HSHX SURFACE
95-108	OUTER HSHX SURFACE
109-112	INLET MANIFOLD
113-116	OUTLET MANIFOLD
200-213	Xe-He WORKING FLUID

Figure 3.--Multitube HSA Thermal Model.

Heat is transferred by radiation from the IHS to the HSHX, from the HSHX to the HSIS, and from the IHS to the HSIS through the gaps between the tubes. Radiation exchange factors were calculated for the different connections.

Heat transfer in the HSHX is characterized by conduction in the tube and manifold walls, internal radiation from the inner tube node to the outer tube node, and forced convection between the working fluid and the walls. In the manifolds, the fluid velocity decreases with circumferential distance from the entrance (inlet manifold) or exit (outlet manifold) port. Thus, the heat transfer coefficient will also decrease. The thermal model considers the location π radians from the ports, where the velocity is lowest and the heat transfer poorest. Because the fluid is almost stagnant, conduction should be the primary mode of heat transfer. This conservative approach yields the minimum fluid temperature increase and the maximum manifold wall temperature.

Pressure drop in the manifold region inlcudes losses for transitions between the connecting ducts and the manifolds, flow frictional losses in the manifolds, and turning losses between the manifolds and the heat exchanger tubes. These losses are calculated with the aid of the AIRLA manifold design computer program, X1000 (appendix B).

The heat transfer and pressure drop for the tubes are calculated by the thermal analyzer program from input values of the tube Colburn modulus and Fanning friction factor, respectively. In order to enhance the heat transfer characteristics of the axial tubes, ring dimples are assumed in the model. AIRLA has fabricated ring-dimpled tubes of various diameters and materials. The dimples are formed in the tube wall by a rolling process that changes the tube wall structure only slightly. Dimple geometry can be varied in both spacing and depth over wide ranges. A sketch of a ring-dimpled tube is shown in fig. 4. As a point of comparison, the axial tube bank ring dimple design has a Reynolds number of around 2000. At this Reynolds number, the dimpled tube Colburn modulus is about twice that of a smooth tube. Ring dimpling increases the pressure drop by a factor of about 2.7 over that for a smooth tube.

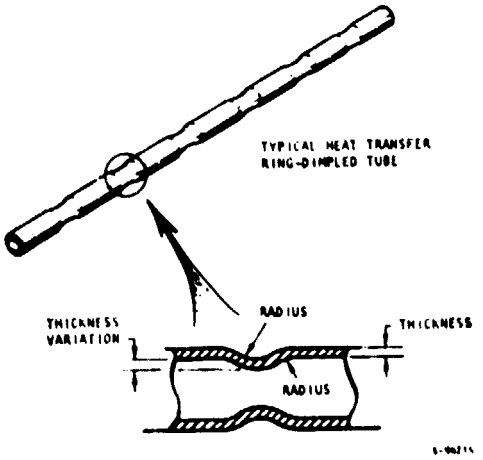

Figure 4.--Ring-Dimpled Tube Geometry.

Tables 4 and 5 summarize the semi-optimized axial-flow tube bank designs. The C-103 and Hastelloy X configurations are similar, except for the outlet manifold insulation for the Hastelloy X case. The steady-state HSA temperature profiles are shown in figs. 5 and 6 for the C-103 and Hastelloy X designs, respectively. The inner and outer surface temperatures along with the working fluid temperatures are shown for the heat exchanger. The manifold metal temperatures are shown; however, the manifold insulation temperatures for the Hastelloy X configuration are not shown. The heat exchangers consist of 83 ring-dimpled tubes, 6.35 mm (0.25 in.) in diameter. The tube and manifold wall thickness requirements were determined by a pressure containment analysis, which is discussed in the structural analysis section.

Both designs meet the fluid outlet temperature requirements of 871°C (1600°F) for the C-103 HSHX and 704°C (1300°F) for the Hastelloy X HSHX. The pressure drop goals are achieved with the manifolds using about 50 percent of the allowable.

Helical-flow tube bank.—In the helical-flow tube bank, a series of tubes is bent into a helical coil so that each tube makes exactly one complete turn around the IHS. The toroidal manifolds require space between the tubes in the manifold region for tube attachment.

If the tubes are coiled into a helix of a particular angle, however, the tubes will be in contact over most of the heat exchanger length as can be seen in fig. 1. The required angle is a function of the number of tubes used and the tube diameter-to-coil diameter ratio. With the tubes in contact, essentially all of the radiation emitted from the IHS in the radial direction is absorbed by the HSHX.

The tube curvature enhances the heat transfer and increases the pressure drop. Because the tubes are coiled, the actual flow length is considerably greater than for the straight-tube configuration. This also tends to increase both the heat transfer conductance and the pressure drop. Thus, the tube diameters are somewhat larger than for the straight tube in order to meet the pressure drop requirement.

The manifold considerations are similar to those for the straight tube bank. To attain flow uniformity by balancing the manifold areas, it is necessary for each tube to have the same relative position in both the inlet and outlet manifolds. This requires an integral number of turns. A single turn was chosen, due to the limited pressure drop allowance.

The thermal model for the helical-flow tube bank is similar to that for the axial-flow tube bank (see fig. 3). Although HSHX symmetry is not precise in the HSA circumferential direction, the temperature variation in this direction should be quite small compared to the axial temperature variation. Thus, the two-dimensional HSHX model was deemed suitable for the helical tube bank. The actual curved tube is represented by a straight tube in the thermal model; the actual tube flow length is used.

TABLE 4

AXIAL-FLOW TUBE BANK DESIGN

Number of tubes	83
Tube OD, mm (in.)	6.35 (0.25)
Dimple spacing, mm (in.)	9.53 (0.375)
Dimple depth, mm (in.)	0.38 (0.015)
Tube center-to-center spacing, mm (in.)	8.89 (0.35)
Centerline tube diameter, cm (in.)	23.5 (9.26)
Tube length, cm (in.)	36.6 (14.40)
Inlet manifold ID, mm (in.)	27.8 (1.095)
Inlet manifold wall thickness, mm (in.)	0.33 (0.013)
Outlet manifold ID, mm (in.)	41.1 (1.62)
Outlet manifold wall thickness, mm (in.)	1.40 (0.055)

TABLE 5

AXIAL-FLOW TUBE BANK PERFORMANCE

	C-103	Hastelloy X
Tube wall thickness, mm (in.)	0.254 (0.010)	0.254 (0.010)
Weight* (including manifolds), kg (lb)	3.2 (7.1)	3.0 (6.6)
Fluid inlet temperature, °C (°F)	677 (1250)	577 (1070)
Fluid outlet temperature, °C (°F)	884 (1623)	752 (1386)
Maximum tube wall temperature, °C (°F)	931 (1708)	787 (1449)
Maximum manifold temperature, °C (°F)	941 (1725)	778 (1443)
Tube pressure drop, kPa (psi)	0.538 (0.078)	0.565 (0.082)
Total pressure drop, kPa (psi)	1.14 (0.165)	1.23 (0.179)
Maximum circumferential tube gradient, °C (°F)	10 (18)	20 (36)
HSA heat loss, percent	5.2	3.7
Maximum IHS surface temperature, °C (°F)	959 (1759)	847 (1557)

*Includes a wrap-up weight of 0.45 kg (1 lb)

TEMPERATURES IN °C

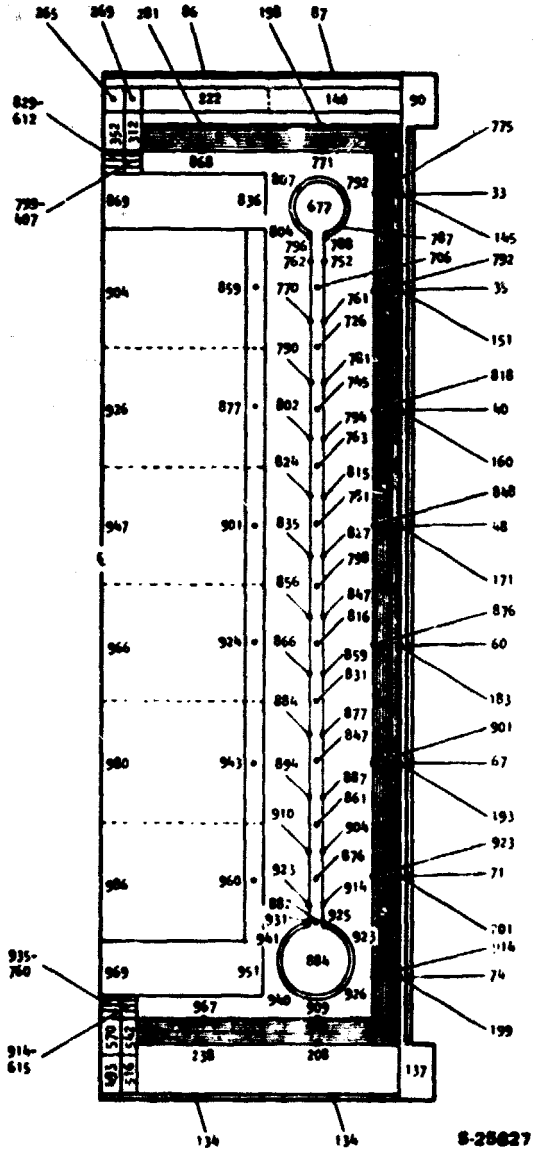

TEMPERATURES IN °R

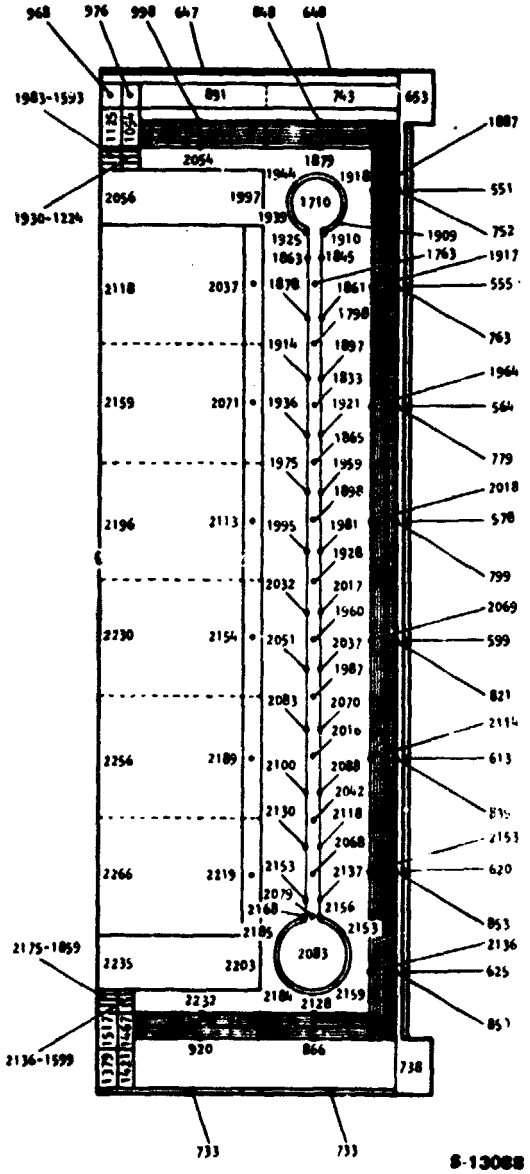

NOTES: W = 44.18 g/SEC (0.0974 LB/SEC)
P = 0.3796 MPa (55.05 PSIA)
SINK TEMPERATURE = 49°C (580°R)

S-28847

Figure 5.--C-103 Axial-Flow Tube Bank HSA Temperature Profile.

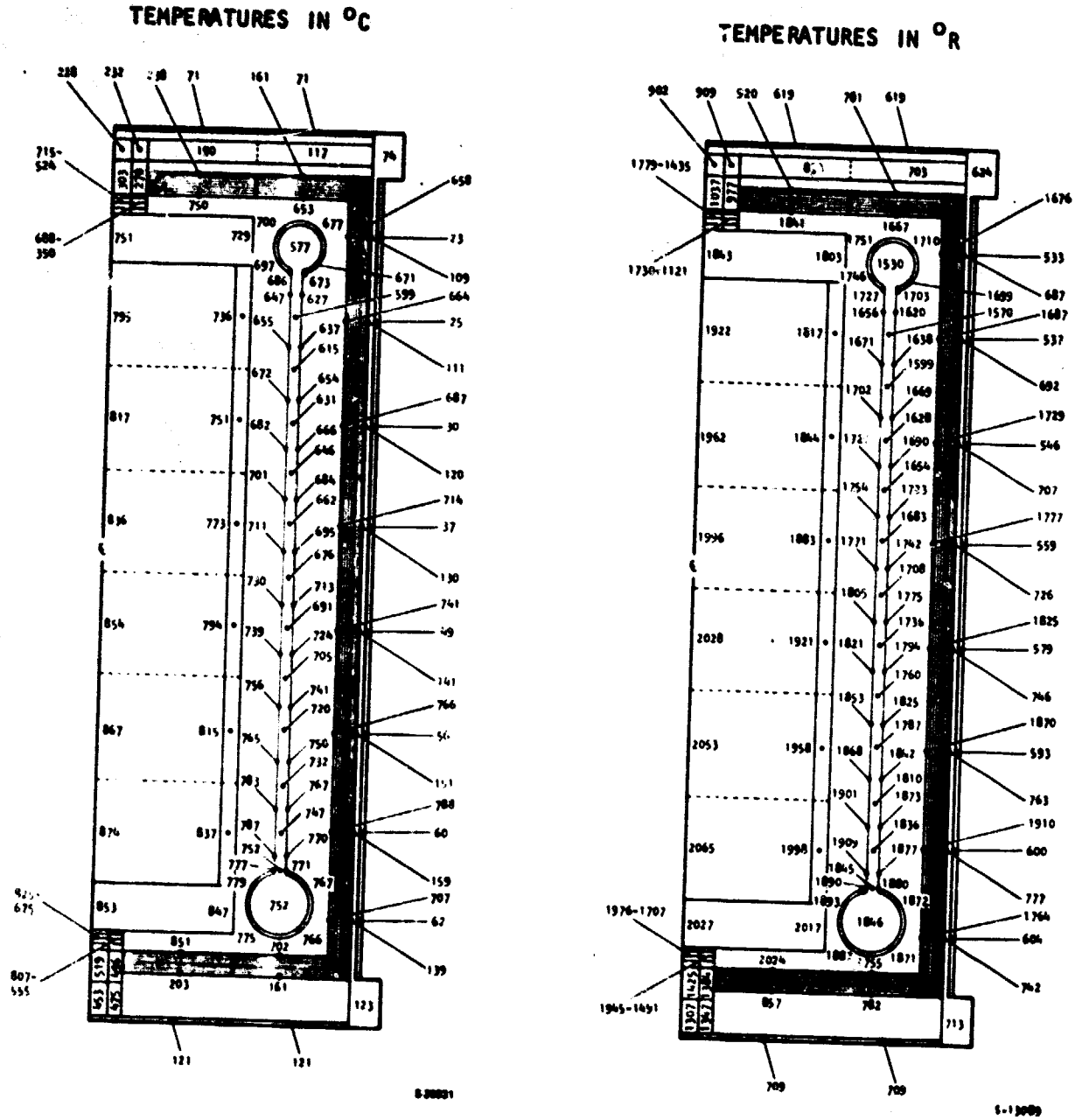

Figure 6.--Hastelloy X Axial-Flow Tube Bank HSA Temperature Profile.

For the helical tubes, the effects of tube curvature on heat transfer and pressure drop must be considered. The helical tube bank design has a Reynolds number of about 3500. This is well within the laminar flow regime since the tube curvature increases the transition Reynolds number. Srinivasan, et. al. (ref. 1) give the transition Reynolds number for helical coils, Re_t, as:

$$Re_t = 2100 \left[1 + 12 (d/D)^{0.5}\right] \tag{3}$$

where d is the tube ID, and D is the mean coil diameter. For the design curvature, the transition Reynolds number is around 6500.

For pressure drop in the laminar regime, the correlation of Kubair and Varrier (ref. 2) is used:

$$f = 0.7716 \left[\exp (3.553\ d/D)\right] Re^{-0.5} \tag{4}$$

where f is the Fanning friction factor.

As a point of comparison, at a Reynolds number of 3500, eq. (4) predicts a friction factor of 0.0146. The straight-tube friction factor at this Reynolds number is around 0.007.

For heat transfer, the theoretical analysis of Mori and Nakayama (ref. 3) for fully developed laminar flow is used. The flow is likely to be fully developed close to the inlet because the curvature aids in reducing the thermal and hydrodynamic entry length (ref. 4). The correlation is:

$$Nu/Nu_s = \frac{0.1978}{Z} Dn^{0.5} \tag{5}$$

$$Z = \frac{1}{5} \left\{ 2 + \left[\frac{10}{Pr^2} - 1 \right]^{0.5} \right\} \tag{6}$$

where Nu is the Nusselt number

Nu_s is the straight-tube Nusselt number, equal to 4.364 for uniform heat flux for fully developed laminar flow

Pr is the Prandtl number

Z is the ratio of thermal and hydrodynamic boundary layer thicknesses, equal to one for a Prandtl number of one

Dn is the Dean number given by

$$Dn = Re\ (d/D)^{0.5} \tag{7}$$

The Colburn modulus, j, is related to the Nusselt number by:

$$j = NuRe^{-1} Pr^{-1/3} \quad (8)$$

As a point of comparison, at a Reynolds number of 3500, eqs. (5) through (8) predict a Colburn modulus of 0.00347. The straight-tube Colburn modulus at this Reynolds number is around 0.0023.

Tables 6 and 7 summarize the semi-optimized helical-flow tube bank designs. The C-103 and Hastelloy X configurations are similar, except for the outlet manifold insulation for the Hastelloy X case. The steady-state HSA temperature profiles are shown in figs. 7 and 8 for the C-103 and Hastelloy X designs, respectively. A single tube of the heat exchanger is shown. For convenience, the tube is viewed straight, although the actual tube is curved and of much greater length than shown. The inner and outer surface temperatures along with the working fluid temperatures are shown for the heat exchanger. The manifold metal temperatures are shown; however, the manifold insulation temperatures for the Hastelloy X configuration are not shown. The heat exchanger designs consist of 39 tubes, 7.94 mm (0.3125 in.) in diameter, each making one turn around the IHS. A conceptual design drawing is shown in fig. 9. The tube and manifold wall thickness requirements were determined by a pressure containment analysis, which is discussed in the structural analysis section.

Both designs meet the fluid outlet temperature requirements of 871°C (1600°F) for the C-103 HSHX and 704°C (1300°F) for the Hastelloy X HSHX. The pressure drop is somewhat greater than the design goal. The manifolds use close to 50 percent of the pressure drop.

Single-tube helical coil.--In this design, a single tube is wrapped around the IHS in the shape of a tightly wound helix. The separation between successive turns of the coil is very small so that very little radiation is transferred directly from the IHS to the HSIS. The single tube has essentially no flow distribution problem and negligible manifold pressure drop. Thus, all of the pressure drop can be expended in the heat exchanger proper to yield maximum heat transfer conductance. The relatively severe tube curvature enhances the heat transfer coefficient and increases the pressure drop. See fig. 1 for a sketch of this configuration.

The HSHX manifolds are essentially extensions of the heat exchanger itself with high heat transfer conductances. Thus, the manifolds need not be insulated to meet the maximum wall temperature requirement for the Hastelloy X design.

For the single-helical-tube heat exchanger there is a significant variation in temperature profile in the circumferential direction. A modified three-dimensional model is used for thermal analysis. The IHS surface and the heat exchanger are divided into four circumferential nodes, in addition to the radial and axial nodes similar to the multitube model. The remainder of the HSA model is essentially two-dimensional and identical to the multitube configuration.

TABLE 6

HELICAL-FLOW TUBE BANK DESIGN

Number of tubes	39
Number of turns	1
Tube OD, mm (in.)	7.94 (0.3125)
Centerline coil diameter, cm (in.)	23.5 (9.26)
Total tube length, cm (in.)	83.8 (33.0)
Helix angle, radians	0.433
Inlet manifold ID, mm (in.)	27.8 (1.095)
Inlet manifold wall thickness, mm (in.)	0.36 (0.014)
Outlet manifold ID, mm (in.)	41.1 (1.62)
Outlet manifold wall thickness, mm (in.)	1.40 (0.055)

TABLE 7

HELICAL-FLOW TUBE BANK PERFORMANCE

	C-103	Hastelloy X
Tube wall thickness, mm (in.)	0.279 (0.011)	0.254 (0.010)
Weight* (including manifolds), kg (lb)	3.9 (8.5)	3.4 (7.5)
Fluid inlet temperature, °C (°F)	677 (1250)	542 (1007)
Fluid outlet temperature, °C (°F)	884 (1623)	718 (1324)
Maximum tube wall temperature, °C (°F)	951 (1744)	788 (1450)
Maximum manifold temperature, °C (°F)	958 (1757)	757 (1394)
Tube pressure drop, kPa (psi)	0.772 (0.112)	0.745 (0.108)
Total pressure drop, kPa (psi)	1.37 (0.199)	1.39 (0.201)
Maximum circumferential tube gradient, °C (°F)	25 (45)	43 (78)
HSA heat loss, percent	5.3	3.5
Maximum IHS surface temperature, °C (°F)	975 (1787)	837 (1538)

*Includes a wrap-up weight of 0.45 kg (1 lb)

TEMPERATURES IN ^{o}C

TEMPERATURES IN ^{o}R

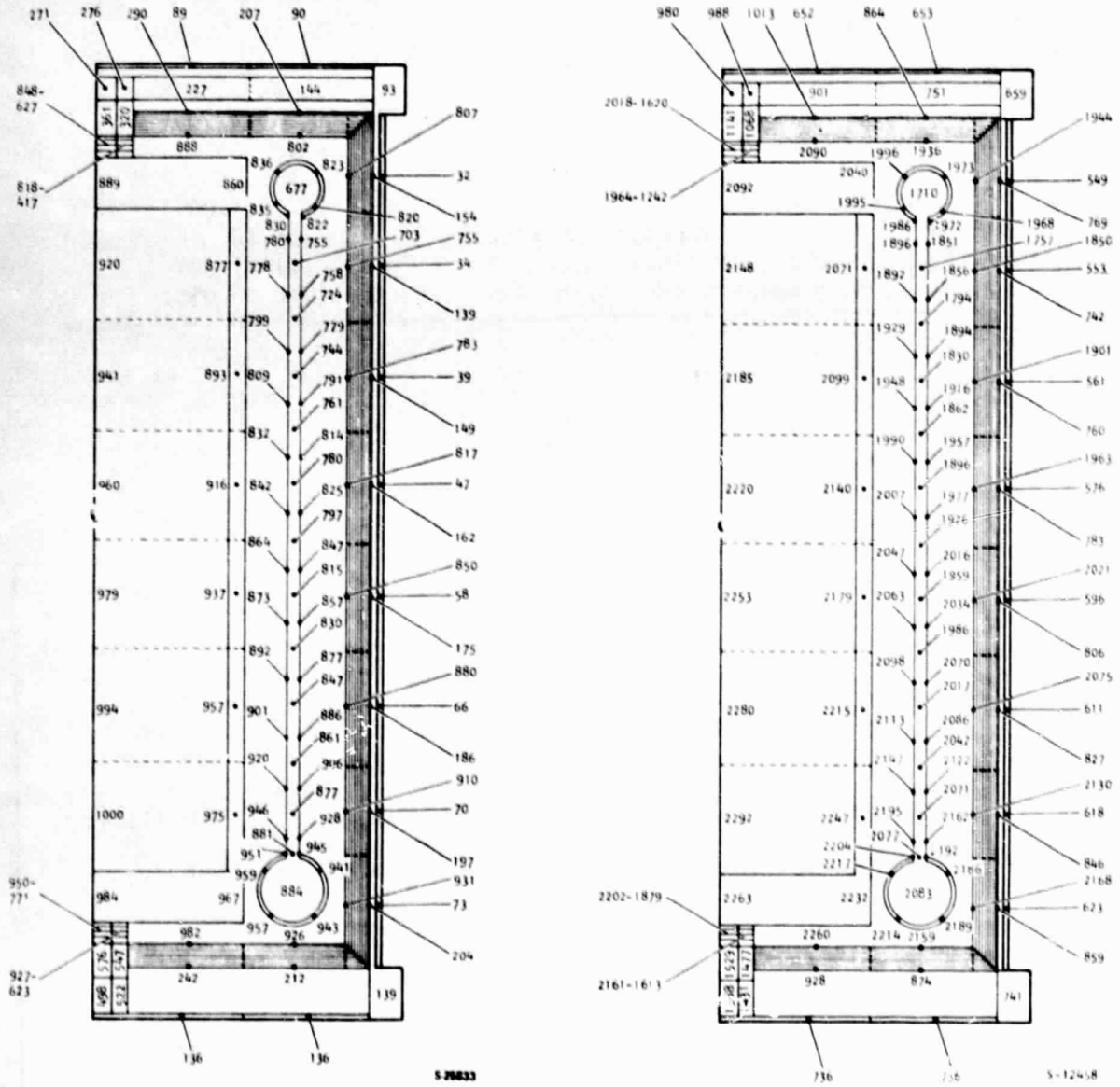

NOTES: W = 44.18 g/SEC (0.0974 LB/SEC)
P = 0.3796 MPa (55.05 PSIA)
SINK TEMPERATURE = 49°C (580°R)

S 28049

Figure 7.--C-103 Helical-Flow Tube Bank HSA Temperature Profile.

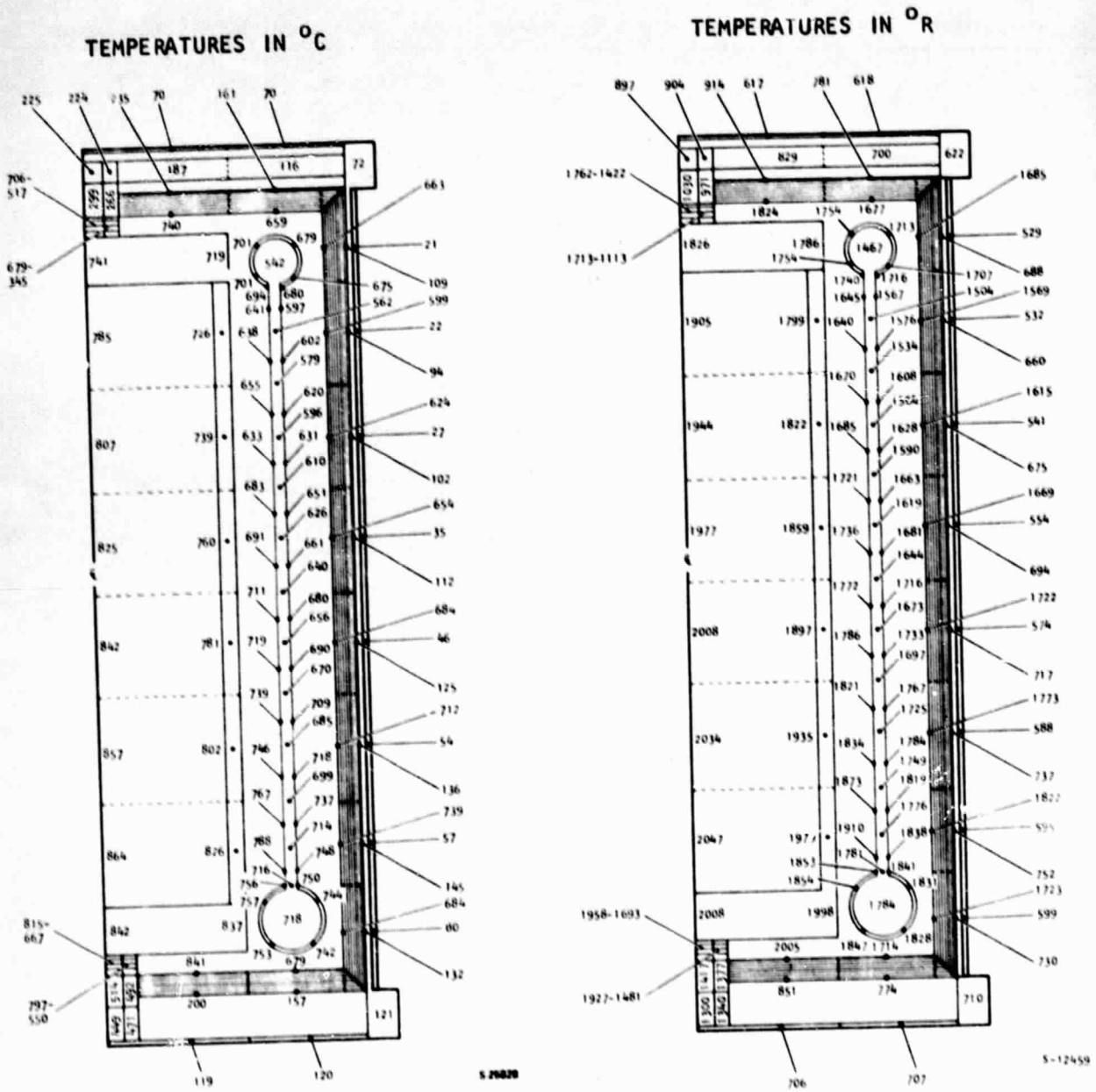

NOTES: W = 53.02 g/SEC (0.1169 LB/SEC)
P = 0.434 MPa (63.0 PSIA)
SINK TEMPERATURE = 49°C (580°R)
OUTLET MANIFOLD COVERED WITH 10 LAYERS OF MULTI-FOIL INSULATION

S 26046-A

Figure 8.--Hastelloy X Helical-Flow Tube Bank HSA Temperature Profile.

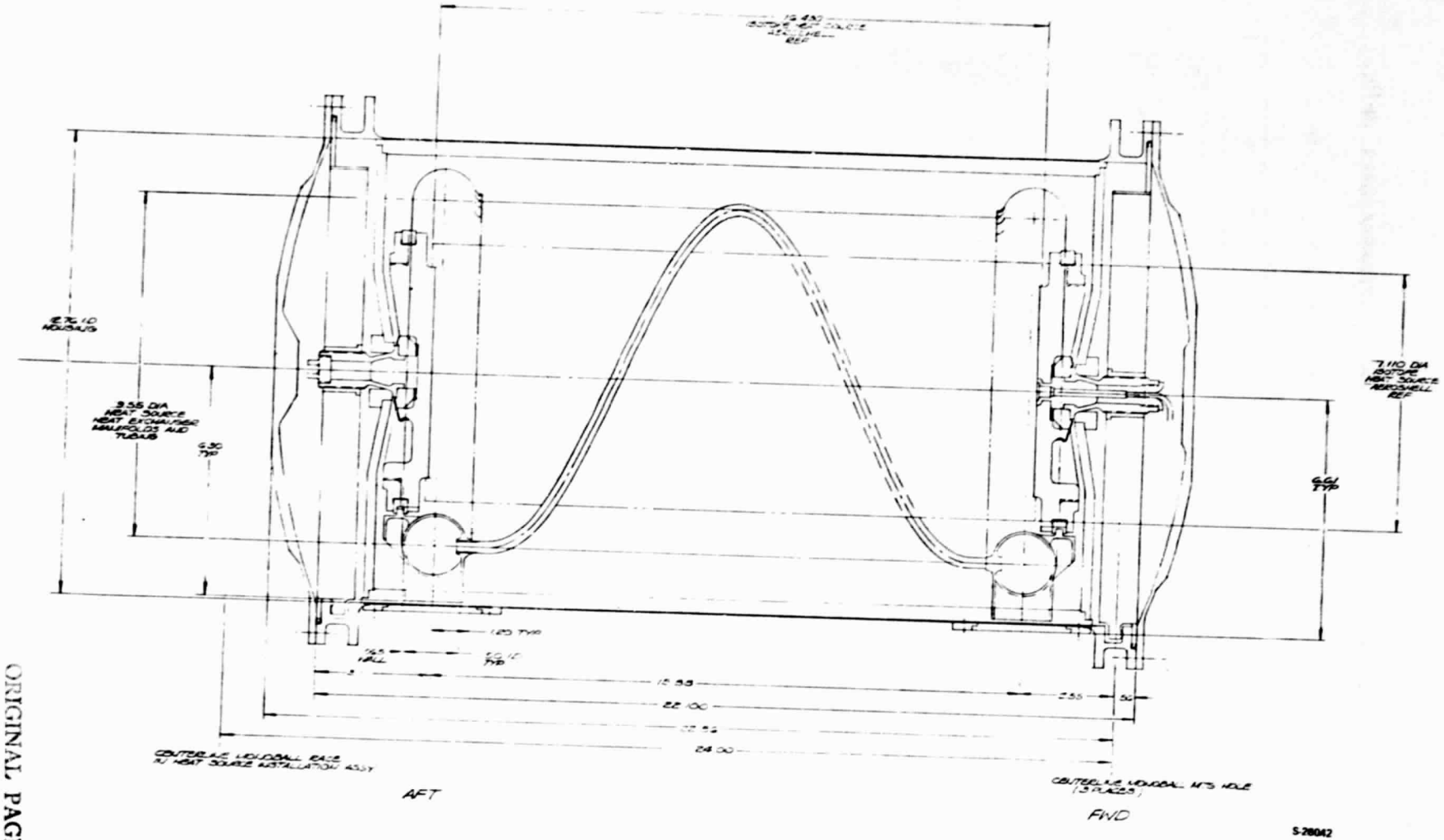

Figure 9.--Helical-Flow Tube Bank Heat Source Assembly.

After some preliminary study, a helical coil with 10 turns was selected as the most promising design. The thermal model constructed for the configuration study is shown in fig. 10. The 10 turns of the helical coil are represented by 10 toroids of circular cross section divided into four quadrants. Each quadrant is divided into two radial sections--an inner section that faces the heat source and an outer section that faces the insulation. Within each turn, the nodes listed first are for the inner heat transfer surface, the nodes listed next are for the working fluid, and the final nodes are for the outer heat transfer surface.

The heat transfer resistive paths are set up in a manner analogous to that previously described for the multitube models. The short manifold sections are considered to be part of the heat exchanger tube. The Reynolds number in the tube is quite high (above 25 000) so the flow regime is definitely turbulent. For pressure drop, the correlation of Ito (ref. 5) is used:

$$f = 0.079\ (d/D)^{0.1}\ Re^{-0.2} \tag{9}$$

At a Reynolds number of 25 000, eq. (9) predicts a friction factor about 35 percent greater than that for a straight tube.

For heat transfer, the correlation of Seban and McLaughlin (ref. 4) is used:

$$Nu = 0.023\ Re^{0.85}\ Pr^{0.4}\ (d/D)^{0.1} \tag{10}$$

At a Reynolds number of 25 000, eqs. (10) and (8) predict a Colburn modulus about 30 percent greater than for a straight tube.

Tables 8 and 9 summarize the semi-optimized single-tube helical coil design. The C-103 and Hastelloy X configurations are similar. The steady-state HSA temperature profiles are shown in figs. 11 and 12 for the C-103 and Hastelloy X designs, respectively. The temperatures listed for each turn represent the ranges within the coil; the working fluid is heated as it flows around the turn. In each turn, the first temperatures listed are for the inner heat transfer surface (facing the IHS), the next temperatures are for the working fluid, and the final temperatures are for the outer heat transfer surface (facing the HSIS). The heat exchangers consist of a single coiled tube of 43.18 mm (1.70 in.) diameter. The tube wall thickness requirements were determined by a pressure containment analysis, which is discussed in the structural analysis section.

Both designs meet the fluid outlet temperature requirements of 871°C (1600°F) for the C-103 HSHX and 704°C (1300°F) for the Hastelloy X HSHX. The pressure drop goals are met.

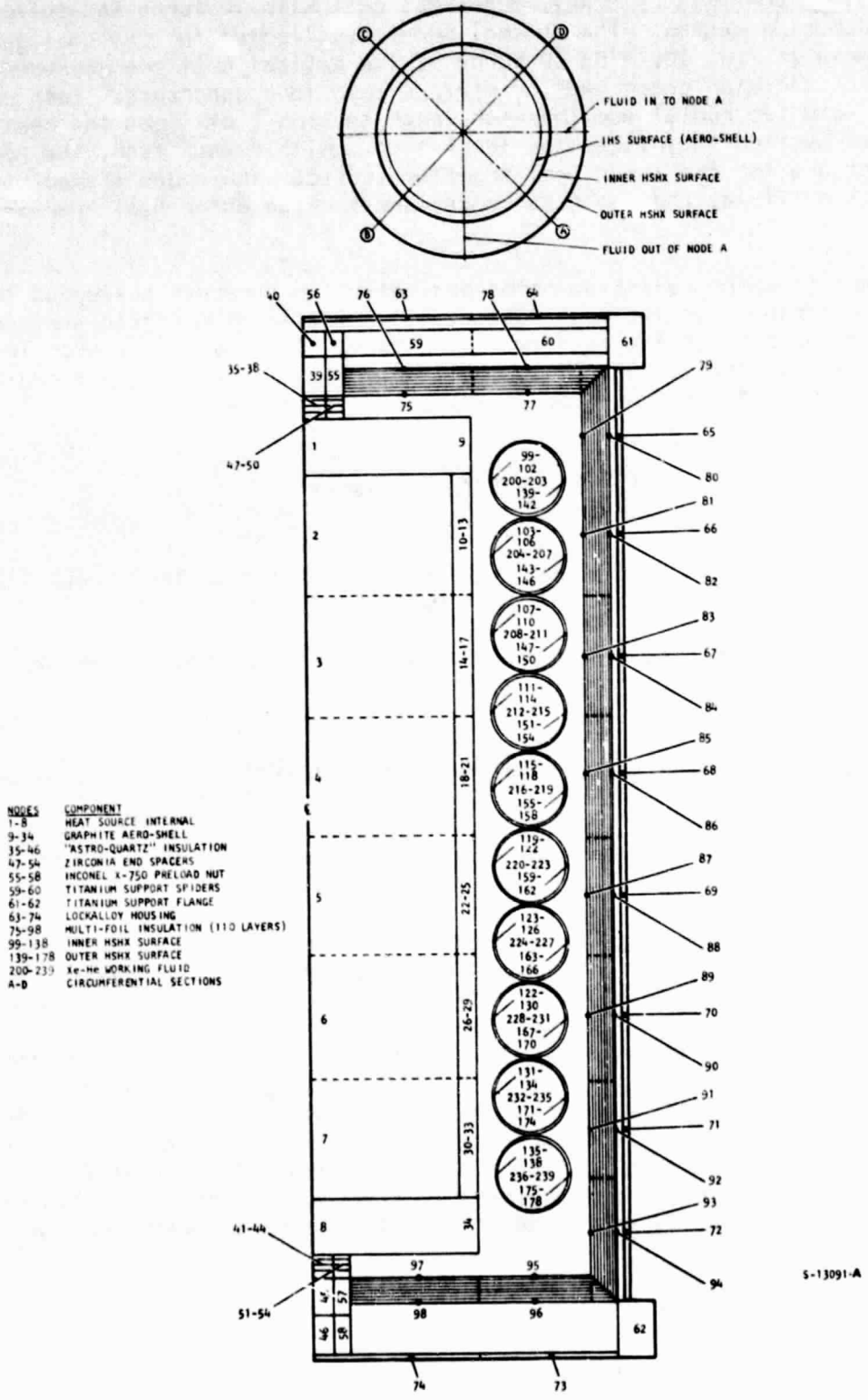

Figure 10.--Single-Tube Helical Coil HSA Thermal Model.

TABLE 8

SINGLE-TUBE HELICAL COIL DESIGN

Number of turns	10
Tube OD, mm (in.)	43.18 (1.70)
Centerline coil diameter, cm (in.)	23.9 (9.41)
Total tube length, cm (in.)	762 (300)

TABLE 9

SINGLE-TUBE HELICAL COIL PERFORMANCE

	C-103	Hastelloy X
Tube wall thickness, mm (in.)	1.09 (0.043)	1.35 (0.053)
Tube weight, kg (lb)	9.75 (21.5)	11.1 (24.4)
Fluid inlet temperature, °C (°F)	677 (1250)	578 (1073)
Fluid outlet temperature, °C (°F)	886 (1626)	754 (1390)
Pressure drop, kPa (psi)	1.13 (0.164)	1.21 (0.175)
Maximum metal temperature, °C (°F)	916 (1680)	786 (1447)
Maximum circumferential tube gradient, °C (°F)	52 (93)	56 (101)
HSA heat loss, percent	4.6	3.4
Maximum IHS surface temperature, °C (°F)	960 (1760)	824 (1515)

TEMPERATURES IN ^{o}C

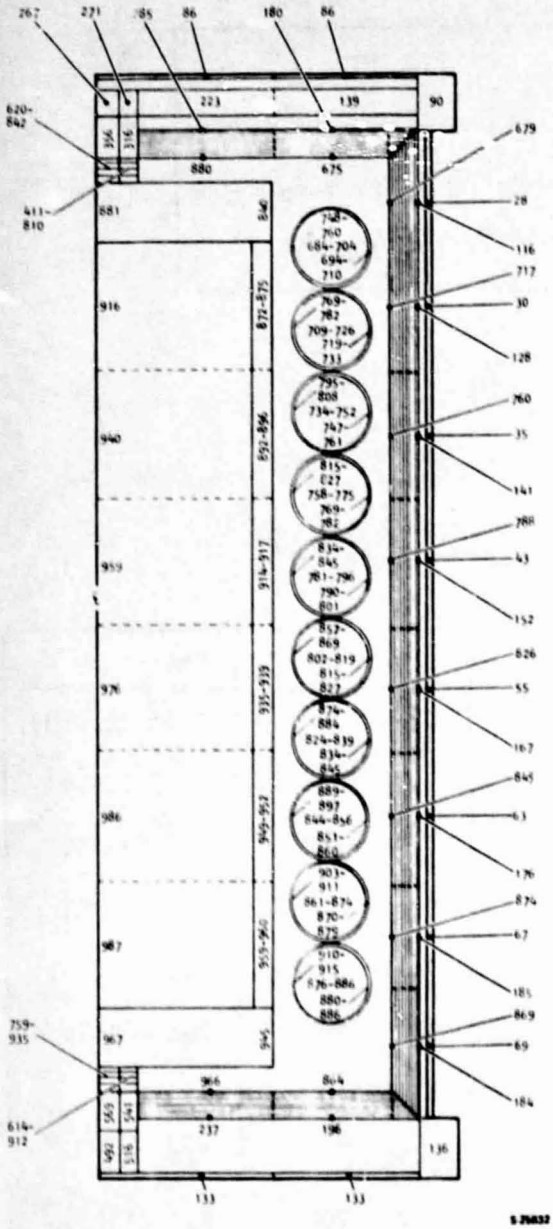

TEMPERATURE IN ^{o}R

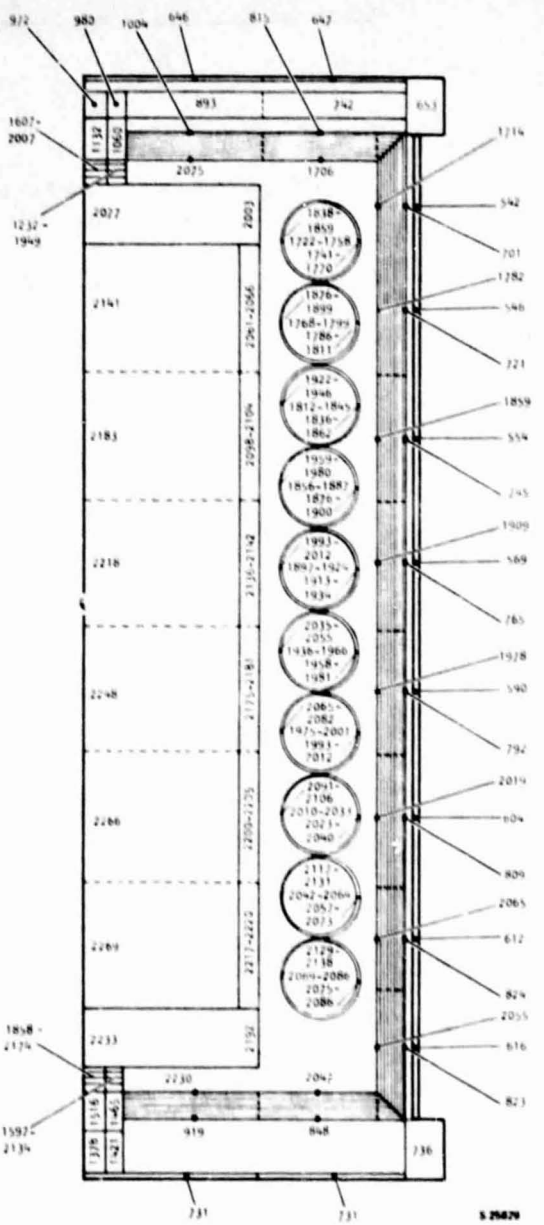

NOTES: W = 44.18 g/SEC (0.0974 LB/SEC)
P = 0.3796 MPa (55.05 PSIA)
Tin = 677°C (1710°R)
SINK TEMPERATURE = 49°C (580°R)

S 26050

Figure 11.--C-103 Single-Tube Helical Coil HSA Temperature Profile.

ORIGINAL PAGE IS
OF POOR QUALITY

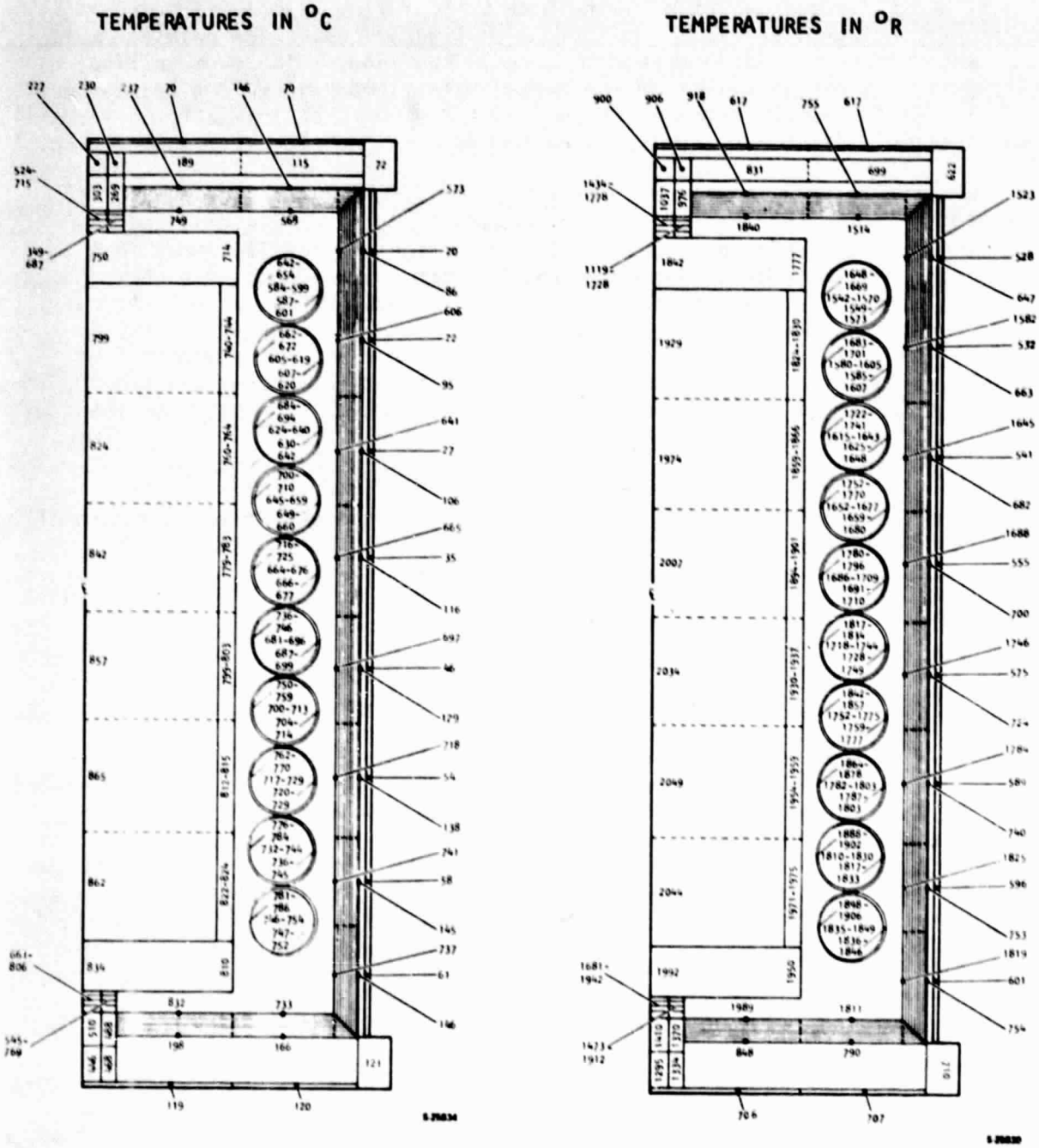

Figure 12.--Hasteiloy X Single-Tube Helical Coil HSA Temperature Profile.

Flow distribution.--The attainment of uniform flow distribution is an important consideration for the multitube configurations. Flow maldistribution will result in higher surface temperatures in the tubes with low mass flow. In addition to the direct effect of the higher metal temperature, the thermal gradients will be increased, thereby influencing the structural integrity of the unit. Also, flow maldistribution may cause an increase in the overall pressure drop.

The flow distribution is controlled by the flow areas of the manifolds. This is illustrated in the following discussion. Consider fig. 13, which shows typical heat exchanger manifold configurations. Fig. 13a shows that all elements of the flow stream experience a common pressure at the heat exchanger inlet, P_1, and a common pressure at the heat exchanger outlet, P_2. Consequently, the pressure loss through all flow streams must be identical, i.e., $P_1 - P_2$. If two flow paths have different resistance characteristics the flow is apportioned as necessary to balance the overall pressure drop. Thus, in fig. 13a, the remote path A will receive a smaller portion of the total flow than the more direct path B.

Pressure losses fall into two categories: (1) frictional (or viscous shear) and (2) kinetic energy. In practical heat exchanger design, frictional losses are usually predominant in the core (or heat transfer matrix) and kinetic energy losses predominate in the manifolds; however, all losses must be considered for optimum design. As a general design guideline, reasonably uniform flow distribution can be achieved by designing manifolds such that their loss characteristics are low, relative to the frictional loss characteristics of the core. The disadvantage of this is that for some configurations, the physical size of the manifolds must be larger than would be the case if detailed analysis were applied. Consider, for example, cases in which the orientation of supply and discharge lines must be perpendicular, rather than parallel, to the direction of the flow through the heat exchanger core. Typical examples are shown in fig. 13b. In both of these cases, the cross-sectional manifold area available for distribution of the flow is proportional to the small dimension Y rather than, as in the case of parallel supply and discharge, the large dimension X. Since both frictional and kinetic energy losses are proportional to the square of the flow stream velocity, this has a profound effect on the manifold losses. Unless core frictional losses are very high, the configuration shown in fig. 13b is inherently inferior to that shown in fig. 13a.

In comparing the configurations of fig. 13b, the initial impression is that distribution of the Z-flow configuration is superior to that of the U-flow, because of the latter's disparity with respect to the ratio of extreme flow path lengths. In Z-flow, all flow streams have the same path length. In fact, however, U-flow is superior to Z-flow. This is due to a factor heretofore neglected, i.e., the conversion of velocity pressure to static pressure. It is observed in fig. 13 that the inlet velocity pressure acts in the direction of core flow; it is therefore available to assist the circulation directly.

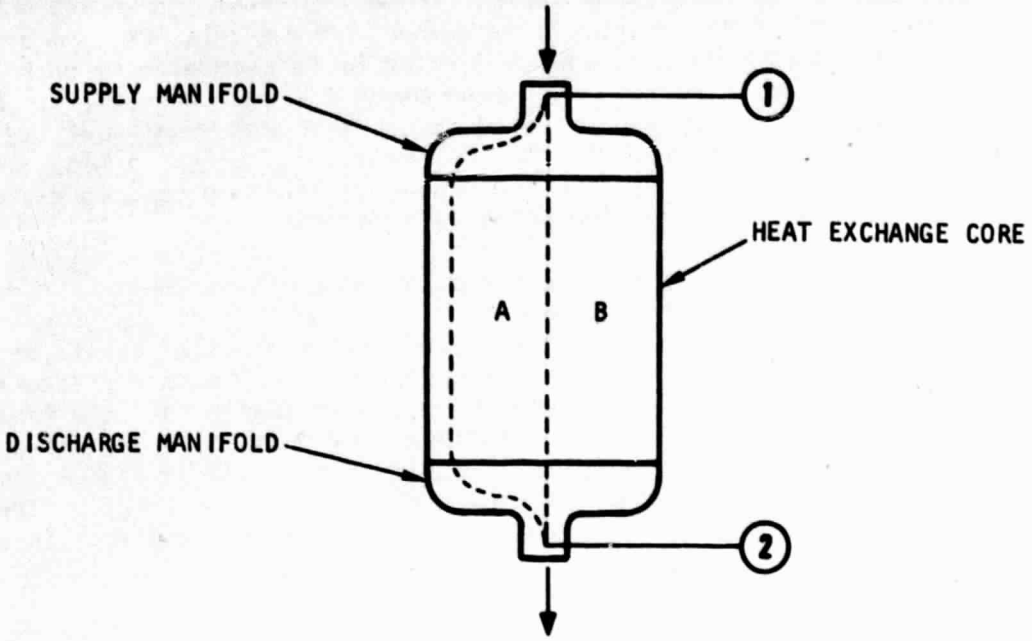

a. DIRECT AND REMOTE FLOW PATHS THROUGH A HEAT EXCHANGER WITH CENTRALLY LOCATED SUPPLY AND DISCHARGE LINES

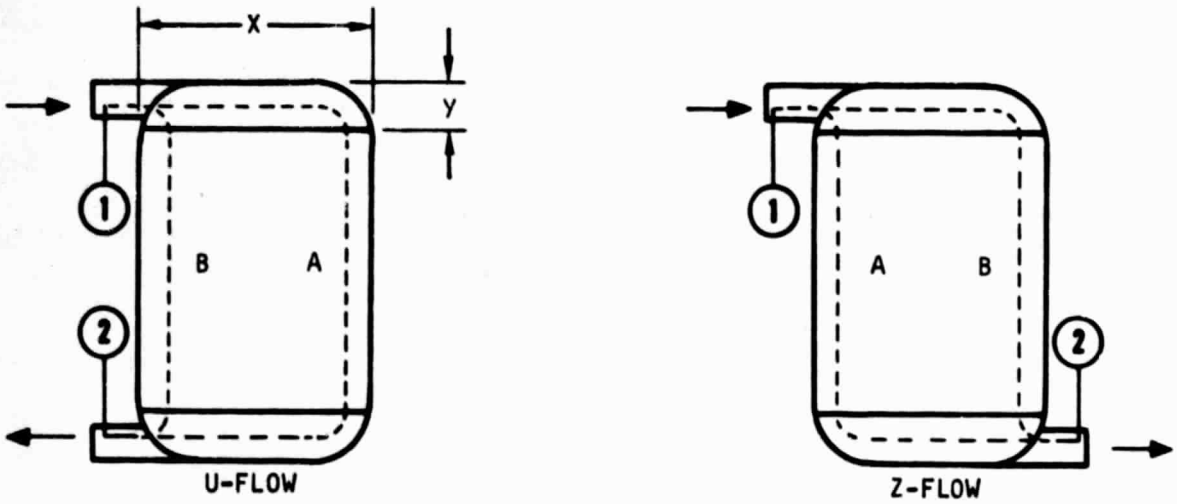

b. DIRECT AND REMOTE FLOW PATHS THROUGH HEAT EXCHANGERS WITH PERIPHERALLY LOCATED SUPPLY AND DISCHARGE LINES

S-4906

Figure 13.--Typical Heat Exchanger Manifold Configurations.

In fig. 13b, the inlet velocity pressures act normal to core flow in such a manner that a portion of the energy is lost in eddy currents generated in turning the flow. Some of the energy is recovered, however, in the form of static pressure gain as the lateral manifold velocity is decreased by core pickoff along the lateral traverse. This phenomenon follows Bernoulli's Law: as the supply manifold velocity is decreased across the core, the local static pressure is increased accordingly. For the U-flow configuration, a similar static pressure profile is generated in the discharge manifold by progressive acceleration of the flow stream in the opposite direction.

Typical pressure profiles for uniform flow for the U-flow configuration are shown in fig. 14a as a function of manifold flow length. It can be seen that the pressure profiles are identical for the inlet and outlet manifolds; the profiles are displaced by a constant pressure equal to the core pressure drop. The static pressure change from the inlet of the supply manifold to the outlet of the discharge manifold is equal to this core pressure drop. In order to attain the identical profiles, the manifold flow areas must be chosen properly. The areas may be either constant, or vary with manifold length. The flow areas control the velocity and hence the acceleration or deceleration of the flow.

In the Z-flow configuration, the supply manifold deceleration and discharge manifold acceleration act in the same direction. This results in conflicting static pressure profiles; the highest static pressure at the closed end of the supply manifold is opposed by the lowest static pressure in the discharge manifold. Conversely, the lowest static pressure at the inlet end of the supply manifold is opposed by the highest static pressure in the discharge manifold. The net effect of this static pressure unbalance is that Z-flow path A (fig. 13b) is starved of a proportional share of the flow. In order to effect uniform flow with a Z-flow configuration, the inlet manifold must be forced to accelerate its flow. This can be done by severely tapering the manifold area; i.e., decreasing the flow area from the open end to the closed end of the inlet manifold.

With the proper inlet manifold taper, matching pressure profiles can be attained, as shown in fig. 14b. The great disadvantage of the Z-flow configuration is that the pressure change from the inlet of the supply manifold to the outlet of the discharge manifold is not just the core pressure drop, but the core pressure drop plus the change in static pressure within either manifold. Thus, the pressure losses associated with a Z-flow system are inherently greater than those associated with a U-flow system.

Due to the size limitations in the HSA, the manifold pressure losses are significant with respect to the heat exchanger core losses for the multitube configurations; therefore, careful design is necessary. Manifolds of the U-flow type with flow normal to the core are indicated (fig. 13b). For simplicity, constant-area toroidal manifolds with circular cross sections are desired. The manifolds are visible in fig. 1. The ducts leading to and from the manifolds split the flow so that the fluid is transported around the manifold in two directions. The closed end of the manifold is at the position π radians from the duct (open end).

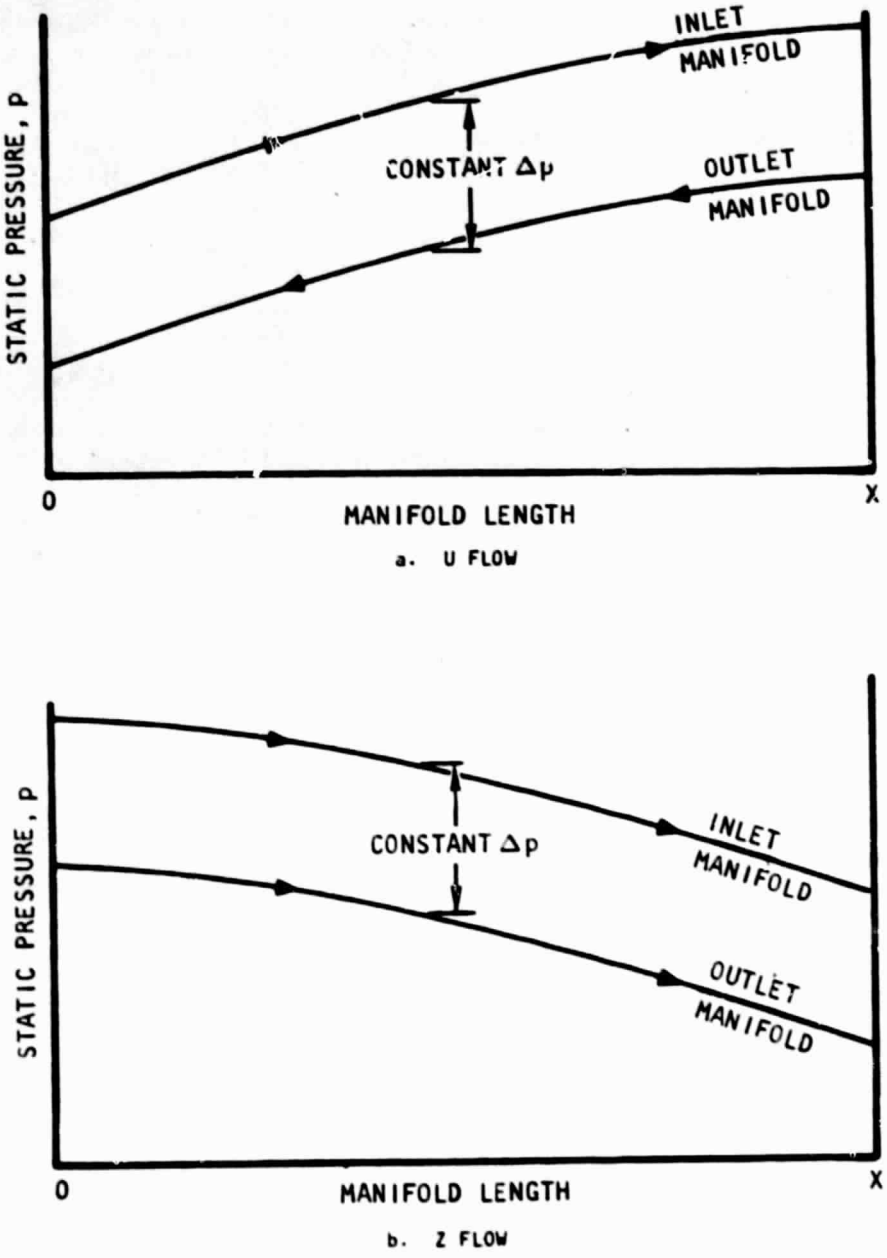

Figure 14.--Typical Manifold Static Pressure Profiles for Uniform Core Flow.

For constant-area, uniform-flow manifolds, the inlet manifold velocity pressure is much larger than the outlet manifold velocity pressure. Thus, if the density change is not too great, the inlet manifold flow area will be smaller than the outlet manifold area. With this in mind, the design technique involves assigning an area for the outlet manifold (such that the envelope requirements are met) and finding the best inlet manifold area.

The AiRLA manifold design computer program, X1000, was used for manifold sizing. The calculations include the effects caused by frictional losses in the manifolds. Because the toroidal manifolds are curved, friction factors for flow through curved tubes are used. Due to the decreasing flow velocity, the flow is turbulent near the manifold open end and laminar near the closed end. In the turbulent region, Ito's correlation, eq. (9), is used. In the laminar region, White's empirical formula as given by Ito (ref. 5) is used. The relatively severe manifold curvature is beyond the range of the correlation of Kubair and Varrier (ref. 2).

The overall pressure drop is determined by summing the heat exchanger core losses, the manifold turning and frictional losses predicted using computer program X1000, and the transition losses between the manifolds and the connecting ducts. The latter are quite significant due to the high losses associated with diverging and converging branched flow (ref. 6). Computer program X1000 is described in appendix B.

Candidate comparison and selection.--A comparision of the candidate designs is presented in table 10. It can be seen that the axial-flow tube bank is clearly the better of the two multitube designs. The weight and thermal performance are superior to the helical-flow tube bank. The HSIS is so effective that the direct impingement of radiation from the IHS on the HSIS in the axial-flow design does not substantially increase the thermal losses. The heat is essentially re-radiated to the back side of the HSHX by the insulation. For the C-103 design, the axial tube bank heat leak is actually lower than the helical tube bank heat leak. This is a result of the lower HSHX wall temperature due to superior heat transfer for the ring-dimpled axial tube bank.

A comparision of the axial-flow tube bank with the single-tube helical coil indicates substantially similar thermal performance. The axial-flow maximum metal temperature for the C-103 design exists on the outlet manifold, which is not insulated. Use of insulation as in the Hastelloy X design would lower the maximum metal temperature.

It can be seen that the axial-flow tube bank offers a substantial weight savings over the single-tube helical coil. Nevertheless, the selected design is the single-tube helical coil. The inherent simplicity and potential structural integrity and reliability of the single-tube design are considered to be of greater importance than the minization of weight. The multitube design requires over one hundred tube-to-manifold welds representing a large number of potential problem areas. The single-tube design has other advantages including no flow distribution problems, no requirement for manifold insulation, and negligible manifold pressure drop.

TABLE 10

HSHX WEIGHTS AND PERFORMANCE

	Single-tube helical coil	Axial-flow tube bank	Helical-flow tube bank
C-103			
Weight, kg (lb)	9.75 (21.5)	3.2 (7.1)	3.9 (8.5)
Fluid outlet temperature, °C (°F)	886 (1626)	884 (1623)	884 (1623)
HSA heat loss, percent	4.6	5.2	5.3
Maximum metal temperature, °C (°F)	916 (1680)	941 (1725)	958 (1757)
Hastelloy X			
Weight, kg (lb)	11.1 (24.4)	3.0 (6.6)	3.4 (7.5)
Fluid outlet temperature, °C (°F)	754 (1390)	752 (1386)	718 (1324)
HSA heat loss, percent	3.4	3.7	3.5
Maximum metal temperature, °C (°F)	786 (1447)	787 (1449)	788 (1450)

AIRLA does consider the axial-flow tube bank to be a viable alternative. It is felt that the potential areas of difficulty can be overcome with careful design. For systems in which the weight savings--as much as 8 kg (17.6 lb) per HSA--would be of great importance, the axial-flow tube bank should be considered.

Hastelloy X is the specified HSHX material for the BIPS. With the major emphasis on HSA reliability, AIRLA considers this to be the correct choice. Preliminary analysis indicates that it would be difficult to limit the PTCS temperatures to below the specified maximum for the high fluid temperatures in the C-103 cycle. BIPS performance requirements can be met at the lower operating temperature of the Hastelloy X design.

Heat Source Heat Exchanger Optimization

With the configuration of the HSHX selected as the single-tube helical coil Hastelloy X design, the task of optimizing the heat exchanger was undertaken. The design reference cycle conditions were updated based on information from the BIPS program office at AIRPHX. The cycle conditions, which replace those given in table 3, are given in table 11. This reference cycle was used for the remainder of the study. The conditions still represent the two-HSA configuration while the pressure containment requirement is for the three-HSA design.

TABLE 11

DESIGN REFERENCE CYCLE CONDITIONS

Flow rate, g/s (lb/s)	51.778 (0.11415)
Minimum outlet temperature, °C (°F)	704 (1300)
Maximum metal temperature, °C (°F)	788 (1450)
Inlet pressure, MPa (psia)	0.4267 (61.89)
Pressure containment requirement, MPa (psia)	0.703 (102)
Pressure drop goal, percent $\Delta P/P$	< 1
HSHX surface emissivity	0.8
Working fluid temperature rise, °C (°F)	172 (310)

The optimization considered HSHX weight, pressure drop, and thermal performance. Since the HSA heat losses are relatively independent of HSHX design, the key thermal performance feature is working fluid outlet temperature. The tradeoff relationships among weight, pressure drop, and fluid outlet temperature

were acquired from the BIPS program office at AIRPHX (J. Lloyd, BIPS-GDS Coordination Memo A0563, November 23, 1977) and are given below:

$$\Delta W = C \times \Delta(\Delta P/P) \tag{11}$$

$$\Delta W = D \times \Delta T \tag{12}$$

where ΔW is the change in equivalent weight

$\Delta(\Delta P/P)$ is the change in percent pressure drop

ΔT is the change in fluid outlet temperature

$C = -9.07$ for ΔW in kg and -20 for ΔW in lb

$D = 0.408$ for ΔW in kg and ΔT in °C and 0.5 for ΔW in lb and ΔT in °F

Eq. (11) indicates that $\Delta P/P$ could be increased by 0.2 percent if 1.8 kg (4 lb) could be saved in weight. Eq. (12) indicates that the fluid outlet temperature could be lowered by 0.55°C (1°F) if 0.22 kg (0.5 lb) could be saved in weight. The value for D is at a fluid outlet temperature of 760°C (1400°F), which will be seen to be the approximate value attainable for the optimized design.

The ground rule used for the HSHX optimization was an integral number of turns in the helical coil with an overall linear dimension of 40.34 cm (15.88 in.), the distance between the centerline of the connecting BIPS ducts. The tube outside diameter is equal to the duct centerline separation divided by the number of turns--with a 0.51- to 0.76-mm (0.02- to 0.03-in.) allowance for clearance between successive turns. The tube wall thickness requirements were determined by a pressure containment analysis, which is discussed in the structural analysis section. Thus, the only independent variable in the HSHX optimization is the number of turns.

HSHX designs are presented in table 12 for 9, 10, and 11 turns. Coils with more than 11 turns had pressure drops exceeding the 1 percent $\Delta P/P$ restriction, while coils with fewer than 9 turns required excessive wall thickness. The nominal wall thickness was taken as 5 percent greater than the minimum allowable to account for manufacturing tolerances. A constant clearance was maintained between the IHS surface and the inside of the coil; thus the smaller tubes have a smaller coil diameter. The HSIS and HSA outer case locations were not changed.

Heat transfer and pressure drop calculations were performed for the designs given in table 12 using the HSA thermal model modified for the specific number of turns. HSHX weights were calculated taking into account the required thick-walled elbows (see the structural analysis section). The results of the analyses are presented in table 13.

TABLE 12

HSHX DESIGNS FOR OPTIMIZATION STUDIES

Number of turns	Tube OD		Nominal wall thickness		Coil diameter		Tube length	
	cm	in.	mm	in.	cm	in.	cm	in.
9	4.42	1.74	1.42	0.056	24.8	9.76	701	276
10	3.96	1.56	1.30	0.051	24.3	9.58	764	301
11	3.61	1.42	1.19	0.047	24.0	9.44	829	326

TABLE 13

HSHX OPTIMIZATION RESULTS

Number of turns	ΔP/P, percent	Fluid outlet temperature		Actual weight		Equivalent weight	
		°C	°F	kg	lb	kg	lb
9	0.275	750.1	1382.1	11.3	24.9	11.6	25.7
10	0.504	756.0	1392.8	10.0	22.2	10.1	22.2
11	0.855	760.5	1400.9	9.1	20.1	10.5	23.1

It can be seen that as the number of turns increases, the pressure drop and fluid outlet temperature increase, while the actual weight decreases. It should be repeated that the calculations were based on a maximum HSHX temperature of 788°C (1450°F). Using the tradeoff relationships in eqs. (11) and (12), an equivalent weight was determined using the 10-turn design as the baseline. Table 13 indicates that the 11-turn HSHX has an equivalent weight 0.4 kg (0.9 lb) greater, and the 9-turn HSHX has an equivalent weight 1.5 kg (3.5 lb) greater than the 10-turn unit. Thus the 10-turn HSHX, with a 3.96-cm (1.56-in.) OD and a 1.30-mm (0.051-in.) wall is identified as the optimum design. All subsequent work in this study concentrates on this configuration.

Steady-State Results

With the selection of the optimized HSHX design, the steady-state HSA thermal analysis was performed. The HSA thermal model was updated to include the latest information on the HSA components. The complete thermal model is shown in fig. 15. Table 14 lists the component materials used in the model.

The number of foil layers in the HSIS was reduced to 60, reflecting the lower temperature superalloy HSHX cycle conditions. A Hastelloy X inner support mandrel for the HSIS was included in the model for both the cylindrical and planar insulation.

The number of HSHX radial nodes was increased from 2 to 4 per turn. This improvement resulted in 160 HSHX nodes, along with 41 fluid nodes.

A detailed model of the IHS was prepared to enable accurate prediction of the PICS temperatures. The IHS model is strictly two-dimensional, as the circumferential nodes on the surface were found to be unnecessary (note the small circumferential temperature variation in fig. 12). Within the IHS, heat is transferred primarily by radiation, with solid conduction heat transfer where appropriate. The partial pressure of helium released by the radioactive decay of the plutonium dioxide fuel is assumed to be too low to offer a significant conductive path within the IHS.

A key assumption that has a significant effect on the predicted PICS temperature is the emissivity of the PICS surface. According to Mound Laboratory (personal communication, E.W. Johnson, December 16, 1977), a reasonable value for the suface emissivity of the grit-blasted iridium is 0.28. This value was assumed for the study. The thermophysical properties for the various forms of graphite used in the IHS were obtained from the General Electric Company (R.J. Hemler, BIPS-GDS Coordination Memo G0161, December 12, 1977).

Using the complete thermal model, a steady-state HSA thermal map was produced based on the reference design conditions given in table 11. Pressure drop and heat transfer in the HSHX were predicted using eqs. (9) and (10), respectively. The average heat transfer coefficient in the heat exchanger tube was 108 $W/(m^2- K)$ [19 Btu/(hr-sq ft-°F)]. A heat sink temperature for the HSA of 49°C (120°F) was assumed.

The thermal map is presented in fig. 16 for all HSA components except the HSHX. The HSHX temperatures are listed in tables 15 and 16 for SI and customary engineering units, respectively. The HSHX nodal locations are indicated in fig. 17. Each of the 10 heat exchanger turns is divided into four quadrants in the coil circumferential (fluid flow) direction and four sections in the tube circumferential direction. The fluid temperatures are considered uniform within each quadrant.

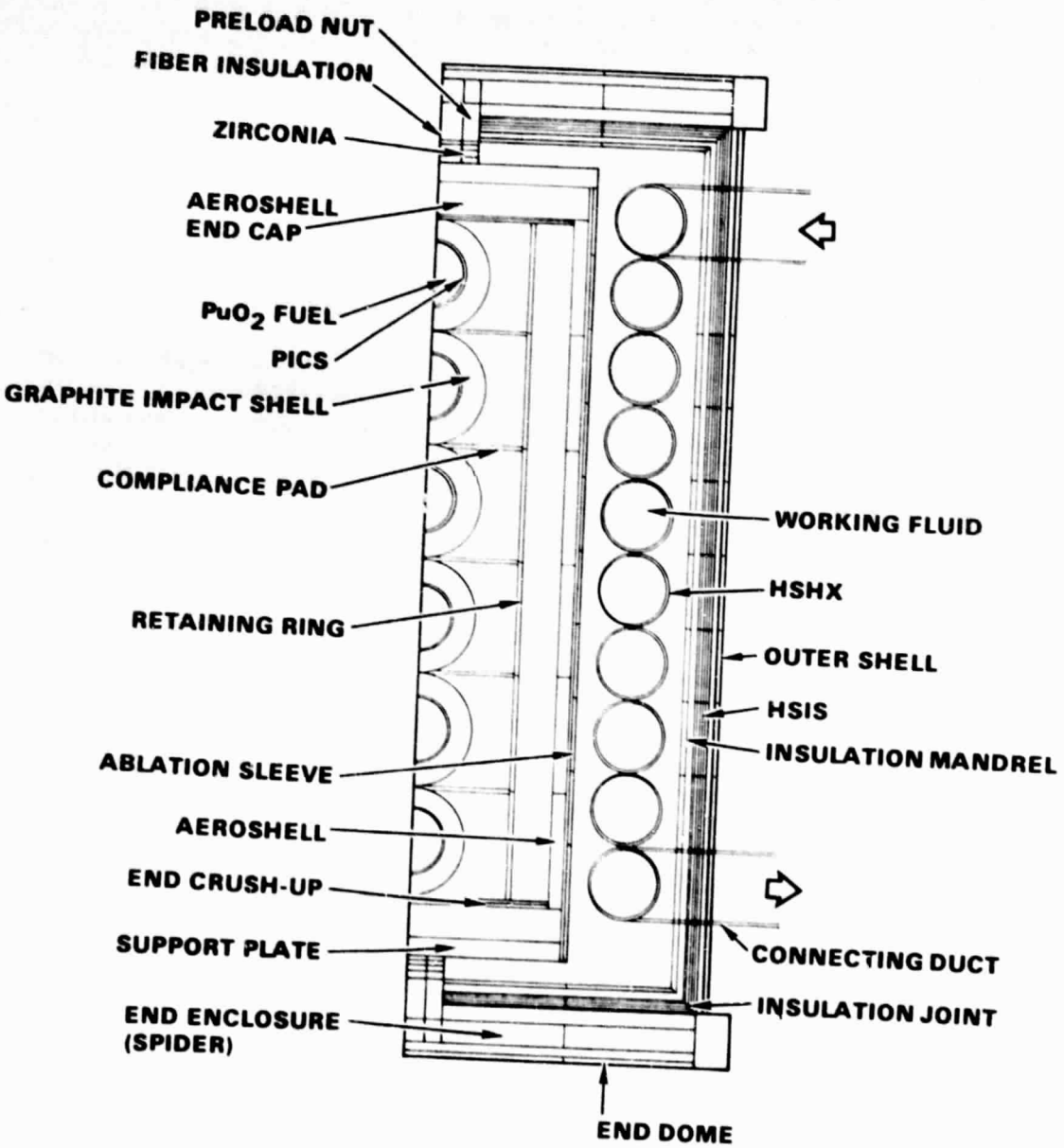

Figure 15.--HSA Thermal Model.

TABLE 14

HSA COMPONENTS

Component	Material
Post-impact containment shell (PICS)	Iridium
Graphite impact shell (GIS)	Thornel-50
Retaining ring	Pyrocarb-508
Aeroshell	Poco AXF-5Q
Ablation sleeve	Pyrocarb-406
Compliance pad	Thornel-50
End crush-up	Pyrocarb-508
Aeroshell end cap	Poco AXF-5Q
Support plate	Poco AXF-5Q
Fiber insulation	Astro-quartz
End spacer	Zirconia
Preload nut	Inconel X-750
End enclosure (spider)	Titanium
Support flange	Titanium
End dome	Lockalloy
Insulation mandrel	Hastelloy X
HSIS	Multi-Foil insulation
Outer shell	Lockalloy
HSHX	Hastelloy X

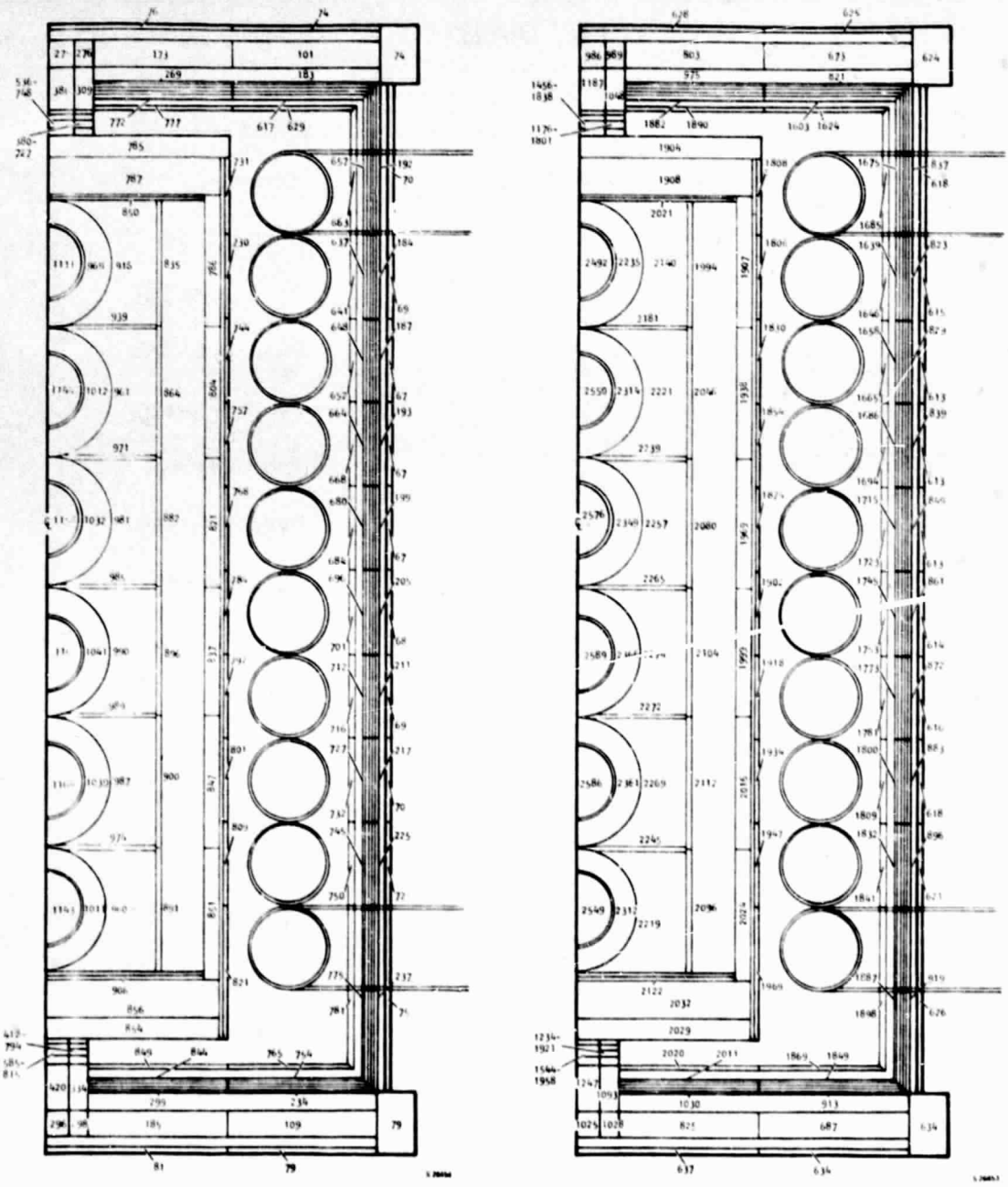

NOTES: W = 51.78 g/SEC (0.1142 LB/SEC)
P = 0.4267 MPa (61.89 PSIA)
SINK TEMPERATURE = 490C (580°R)
ε = 0.8

S-26473

Figure 16.--Steady-State HSA Temperature Profile.

TABLE 15

HSHX TEMPERATURES, °C

Tube No.	Quadrant position	Fluid Out of sect.	Temperature at circumferential position			
			A	B	C	D
Inlet		581				
1	1	588	652	619	614	621
	2	595	655	623	617	624
	3	601	658	628	622	628
	4	607	661	632	626	632
2	1	612	664	634	624	634
	2	617	667	637	627	637
	3	621	669	641	630	641
	4	626	672	644	634	644
3	1	630	681	651	640	651
	2	635	684	655	644	655
	3	639	686	658	646	658
	4	644	689	661	650	661
4	1	648	698	669	657	669
	2	652	700	672	661	672
	3	657	702	675	664	675
	4	661	705	678	666	678
5	1	665	713	685	675	685
	2	670	716	689	677	689
	3	674	717	691	680	691
	4	677	720	694	683	694
6	1	682	731	702	692	702
	2	687	733	706	695	706
	3	691	735	709	697	709
	4	695	737	711	700	711
7	1	699	744	718	708	713
	2	703	746	721	711	721
	3	707	749	724	714	724
	4	711	750	726	716	726
8	1	715	757	733	724	733
	2	719	759	736	726	736
	3	722	761	739	729	739
	4	726	763	741	731	741
9	1	730	769	747	740	747
	2	734	771	750	742	750
	3	737	772	752	744	752
	4	740	774	755	746	755
10	1	745	783	765	760	764
	2	749	785	767	763	767
	3	753	787	769	765	770
	4	756	788	770	767	772
Outlet		756				

TABLE 16

HSHX TEMPERATURES, °R

Tube No.	Quadrant position	Fluid Out of sect.	Temperature at circumferential position			
			A	B	C	D
Inlet		1537				
1	1	1550	1565	1605	1596	1609
	2	1562	1670	1613	1603	1615
	3	1573	1676	1622	1611	1622
	4	1584	1682	1630	1618	1629
2	1	1593	1687	1632	1614	1632
	2	1602	1692	1639	1620	1639
	3	1610	1696	1645	1626	1645
	4	1618	1701	1651	1632	1651
3	1	1626	1718	1664	1644	1664
	2	1635	1723	1670	1650	1670
	3	1642	1727	1676	1655	1676
	4	1650	1731	1681	1661	1681
4	1	1658	1748	1695	1675	1695
	2	1666	1752	1701	1681	1701
	3	1674	1756	1707	1686	1707
	4	1681	1760	1712	1691	1712
5	1	1689	1775	1725	1706	1725
	2	1697	1780	1731	1711	1731
	3	1704	1783	1736	1716	1736
	4	1711	1787	1741	1721	1741
6	1	1720	1807	1756	1737	1756
	2	1728	1811	1762	1742	1762
	3	1735	1815	1767	1747	1767
	4	1742	1818	1772	1752	1772
7	1	1750	1831	1784	1766	1784
	2	1757	1835	1789	1771	1789
	3	1764	1839	1794	1776	1794
	4	1771	1842	1799	1780	1799
8	1	1778	1855	1811	1794	1811
	2	1785	1858	1816	1799	1816
	3	1792	1862	1821	1803	1821
	4	1798	1865	1825	1807	1825
9	1	1805	1876	1837	1823	1837
	2	1812	1879	1841	1827	1841
	3	1818	1882	1846	1831	1846
	4	1824	1885	1850	1835	1850
10	1	1832	1901	1868	1860	1867
	2	1840	1905	1872	1865	1872
	3	1847	1908	1875	1869	1877
	4	1853	1910	1878	1873	1881
Outlet		1853				

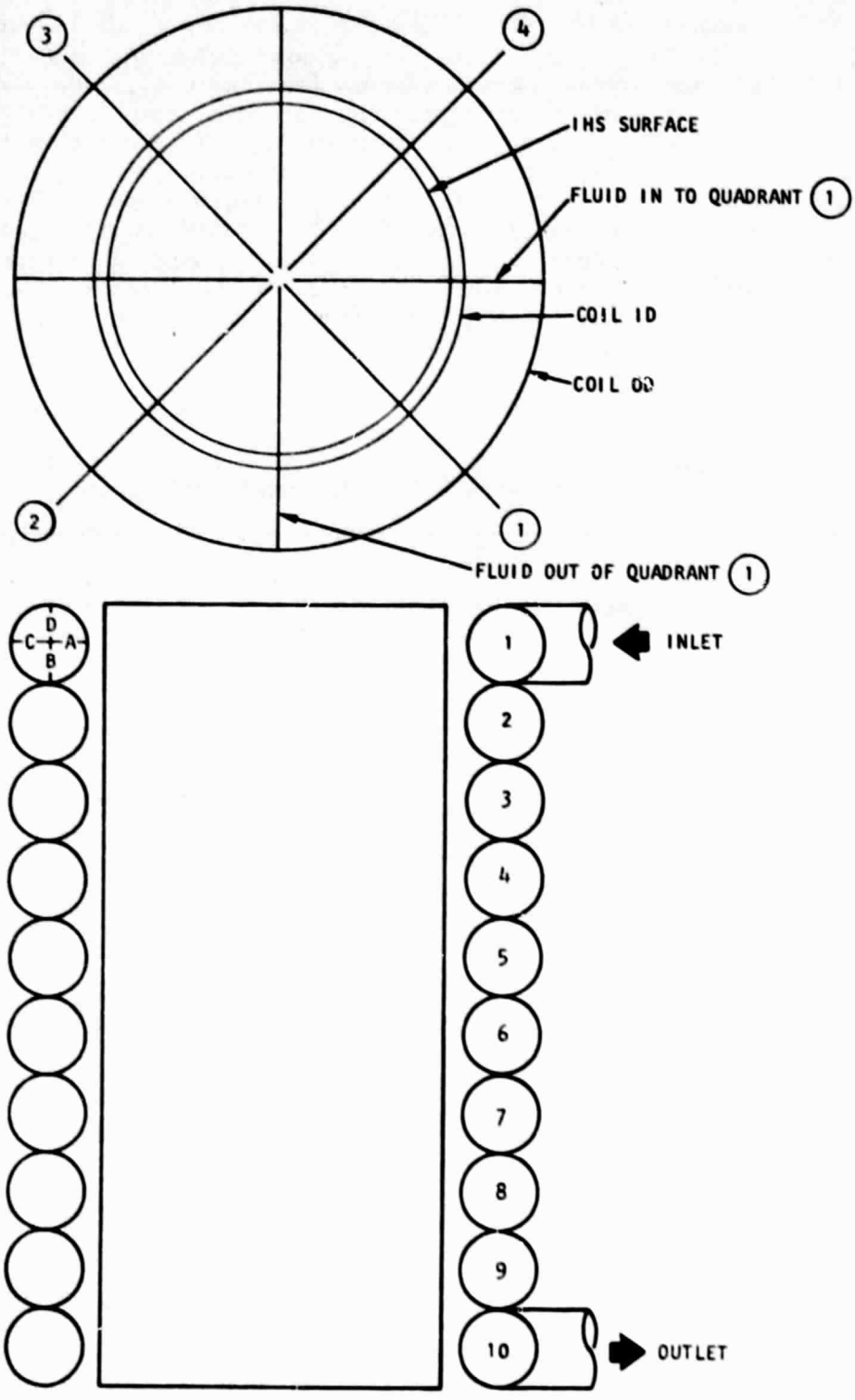

S-23800

Figure 17.--HSHX Thermal Model.

The key results of the steady-state analysis are shown in the first column of table 17. The PICS temperatures are somewhat below the specified limits of 1150° to 1200°C for steady-state operation (see table 1). The variation in PICS temperature is in the HSA axial direction, as can be seen from fig. 17, and is a result of the varying fluid temperature in the HSHX and the heat loss from the HSA ends. The maximum ablation sleeve temperature, listed for reference, is well within the capability of the ablation sleeve material, Pyrocarb-406. The working fluid outlet temperature of 756°C (1393°F) easily meets the minimum requirement of 704°C (1300°F). The working fluid temperature rise, HSA heat loss, and pressure drop meet the reference cycle requirements (see table 11). The maximum HSA outer shell temperature is well within the capability of the shell material, Lockalloy.

TABLE 17

HSA STEADY-STATE THERMAL ANALYSIS RESULTS

HSHX emissivity	0.8	0.6	0.3	0.25
PICS temperature range, °C	1111 to 1165	1117 to 1170	1138 to 1188	1145 to 1195
Maximum ablation sleeve temperature, °C (°F)	821 (1510)	829 (1525)	859 (1579)	871 (1599)
Working fluid inlet temperature, °C (°F)	580 (1076)	580 (1076)	579 (1075)	579 (1075)
Working fluid outlet temperature, °C (°F)	756 (1393)	756 (1392)	754 (1390)	754 (1390)
Maximum HSA outer shell temperature, °C (°F)	81 (178)	81 (178)	83 (181)	83 (182)
$\Delta P/P$, percent	0.504	0.504	0.504	0.504
HSA heat loss, percent	5.84	5.90	6.17	6.29

In order to increase the PICS temperatures to comply with the specified requirements, the thermal resistance between the PICS and the working fluid must be increased. One way to do this is to decrease the surface emissivity of the Hastelloy X HSHX. This would seem to be a reasonable approach, since to attain the baseline design emissivity of 0.8, surface treatment is required. The stability of this high emissivity is problematical.

A sensitivity study was conducted by performing HSA thermal analyses for HSHX's of various surface emissivities. It should be noted that uniform emissivities were assumed for the entire outside surface of the HSHX--the portion viewing the IHS and the portion viewing the HSIS. The emissivity of the surface of the HSHX facing the HSIS does not directly affect the thermal resistance between the PICS and the working fluid, but does affect the HSHX temperature. The results of the study are summarized in the remainder of table 17. Note that for each case, the maximum HSHX wall temperature was 788°C (1450°F).

It can be seen that the 0.25 emissivity yields PICS temperatures very close to the required temperature range of 1150° to 1200°C. This emissivity corresponds to the value for untreated Hastelloy X. Naturally, the temperature level of the entire IHS increases as the PICS temperature increases, as can be seen from the ablation sleeve temperatures. The decreased emissivity does cause a small performance penalty, however. The 0.25 emissivity case results in a 2°C (3°F) drop in the attainable working fluid outlet temperature. In addition, the heat loss from the HSA is increased for the lower HSHX emissivity.

Based on the results of the sensitivity study, the untreated HSHX emissivity of 0.25 looks promising; however, the effect of this emissivity must be checked for all operating conditions including the ECS, ACS, and the startup transients.

As previously mentioned, the HSA heat sink assumed for the preceding analyses was 49°C (120°F). To estimate the effect of the heat sink on the important HSA parameters, an analysis was performed for a heat sink of -62°C (-80°F). The change in heat sink temperature had a minimal effect on the key HSA parameters; the temperatures of the PICS and HSHX decreased by less than 0.3°C (0.5°F) and the HSA heat loss increased by about 1 W. This would seem to indicate that diurnal temperature changes in orbit should have a negligible effect on HSHX thermal fatigue.

Auxiliary Cooling System

The ACS is required to provide cooling for the HSA during all nonoperational phases of the Brayton cycle when there is no circulating working fluid available to remove the heat produced by the IHS. Thus, the ACS must operate on the launch pad, in space prior to system startup, and during any subsequent system shutdown. The requirements for ACS operation are as follows:

(1) On the launch pad, all exposed surfaces must be maintained below 193°C (380°F) to prevent possible ignition of fuel vapors present in the prelaunch environment.

(2) The PICS temperatures should be maintained in the 1050° to 1200°C range--the launch and ascent requirements given in table 1. It should be noted that the PICS temperature "window" is wider for ACS operation than for normal operating conditions.

(3) The HSHX temperature should not be so high as to seriously degrade fatigue life.

The ACS design consists of a stagnant inert gas completely filling the HSA from the PICS outward. The inlet gas decreases the heat transfer resistance in the HSA, primarily by short-circuiting the HSIS and providing a gas thermal conductive path through the foil package. In addition, all other radiation gaps in the HSA from the PICS outward similarly become gas thermal conductive paths, further decreasing the resistance. On the launch pad, heat can also be transferred by natural convection, both within the HSA and from the HSA to its surroundings. For the present analysis, the inert gas is assumed to be contained in a hermetically sealed "cocoon" surrounding all of the HSA, as well as the BIPS power conversion equipment, except for the top (forward) end dome, which penetrates the cocoon to permit insertion of the IHS. The cocoon offers a number of advantages to the BIPS operation:

(1) The HSA can be evacuated while the system is on the launch pad, thereby permitting ground operation of the power system.

(2) The cocoon mitigates the exposed temperature requirement on the launch pad, as the top end dome is the only part of the HSA that is exposed. The cocoon, with its large surface area, should be well below 193°C (380°F).

(3) The HSA case-to-duct bellows can be eliminated since the HSA case does not have to be sealed--the cocoon serves as the pressure containment vessel.

Launch Pad Operation.--The ACS launch pad operation was analyzed using the complete HSA thermal model modified for the auxiliary cooling conditions by including gas conduction and natural convection heat transfer in all radiation gaps. For heat transfer calculations, the inert gas is assumed to be at ambient pressure. For natural convection, the gravity vector is assumed to be along the HSA axis. Natural convection is suppressed in the HSIS due to the numerous foil layers. Since there is no fluid flow in the HSHX, the quadrant nodes in the coil circumferential direction were eliminated. This simplification resulted in 40 HSHX nodes in two dimensions. The working fluid inside the HSHX is assumed to be stagnant at 0.21 MPa (30 psia), the approximate BIPS pressure for zero-flow conditions.

The cocoon is modeled as a uniform temperature, steady-state node. A constant-temperature heat sink of 49°C (120°F) is assumed for both the cocoon and the top end dome. In general, heat transfer to the heat sink is by radiation and natural convection through ambient air. Preliminary thermal analysis indicated that with certain fill gases these heat removal modes would not be sufficient to maintain the top end dome at a temperature below 193°C (380°F). Additional cooling across the top end dome surface is required. Possibilities for this cooling include flowing a liquid coolant through coils on the end dome surface, or blowing ambient or cooled air over the surface. Since design of this coolant loop was beyond the scope of the study effort, a forced-convection heat transfer coefficient of 28 W/(m^2-K) [5 Btu/(hr-sq ft-°F)] acting over the entire top end dome area was assumed. This forced-convection cooling, in addition to the radiation heat transfer, was sufficient to cool the top end

dome to below 193°C (380°F). The cocoon is much cooler than the end dome and does not require additional cooling.

In order to determine the appropriate fill gas, thermal analyses were conducted using helium, neon, argon, and xenon. The baseline design HSHX, with a surface emissivity of 0.8, was assumed for the fill gas comparison study. A summary of the important HSA temperatures for the different fill gases is given in table 18. The xenon results are not shown since with this fill gas the HSA temperatures are so high that melting of some of the insulation foils was predicted. With helium as the fill gas, additional cooling of the HSA top end dome is not required.

TABLE 18

HSA TEMPERATURES FOR LAUNCH PAD AUXILIARY COOLING OPERATION

	Temperature, °C (°F)			
	Helium[a]	Neon	Argon	Neon[b]
PICS	851 to 897 (1564 to 1647)	1014 to 1050 (1858 to 1922)	1219 to 1249 (2227 to 2280)	1051 to 1085 (1923 to 1985)
Abalation sleeve (maximum)	619 (1147)	782 (1440)	1023 (1874)	837 (1538)
HSHX (maximum)	573 (1064)	751 (1383)	1007 (1844)	771 (1419)
Top end dome (maximum)	183 (362)	152 (305)	161 (322)	153 (307)
Cocoon	77 (171)	74 (166)	74 (165)	74 (166)

[a]No additional cooling for top end dome.
[b]HSHX surface emissivity of 0.25.

It can be seen from the first three columns of table 18 that the PICS temperatures come closest to the specified range of 1050° to 1200°C with neon as the fill gas. Helium provides such a good heat transfer path that the predicted PICS temperatures are far below the desired range. With argon, the heat transfer resistance is not sufficiently decreased to cool the PICS below 1200°C. In addition, the HSHX maximum wall temperature using argon is 219°C (394°F) above the maximum steady-state operating temperature of 788°C (1450°F). The variation in PICS temperature is in the HSA axial direction, and is due to heat transfer from the ends of the HSA. The absence of fluid flow in the HSHX allows for more uniform PICS temperatures than for normal operating conditions.

The complete HSA temperature map for the neon launch pad ACS, with additional cooling of the top end dome and a HSHX surface emissivity of 0.8, is shown in fig. 18. The nodal model is described in fig. 15 and table 12.

The fourth column in table 18 shows the results of a thermal analysis for the neon fill gas and an HSHX emissivity of 0.25, the nominal value for untreated Hastelloy X. The increased thermal resistance caused by the lower emissivity results in higher PICS temperatures. As can be seen from table 18, the predicted PICS temperature range is within the specified requirements.

Space Operation.--The space ACS differs from the launch pad ACS in the following particulars:

(1) The temperature limit of 193°C (380°F) for exposed surfaces does not apply to the space system since launch pad fuel vapors are not present. Thus, additional cooling of the exposed HSA top end dome is not required. The need for HSA or cocoon cooling because of possible spacecraft heat dump limitations is beyond the scope of the study.

(2) The conditions of a diminished gravitational field and a space vacuum preclude any natural convection to the fill gas or to the environment. This increases the thermal resistance of the HSA because the fill gas can transfer heat by conduction only. As a result, the PICS temperatures will tend to be higher for the space ACS than for the launch pad ACS.

The space ACS operation was analyzed for the recommended neon fill gas using the same HSA thermal model as for launch pad ACS operation, with removal of natural convection heat transfer and additional cooling for the top end dome. The neon fill gas is assumed to be at a pressure sufficient to support continuum flow (only a few torr are required). For this condition, the neon thermal conductivity can be considered equal to its conductivity at ambient pressure. Other conditions were identical to those for the launch pad ACS.

The results of the space ACS thermal analyses with neon as the fill gas are summarized in table 19 for the reference design HSHX surface emissivity (ε) of 0.8 and the untreated surface emissivity of 0.25.

The predicted PICS temperatures are approximately 25°C higher than those for the launch pad ACS. The temperatures are just outside the required range for the 0.8 HSHX surface emissivity and well within the range for the 0.25 HSHX emissivity. The maximum HSHX temperatures are approximately 40°C (70°F) higher than those for the launch pad ACS. Although the HSHX maximum temperature for the 0.25 emissivity exceeds the long-term temperature limit of 788°C (1450°F), this should cause no difficulty during the short-duration space ACS operation.

The HSA temperature profile for the reference design HSHX emissivity of 0.8 is shown in fig. 19.

TEMPERATURES IN ^{o}C

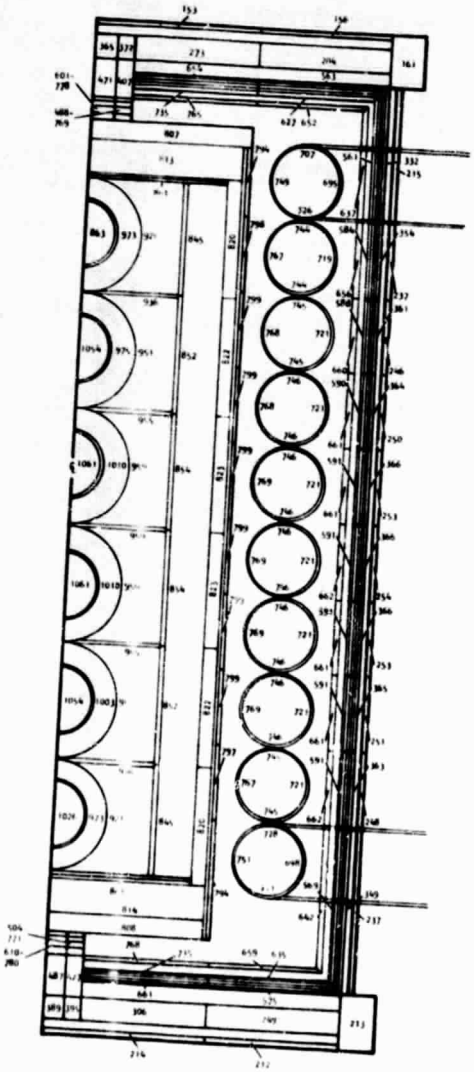

S-25826

TEMPERATURES IN ^{o}R

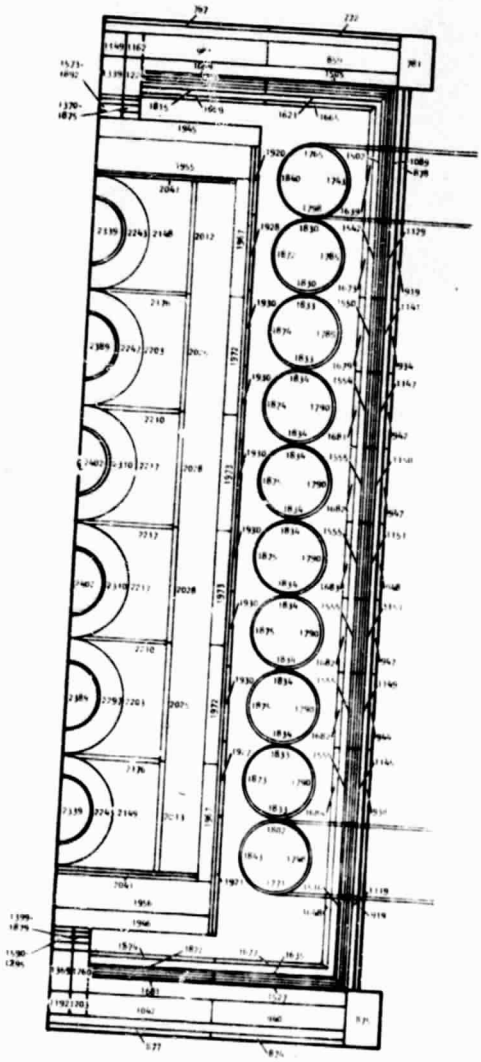

S-24432

NOTES: HSA FILLED WITH NEON AT AMBIENT PRESSURE
SINK TEMPERATURE = 49°C (580°R)
ADDITIONAL COOLING FOR TOP END DOME

S-26106

Figure 18.--Neon Launch Pad ACS HSA Temperature Profile.

ORIGINAL PAGE IS OF POOR QUALITY

TEMPERATURES IN ^{o}C

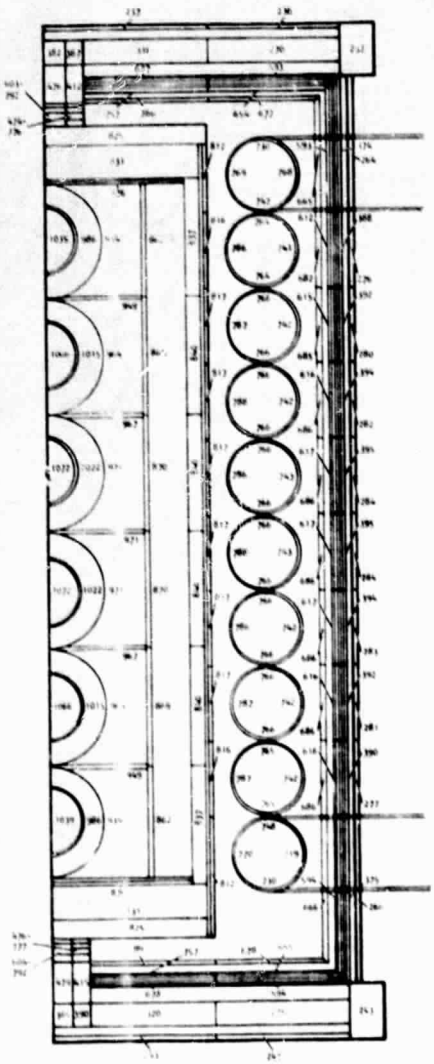

S-25825

TEMPERATURES IN ^{o}R

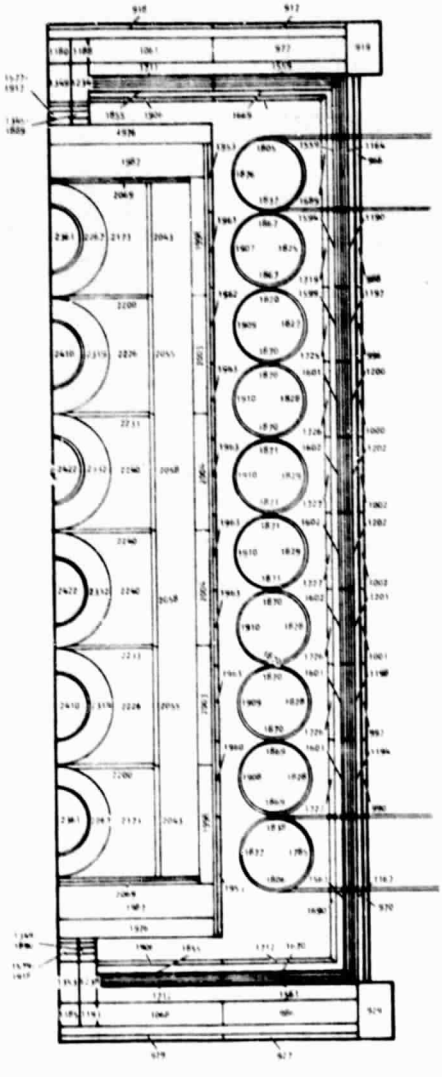

S-25249

NOTES: HSA FILLED WITH NEON
SINK TEMPERATURE = 49°C (580°R)

S-26105

Figure 19.--Neon Space ACS HSA Temperature Profile.

TABLE 19

HSA TEMPERATURES FOR SPACE AUXILIARY COOLING OPERATION

	Temperatures, °C (°F)	
	ε = 0.8	ε = 0.25
PICS	1039 to 1073 (1902 to 1963)	1075 to 1108 (1968 to 2027)
Ablation sleeve (maximum)	817 (1503)	871 (1599)
HSHX (maximum)	788 (1450)	809 (1488)
Top end dome (maximum)	237 (458)	239 (463)
Cocoon	89 (193)	89 (193)

To determine the effect of assumed heat sink temperature on the important HSA temperatures, a thermal analysis was performed for a heat sink temperature of 71°C (160°F). As compared with the 49°C (120°F) heat sink, the maximum PICS temperature increased by about 3°C and the maximum HSHX temperature increased by about 4°C (7°F). This indicates that the heat sink temperature has a greater effect on ACS operation than on normal steady-state operation. Even for the ACS operation, the sensitivity of the key HSA temperatures to the heat sink temperature is not large enough to have a significant system impact.

Heat Source Assembly Fueling Transient

The IHS and the HSA are stored separately. The loading or fueling of the IHS into the HSA is effected in the mobile loading station (MLS). The fueling transient results in a large temperature variation in the HSHX; the unit is heated from essentially ambient conditions to close to operating temperatures. Thermal analyses were performed to map the HSHX temperatures during the fueling transient with the goal of determining the impact on the low-cycle fatigue life of the unit.

The MLS initially contains the entire BIPS, with an electrical heat source (EHS) substituting for the IHS, at essentially ambient conditions. A circulating inert gas flows through the MLS prior to and during the fueling. Inside the HSA and cocoon the gas can be assumed to be stagnant and at ambient pressure; heat is transferred by natural convection, conduction, and radiation. For the fueling analysis, the inert gas was assumed to be neon. This gas is recommended since the fueling operation approaches a steady-state condition similar to the ACS mode. The temperature requirement for the PICS during ground handling is 1200°C maximum with no minimum (see table 1). The prior ACS analysis indicates the inapplicability of argon for the fill gas in the MLS. However, since there is no minimum PICS temperature requirement during ground handling, helium could be used in the MLS. The helium would have to be flushed out and replaced by neon after connection of the BIPS to the launch vehicle.

The fueling is initiated by removing the EHS from the BIPS HSA and replacing it with the IHS. Since this operation is likely to take a reasonable amount of time, the IHS can be assumed to reach a steady state with respect to the neon environment. These steady-state IHS temperatures are the initial temperatures for the fueling transient.

To determine the steady-state IHS temperatures, a thermal analysis was conducted using the HSA thermal model depicted in fig. 15. Only the IHS nodes were used. The heat sink for the IHS was assumed to be stagnant neon at ambient pressure and 27°C (80°F). The results of this analysis are summarized in table 20.

TABLE 20

AVERAGED IHS STEADY-STATE TEMPERATURES IN THE MLS

Component	Temperature	
	°C	°F
PICS	791	1455
GIS inner surface	721	1329
GIS outer surface	662	1223
End crush-ups	495	923
Retaining ring	397	747
Aeroshell	337	638
Aeroshell end caps	326	618
Ablation sleeve	279	535

The IHS temperatures shown in table 20 are well below the temperatures at normal ACS or BIPS operation. This is due to the greatly reduced thermal resistance when the IHS is outside of the HSA. Note that the temperature of the outer surface of the IHS is only 279°C (535°F).

Since the fueling transient takes a few hours to approach steady state, a simplified HSA model was required to reduce computer time. In the simplified model, each set of axial components in the IHS, HSHX, HSIS, and HSA outer case is represented as a single node. In addition, the HSHX quadrant nodes in the coil circumferential direction are lumped together as a single node.

The simplified model has one PICS node and four HSHX nodes. Since there is no fluid flow through the HSHX during the fueling transient, the preceding

assumptions are not unreasonable. However, due to heat losses out the ends of the HSA, there will be a small axial temperature variation. The PICS and HSHX temperatures predicted with the simplified model represent the average axial temperatures. The actual maximum PICS and HSHX temperatures will thus be somewhat higher than the average temperatures.

The temperatures listed in table 20 are input as the initial IHS temperatures. All other initial HSA temperatures (including the HSHX) as well as the constant heat sink temperature are assumed to be 49°C (120°F). The HSHX is assumed to be filled with stagnant Xe-He working fluid at 0.21 MPa (30 psia), the approximate BIPS pressure for zero-flow conditions.

The predicted HSHX temperatures during the fueling transient are shown in fig. 20. Also shown are the PICS temperatures. The reference HSHX, with an emissivity of 0.8, was used in the model. It can be seen that after the initial rapid HSHX temperature rise, the approach to steady state is slow. The circumferential temperature gradients in the HSHX tube do not seem to be particularly severe during the transient. The predicted PICS temperature is around 1030°C after 6 hours.

BIPS Startup Transient

When cool working fluid enters the HSHX during the system startup, large thermal gradients may be produced in the heat exchanger, producing stresses that must be evaluated to determine the LCF life of the unit. The HSA has a requirement for a minimum of 100 startup cycles without evidence of fatigue cracking. The study work concentrated on the thermal gradients and cycle life prediction for the HSHX. The thermal analysis is discussed in this section. The LCF life prediction is discussed in the structural analysis section.

The BIPS program office at AIRPHX has provided the latest BIPS startup conditions for the proposed flight system start (B. Minshall, BIPS-GDS Coordination Memo A0609, April 21, 1978). The HSHX inlet flow and temperature from the AIRPHX system transient computer program are shown for the BIPS startup in fig. 21. The conditions are identified as Run 600. Also shown are the HSHX outlet temperatures as predicted from the system program and the detailed HSA model. These temperatures will be discussed later. Note that the flow is for the entire two-HSA BIPS; the flow through each HSA is taken as one-half of the total. It should be emphasized that the startup conditions are preliminary as the flight system scenario has not been finalized.

The proposed startup scenario begins with the HSA in the steady-state space ACS mode of operation. The HSA heat sink is assumed to be about 16°C (60°F). This is expected to be the coldest heat sink (radiator temperature) for the HSA while the BIPS is in the spacecraft; the coldest heat sink represents the most critical startup condition. The BIPS rotating equipment will be motored and allowed to accelerate to full speed to check engine operation. At this point, the neon is vented from the HSA. This is the zero time for the transients shown in fig. 21. It can be seen from fig. 19 that the stagnant working fluid in the HSHX during the ACS deployment is close to normal operating

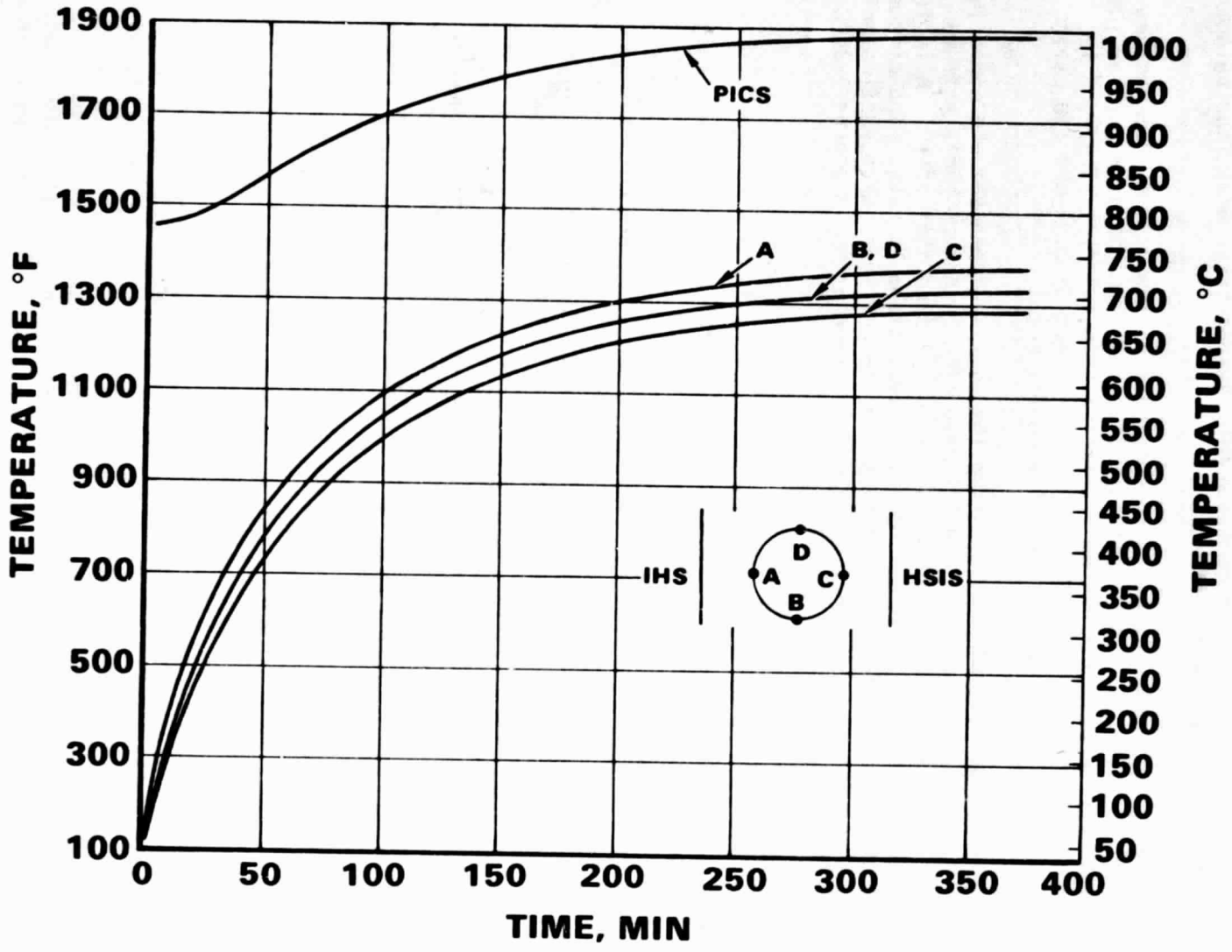

Figure 20.--HSHX Temperatures During HSA Fueling.

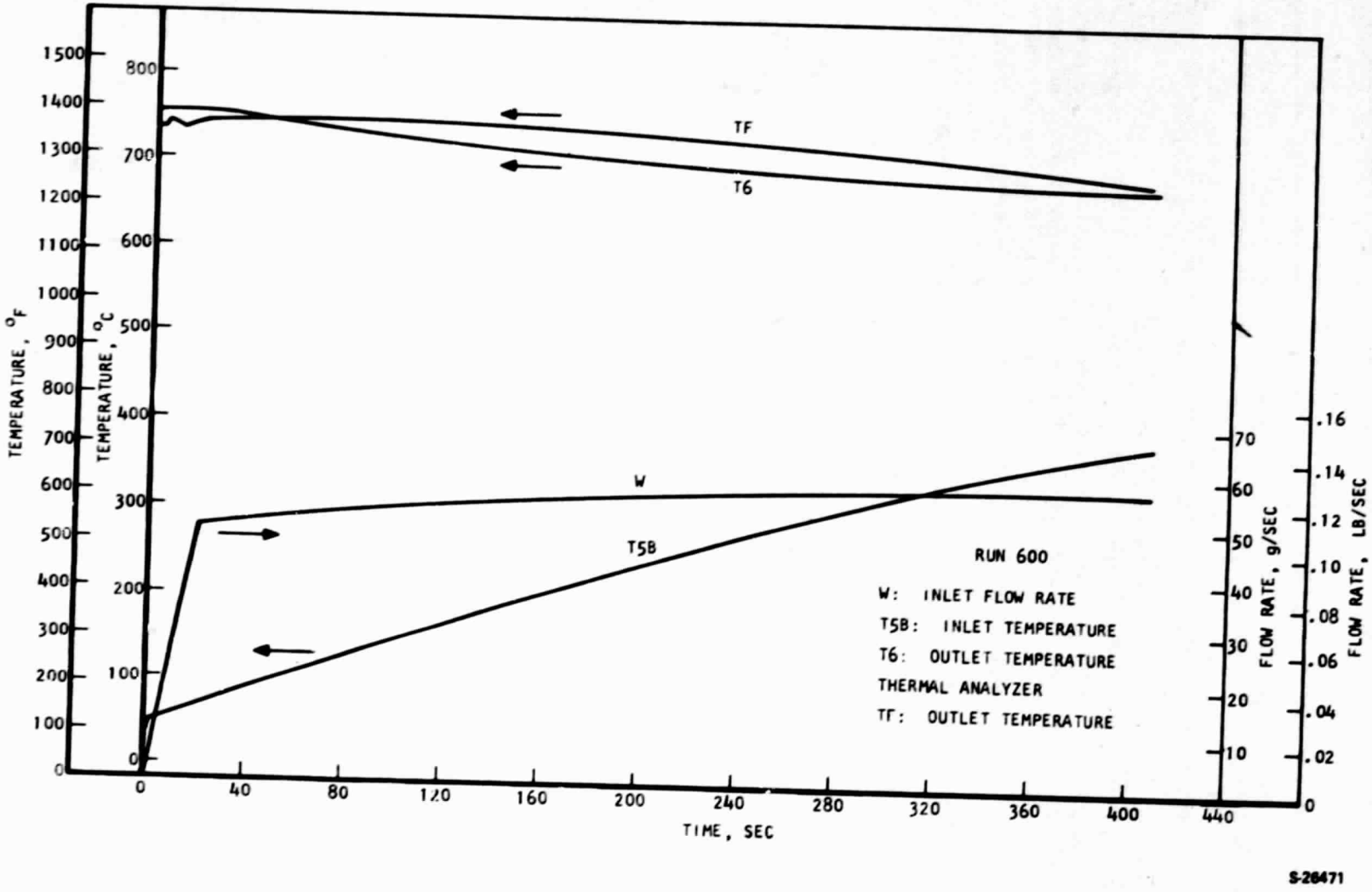

Figure 21.--BIPS Startup Transient Run 600.

temperatures. The scenario is described in detail in the BIPS memo referenced in the preceding paragraph.

To analyze the startup temperatures, the thermal analyzer computer program was run in the transient mode using the complete HSA model shown in fig. 15. The initial conditions for the transient were taken from a space ACS analysis, similar to that shown in fig. 19, but with a heat sink temperature of 16°C (60°F). The temperatures from this run are very similar to those shown in fig. 19.

The key results of the transient analysis are shown in fig. 22. HSHX temperatures are shown at the inlet and outlet ends of the unit. The reference HSHX, with an emissivity of 0.8, was used in the model. Temperatures for two of the four circumferential nodes are shown; the node facing the IHS and the node facing the HSIS. Complete HSA temperature profiles are available from the author for various times during the startup transient; these are not presented in this document.

It can be seen that the inlet portion of the HSHX, initially hot during ACS operation, is rapidly cooled by the cold working fluid. Since the IHS remains hot, the heat flux to the inlet region of the HSHX increases, resulting in an increase in tube circumferential temperature gradient. The inlet end minimum tube wall temperature and maximum circumferential temperature gradient occur about 180 sec after startup. The temperatures at the HSHX outlet end are still decreasing at 420 sec; these temperatures must bottom out and increase as steady state is approached.

Referring back to fig. 21, the predicted fluid outlet temperature is shown and compared with the HSHX outlet temperature from Run 600. The AIRPHX system computer program has a simplified model for the HSA and HSHX; thus the outlet temperatures will be somewhat different than for the detailed HSA model. The agreement must be close enough to ensure that the HSHX inlet temperatures are reasonably accurate. The agreement in fig. 21 would appear to be satisfactory for this analysis; for a more accurate thermal analysis, another iteration between the system model and the HSA model would be required.

The PICS temperatures are initially at the space ACS values. During the startup, the PICS temperatures increase and approach the steady-state values. The steady-state temperatures are not exceeded during the startup transient.

Emergency Cooling System

The ECS is required to maintain the PICS at a safe temperature (see table 1) in the event of a failure in the BIPS, such as a loss of working fluid accident or a breakdown in the ACS. The ECS must remove the heat generated by the IHS fuel that is normally removed by the circulating working fluid.

The present ECS design relies on the successive melting of the HSIS foil layers. If a system failure occurs, the heat released by the fuel is initially absorbed by the HSA components, including the IHS, the HSHX, and the HSIS. Only a small amount of heat can be rejected to the environment due to the high

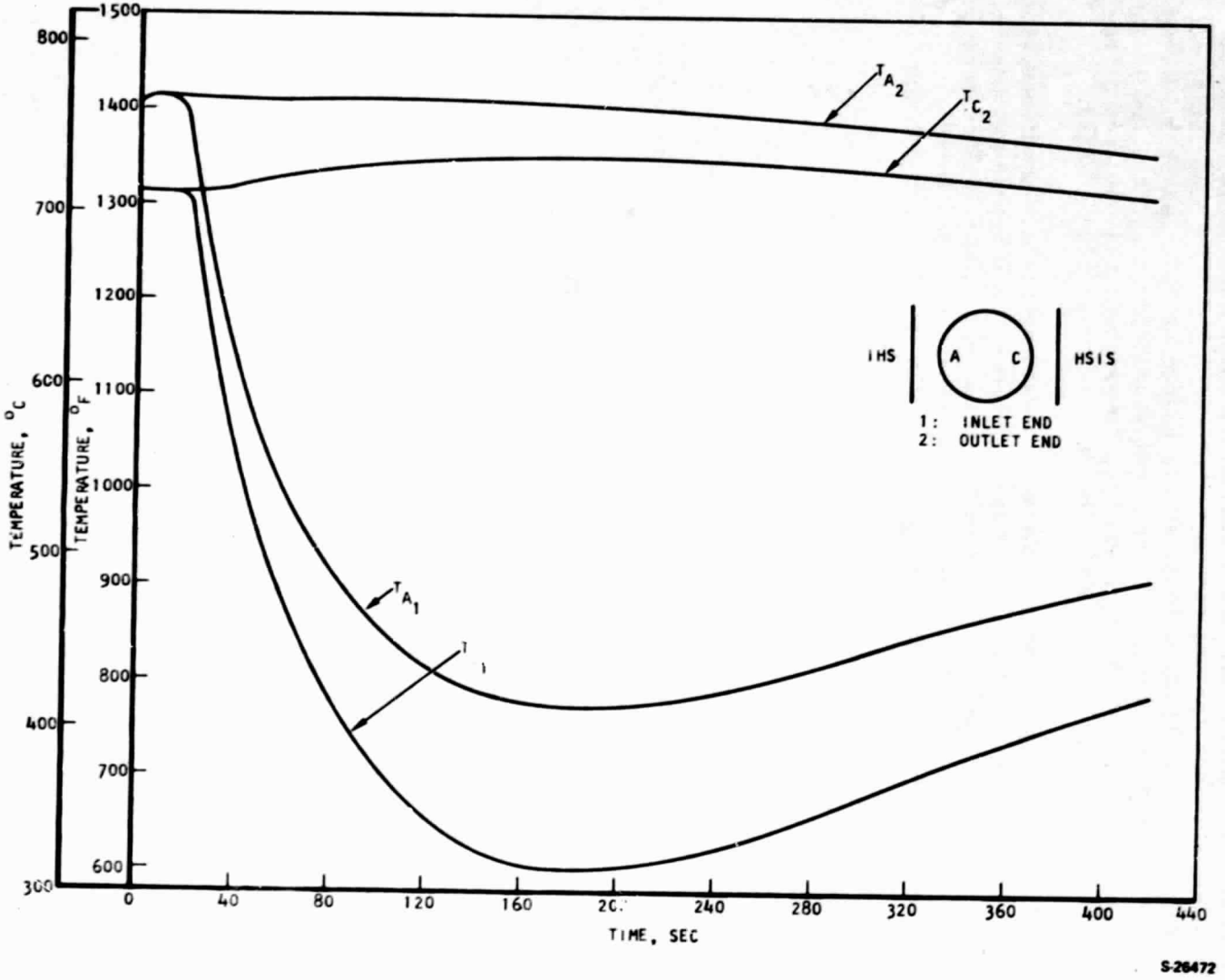

Figure 22.--HSHX Temperature During BIPS Startup.

thermal resistance of the insulation. The absorbed heat causes the temperature of the HSA components to rise. As the temperature of the hottest foil (closest to the IHS) reaches the foil melting temperature, the layer melts and allows increased irradiation of the next foil, with a subsequent increase in temperature. As each foil melts, the resistive path through the insulation bundle decreases, and the heat loss to the heat sink increases. At some point, a steady state will be reached, with a certain number of foil layers surviving. At this point, the heat generated by the fuel equals the heat rejected to the environment. As listed in table 1, the PICS temperature must be controlled both during the transient meltdown and the post-meltdown steady state.

With this goal in mind, both transient and steady-state thermal analyses were performed for the ECS mode of operation. Since the ECS mode represents a long running transient, the simplified HSA model was used. In this model, as discussed previously, each set of axial components is represented as a single node. Use of the simplified model results in predicted average PICS temperatures somewhat below the maximum PICS temperatures.

In order to determine the transient meltdown characteristics, it was necessary to modify the AIRLA thermal analyzer program to account for foil melting. To reduce computation time, the 60 foil layers in the HSIS were lumped into 14 nodes with the innermost node composed of 3 foils, the next eleven nodes five foils each, and the last two nodes one foil each. The foil nodes or packets are modeled to melt when the node reaches the melting temperature. The melted packet is assumed to resolidify on the next outer packet. The mass of the melted packet is combined with the outer packet to form a new node of increased thermal capacitance. This reduces the effective number of radiation shields and increases the thermal conductance through the HSIS. At any time, the innermost node contains, in addition to its own mass, the mass of all the previously melted foils. In this manner, the heat of fusion required to melt the foils is recovered upon resolidification.

For the present analysis, all of the foils were assumed to be a mixture of 40 percent Ni and 60 percent Pd, with a constant melting temperature of 1237°C (2259°F). There seemed to be no reason to include any higher melting point pure Ni or Mo foils, since it became apparent that it would be desirable to melt as many of the foil layers as possible.

The TECO correlation for heat transfer through the foils, eq. (1), was not used for the ECS transient since it represents heat transfer from the hot side to the cold side of the entire foil package. Due to the change in effective foil emissivity with temperature, eq. (1) is not valid for each of the insulation nodes used for the ECS transient analysis. Instead, effective foil emissivity data, presented in T. Ashe, BIPS-GDS Coordination Memo A0090, December 23, 1975, were used so that each node would have an emissivity appropriate to its temperature. The effective emissivity includes both the radiation and conduction heat transfer in the foils, modeled as radiation heat transfer; the conductive path is provided by the refractory oxide binder in the Multi-Foil system. The emissivity data were used with the following equation for radiation heat transfer through a series of radiation shields (ref. 7).

$$\phi = \frac{\sigma \epsilon_f}{N\,(2-\epsilon_f) + 1} \left[T_h^4 - T_c^4 \right] \qquad (13)$$

where ϕ is the heat flux perpendicular to the foils

σ is the Stefan-Boltzmann constant

ϵ_f is the effective foil emissivity at the average temperature of a packet

N is the number of foil layers in the packet

T_h is the hot-side temperature of the packet

T_c is the cold-side temperature of the packet

During the ECS transient, the Hastelloy X HSHX and insulation support mandrel are heated well above their normal operating temperatures. Indeed, during the transient the temperatures exceed the solidus point of Hastelloy X, 1260°C (2300°F). In the meltdown analysis, it was assumed that the Hastelloy X components would remain in the model as thermal barriers unless their temperatures exceeded the liquidus point, 1354°C (2470°F)

Other assumptions made for the ECS transient analysis included the following:

(1) The heat sink was 49°C (120°F).

(2) The reference design HSHX was used (surface emissivity = 0.8).

(3) Any effects due to sublimation of either the insulation or the HSHX were not included in the model.

(4) The starting point for the ECS transient was the steady-state normal operating condition.

The key results of the ECS meltdown transient are shown in fig. 23. It can be seen that during the transient, the HSHX temperature does not exceed the liquidus point of Hastelloy X. Thus, the HSHX and the support mandrel (which is cooler than the HSHX) are retained in the model as thermal barriers throughout the meltdown. Elimination of these nodes would tend to decrease the HSA resistance and ultimate PICS temperature.

Starting at its steady-state temperature at zero time, the PICS temperature increases until the first foil packet is melted at about 130 min. At this point the PICS temperature is 1432°C. Foil meltdown continues for about 40 min. At this point (as can be seen from the heat loss curve in fig. 23) the thermal resistance of the HSIS has decreased sufficiently so that almost all of the heat produced by the foil is rejected to the environment. The remaining

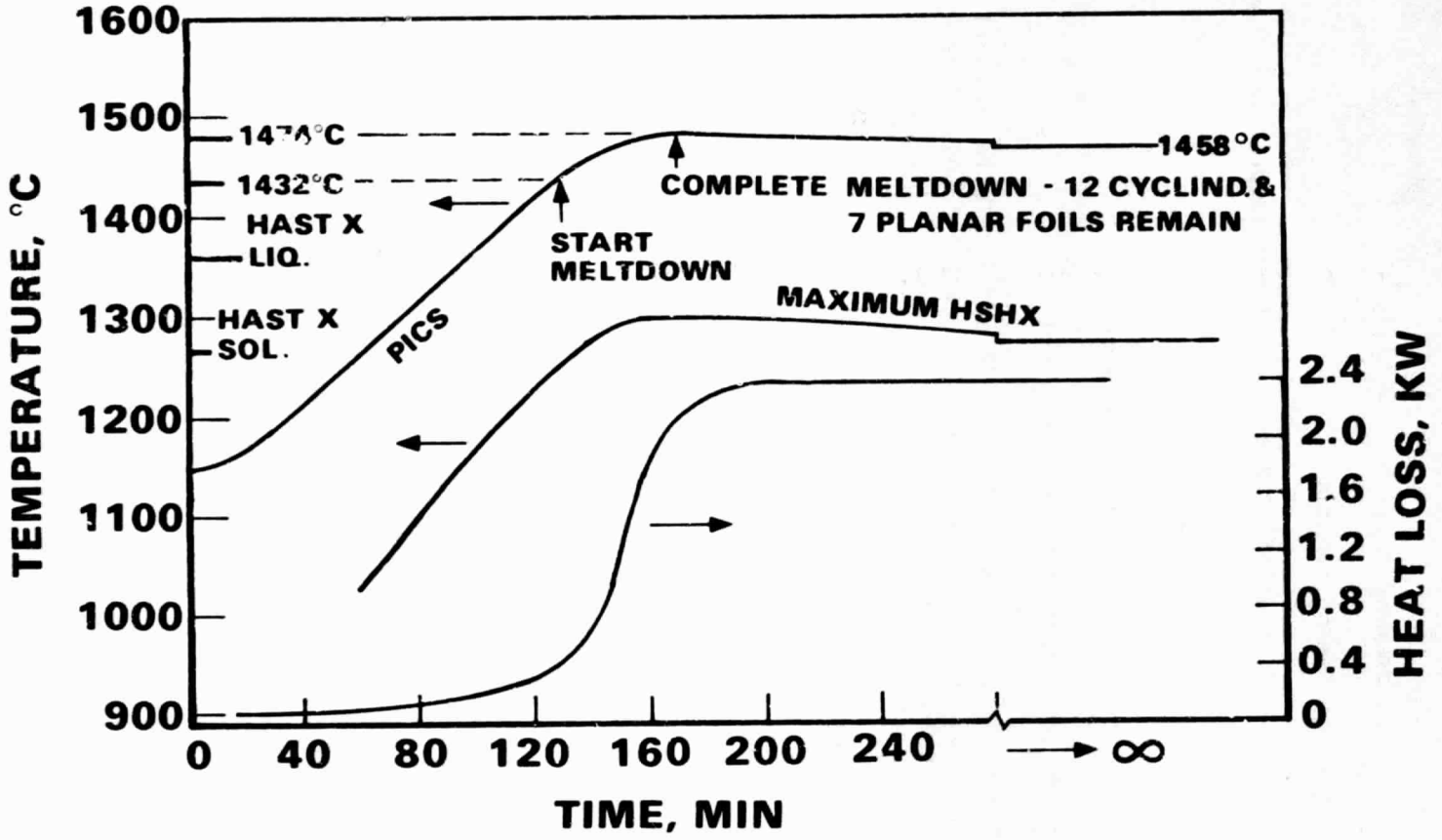

Figure 23.--ECS Meltdown Results.

foils cannot continue to increase in temperature so the meltdown is terminated. The analysis predicts that 12 cylindrical and 7 planar (end) foils remain. Due to the lumping of foil layers into packets, the next unmelted nodes contain 5 foil layers each. Thus one more melted cylindrical node would result in 7 layers remaining and one more melted planar node would result in 2 layers remaining.

The PICS temperature reaches a maximum of 1474°C at about 175 min. Since the HSA is close to steady state, the PICS temperature is only 16°C above its ultimate steady-state temperature of 1458°C. This is considerably higher than the PICS temperature limitation of 1200°C for ECS post-meltdown steady state. The absolute temperature limit during the transient of 1600°C is not approached during the meltdown.

A transient analysis was performed replacing the inner Hastelloy X insulation mandrel with a mandrel made of a material similar to the main foils (40% Ni-60% Pd). This sheet would melt during ECS operation and reduce the thermal resistance. The results indicated that 12 cylindrical and 7 planar foils remained after meltdown--exactly the same as with the Hastelloy X mandrel. Due to the removal of the mandrel as a radiation shield, the steady-state post-meltdown PICS temperature was lower by about 10°C.

To assess the influence of the heat sink temperature on the ECS operation, several analyses were performed using a sink temperature of -62°C (-80°F). Very little change was noticed for either the transient or the ultimate steady-state conditions.

Post-meltdown steady-state analyses were performed for various numbers of remaining foil layers, without regard to how the steady state was achieved. To conserve computation time, the simplified HSA model was used. The PICS and insulation temperatures for steady state are shown in table 21. It can be seen that to maintain the PICS temperature below the specified limit of 1200°C (table 1) all of the foils must be removed.

TABLE 21

ECS POST-MELTDOWN STEADY STATE

Remaining foils	PICS temp., °C	Inner foil temp., °C	
		Cylindrical	Planar
0	1160	-	-
1	1211	645	672
2	1286	878	894

The effect of foil sublimation on the ECS operation has not been analyzed. Since the vapor pressure of the Ni-Pd foils is significant at temperatures approaching their melting point, a few more foils may be lost due to sublimation. Like the melting, the foil sublimation is a self-limiting process; as a foil sublimates, the system thermal resistance decreases and the foil temperatures drop. Table 21 shows the temperatures of the innermost foil with one and two foil layers remaining. These temperatures are well below the melting point (1237°C) and the vapor pressure would be quite low. It seems very unlikely that all of the foils remaining after meltdown would be removed by sublimation, especially when giving consideration to the entire accumulated mass of the melted foils. The sublimation phenomenon is certainly an area that requires further investigation given the necessity of removing all of the foils to meet the PICS temperature requirements. The possible sublimation of the Hastelloy X HSHX and/or insulation support mandrel also should be investigated.

To attain the desired temperature level with the present type of ECS (i.e., foil meltdown) would probably require using HSIS foil material with a lower melting point than the Ni-Pd. With a lower melting point it is likely there would be a higher vapor pressure; this must not be high enough to endanger foil stability under normal operating conditions. It may also be helpful to reduce the number of foil layers used. This, of course, would tend to increase the heat leak under normal operation. The effect of such a change on the ACS would also have to be considered. The use of a fusible inner insulation mandrel should be considered as a design option.

The ECS analysis just discussed was for the reference design HSHX with an emissivity of 0.8. It appears that an untreated emissivity of 0.25 may be more desirable for the other modes of operation. This lower emissivity should be included in future ECS studies. Since the reduced emissivity increases the HSA thermal resistance, the PICS temperature problem should become more difficult unless the increase in HSA temperature causes the HSHX to exceed the Hastelloy X liquidus point. If this occurs, the HSHX is removed as a thermal barrier, reducing the HSA thermal resistance.

Results of the recent TECO "mini-meltdown" tests for Ni-Pd Multi-Foil insulation have become available (T. Ashe, BIPS-GDS Coordiantion Memo A0596, March 6, 1978). These results are essentially consistent with the transient meltdown analysis discussed in this section.

STRUCTURAL ANALYSIS DESCRIPTION AND DISCUSSION OF RESULTS

The structural analysis performed during the study concentrated on satisfying the following requirements:

Pressure Containment--The HSHX is designed for pressure containment for a 7-yr life. A maximum of 1 percent creep deformation is allowed for the required life.

Low-Cycle Fatigue--The HSA must withstand a minimum of 100 startup cycles. The analysis was limited to the HSHX.

Resonant Frequency--In accordance with the BIPS requirement, no HSA natural frequencies should be below 60 Hz to avoid any spacecraft-induced resonances.

Dynamic Loading--The HSA must withstand launch loads of shock, vibration, and acceleration without any loss in structural integrity. MIL-STD-810B is the specified requirement for dynamic loading. An equivalent static loading of $\pm$50 g, where g is the normal acceleration of gravity, was used in the analysis and compared with MIL-STD-810B.

In the calculation of structural properties for the HSHX, a design margin of 28°C (50°F) was used. Thus, for a HSHX temperature of 788°C (1450°F), structural properties at 816°C (1500°F) are used.

Pressure Containment

The HSHX is designed for pressure containment for a 7-yr life. The design allowable stress is based on 1 percent creep deformation, at the appropriate fluid pressure level, accumulated over the life of the unit.

For short-term stress, the design practice employed by AiResearch is to size the pressure-carrying structure for proof pressures of 1.5 times the working pressures and for burst pressures of 2.5 times the working pressures. The structure must not yield at proof pressure or rupture at burst pressure. This implies that the proof pressure is the governing design condition if the ratio of yield stress to ultimate stress is less than 0.6 and that the burst pressure will govern if the ratio is greater than 0.6.

When the limiting stress is due to bending, a small amount of yielding can be allowed in the outermost fibers, which leads to a modified stress distribution through the thickness. The ideal plastic bending moment is 1.5 times the computed elastic bending moment for the same peak stress. Accordingly, the allowable indicated elastic stress due to bending loads is taken to be 1.5 times the allowable values for uniform tension or compression loads.

At the elevated operating temperatures and long life requirement for the HSHX, it has been found that the creep stress is always the controlling stress. The 1 percent creep deformation criterion was used to determine the required wall thicknesses for all pressure containment components in the HSHX--tubes, elbows, and manifolds. An aging factor, F_a, and a tube weld efficiency, η, were used to reduce the allowable stress for all pressure containment designs as follows:

$$\sigma_a = \frac{\eta \sigma_c}{F_a} \tag{14}$$

where σ_a is the allowable stress and σ_c is the 1 percent creep stress for 7 yr.

The 1 percent creep stress is taken at the maximum temperature of the component including the 28°C (50°F) design margin. Potential degradation of material properties due to contamination, radiation-induced swelling, and radiation-induced creep have not been considered. An aging factor of 1.2 was assumed for all designs.

Configuration study.--For the configuration studies the long-term creep stresses were estimated from refs. 3 and 9 for the C-103 and the Hastelloy X designs, respectively. A tube weld efficiency of 0.95 was assumed for the tubes and manifolds, a resonable value for rolled and planished butt welds. The required tube and manifold wall thickness, t, is calculated by the thin-wall pressure containment relationship:

$$t = \frac{KPD}{2\sigma_a} \tag{15}$$

where K is a tube wall thinning factor

P is the design pressure containment criterion, 0.793 MPa (115 psia)

D is the tube OD

For the single-tube helical coil, the helical-flow tube bank, and the toroidal manifolds for both multitube designs, a wall thinning factor of 1.05 was assumed to account for any thinning due to tube bending. The dimpled tubes of the axial-flow tube bank design are not bent, but the dimple formation results in some wall thinning in the dimple area. For the relatively shallow dimples used in the design, AiResearch experience indicates a maximum wall thinning of around 12 percent. Thus, a K of 1.12 was used for the dimpled tube wall thickness determination.

Selected Configuration.--Required tube and elbow wall thicknesses were determined for the selected single-tube helical-coil Hastelloy X configuration for coils of various numbers of turns (see table 12). Updated creep stress properties for Hastelloy X were used (J. Hadley, BIPS-GDS Coordination Memo A0521, September 21, 1977). The 1 percent creep stress at 816°C (1500°F)--788°C (1450°F) maximum tube wall temperature plus the 28°C (50°F) design margin--is

15.2 MPa (2200 psi). In the determination of the allowable stress in eq. (14), a tube weld efficiency factor of 0.95 was assumed for the HSHX tube. In the transition elbows, which connect the tube with the BIPS ducts, the radius of curvative precludes roll planishing, so a lower weld efficiency of 0.7 was assumed. The inlet and outlet elbows were designed to have identical wall thicknesses even though the inlet elbow is at a considerably lower temperature (and hence, higher allowable stress level) than the outlet elbow. The tube wall thicknesses were calculated using eq. (15) for the design pressure containment criterion of 0.703 MPa (102 psia) and a tube wall thinning factor due to bending of 1.05.

The results of these calculations are shown in table 22. As previously discussed, an additional allowance of 5 percent was added to the minimum required tube wall thickness to account for manufacturing tolerances. This allowance is reflected in the nominal wall thicknesses listed in table 12.

TABLE 22

TUBE WALL THICKNESS

Number of turns in coil	Tube OD, cm (in.)	Minimum tube wall thickness, mm (in.)	Minimum elbow wall thickness, mm (in.)
9	4.42 (1.74)	1.35 (0.053)	2.36 (0.093)
10	3.96 (1.56)	1.22 (0.048)	2.11 (0.083)
11	3.61 (1.42)	1.12 (0.044)	1.93 (0.076)
12	3.30 (1.30)	1.02 (0.040)	1.75 (0.069)
13	3.05 (1.20)	0.94 (0.037)	1.63 (0.064)

As a check on the selected 10-turn design, a three-dimensional thin-shell finite-element model was constructed and the pressure containment stress calculated using the ANSYS computer program. The ANSYS is a general-purpose finite-element computer program used for stress and vibration analysis. The program is discussed in appendix C. The model was for a single turn of the HSHX with boundary conditions applied to simulate the effects of the continuous tube. A model also was constructed for the transition elbows. The tube and elbow models are shown in figs. 24 and 25, respectively.

The results of the ANSYS analysis substantiated the 10-turn minimum wall thickness calculation and verified the applicability of eq. (15).

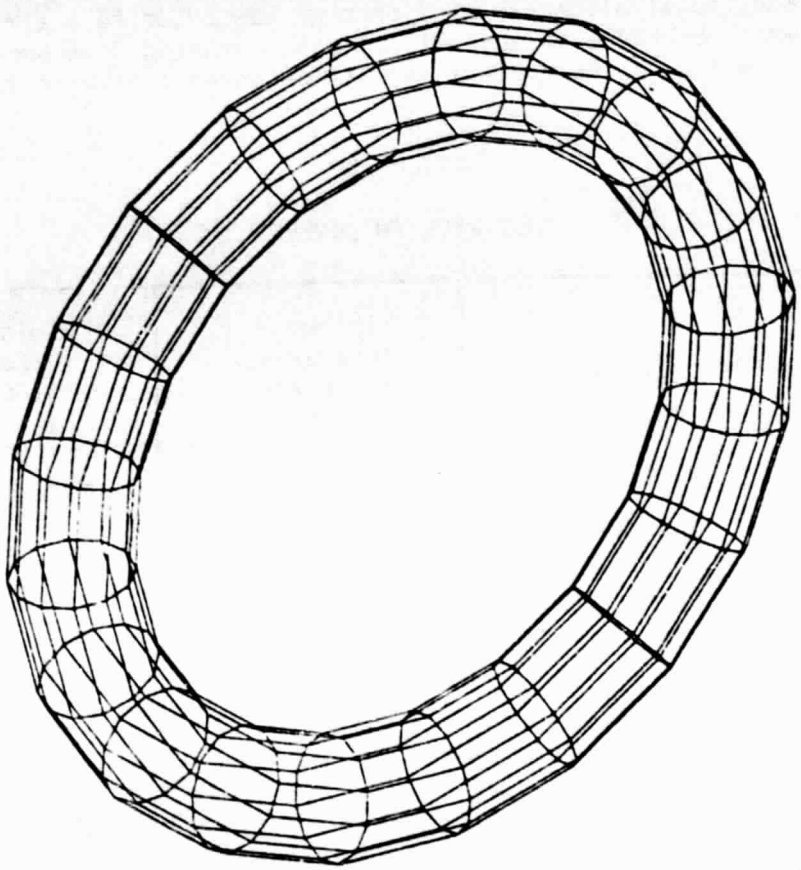

S-23798

Figure 24.--Coil Finite-Element Model.

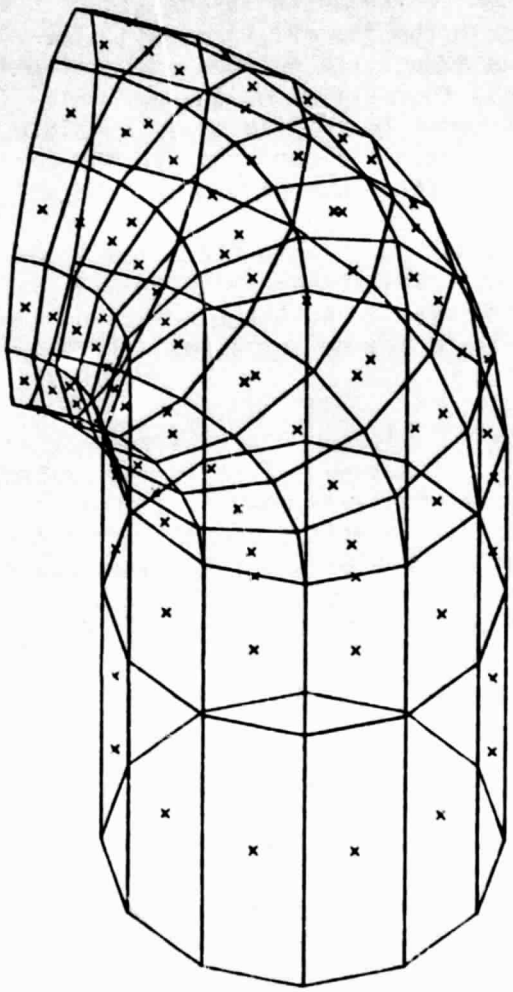

S-18236

Figure 25.--Elbow Finite-Element Model.

Thermal Stresses and Low-Cycle Fatigue

The HSA has a requirement for a minimum of 100 startup cycles without evidence of fatigue cracking. The present analysis concentrated on the LCF life prediction of the HSHX. The temperature profiles calculated from BIPS startup transient Run 600 were used as inputs to the thermal stress computations (see the thermal analysis section).

A finite-element model of the HSHX was constructed for use with the ANSYS computer program to compute the thermal stresses. The HSHX has a continuous strip that slips into the separation between successive turns of the coil and is brazed to the coil (see the system design section). The brazed strip is implemented in the ANSYS model by the use of appropriate boundary conditions at the required angular location of each turn in the coil. The brazed joint is assumed to have a braze efficiency of 0.5. The model is shown in fig. 26.

Thermal stresses are set up in both the axial (flow) and circumferential directions around the tube. The steady-state thermal stresses are relatively low, well below the yield stress. With the expected stress relaxation, it appears that the steady-state thermal stresses will not impact on the required 7-yr life.

The transient analysis indicates that the most critically stressed region of the HSHX is the inlet to the tube. This is due primarily to the large circumferential temperature gradients resulting from the cold inlet fluid temperature (see the thermal analysis section). It can be seen from fig. 22 that the largest temperature gradients at the inlet end occur around 180 sec. Although the yield stress is lower at the outlet (hot) end, the smaller temperature gradients result in less critically stressed regions. The axial temperature gradients produce much smaller stresses; the maximum axial thermal stress is only about one-seventh of the maximum circumferential thermal stress.

The maximum combined thermal stress due to circumferential and axial temperature gradients is only about 50 percent of the yield stress at the inlet end. In the absence of stress concentration effects, there would be no plastic strains generated. However, the LCF life of the HSHX will be limited by the repetitive creep relaxation; to account for the relaxation a stress concentration factor of 3 was assumed. This large value was assumed so as to include the effects of the local changes in coil thickness produced by the continuous braze strip and the HSHX mount brackets.

Based on a comparison with a fatigue life study conducted under a DOE contract (ref. 10), an LCF life of 570 startups is predicted. This is well above the HSA requirement of 100 cycles. The fatigue failure location is at the braze joint at the cold end of the tube. It should be noted, however, that only the startup portion (Run 600) of a complete cycle was considered. Reductions in fatigue life due to other modes of operation (e.g., steady state, HSA fueling transient, etc.) have not been included. These effects are expected to be small.

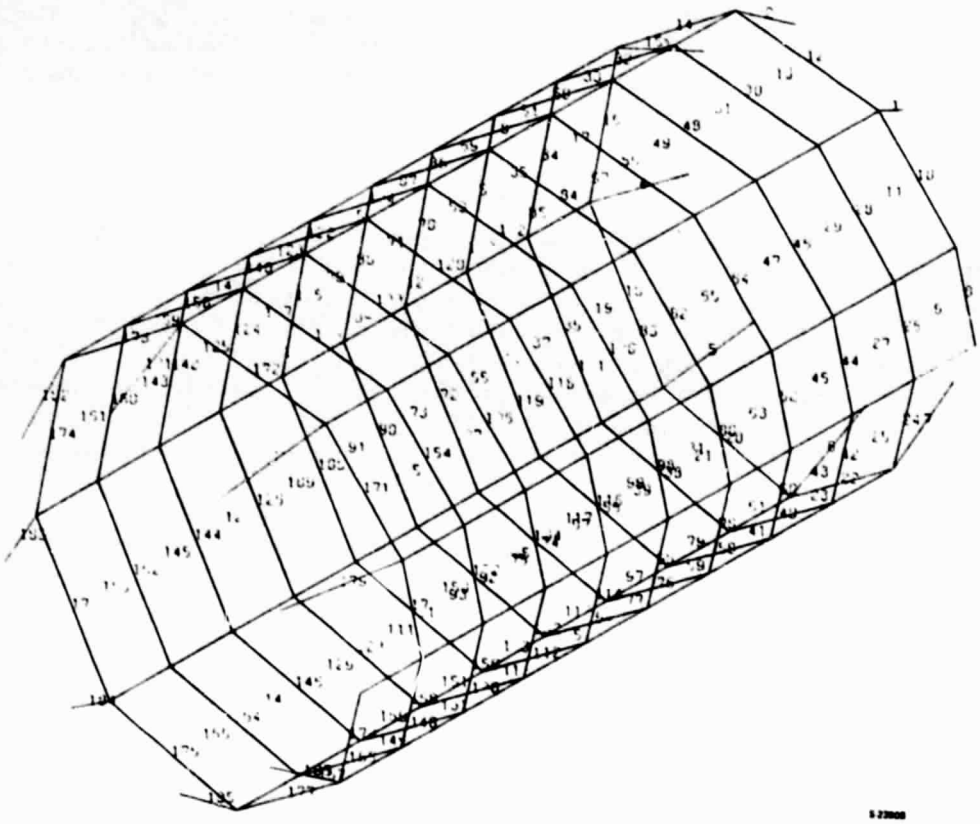

Figure 26.--HSHX ANSYS Model.

Resonant Frequency

The BIPS has the requirement to maintain all HSA natural frequencies above 60 Hz to avoid any possible coupling with spacecraft frequencies. This requirement, as applied to the HSHX, was the main driving force in the selection of the continuous brazed strip design for the coil, as the natural frequency of the free coil is below 60 Hz. The brazed strip has the additional advantages of taking up the unwinding load due to the Bourdon effect of the internal pressure, significantly reducing the bending stress in the tube, and helping to maintain direct alignment. The selection of the continuous brazed strip coil design is discussed in ref. 10. The effort in this study concentrated on determining the natural frequencies of the HSA at the HSHX mounts, ensuring that all modes exceed the 60 Hz minimum, and comparing these frequencies with the calculated natural frequencies of the HSHX.

A finite-element computer model of the HSHX was constructed to determine the dynamic response of the unit. The model is similar to that shown in fig. 26. The forward and aft brackets that attach the heat exchanger coil to the HSA were modeled as three-dimensional beams with stiffnesses equivalent to the brackets. The beam elements were assumed to be held in the radial and axial directions but were free to rotate at the aft graphite plate. The forward beam elements were allowed to move freely in the fore and aft direction and to rotate freely, but were held in the radial directions by the attachment to the forward graphite plate in the HSA. The coil itself was modeled using three-dimensional curved tubular elements. The coil-to-coil brazed strips were simulated by connecting the coils with shell elements. The axial and bending stiffnesses of the shells were made equal to the stiffness of the tubes for resisting axial and bending loads with the brazed strip between coils. The density of the shell elements was set to yield the weight of the brazed strip.

The model was run on the ANSYS computer program to determine the HSHX resonant frequencies. The results for the first few natural frequencies are given in table 23.

TABLE 23

HSHX NATURAL FREQUENCIES

Mode	Frequency, Hz
Lateral bending mode (bending of coil)	261
Axial mode (resonance of mount brackets)	342
Lateral rocking mode (side displacement of brackets)	648
Undefined higher order modes	734

The first and third modes are illustrated in figs. 27 and 28, respectively. As can be seen from table 23, all natural frequencies of the HSHX are well above 60 Hz.

A finite-element model of the entire HSA was constructed to determine the HSA natural frequencies at the HSHX mount points. The model representation and restraints are summarized in table 24.

TABLE 24

HSA DYNAMIC MODEL REPRESENTATION AND RESTRAINTS

HSA feature	Model representation	Model restraint
Forward and aft end domes	Shell elements	Center of aft dome fixed in X-Y (lateral) plane to simulate mount.
Outer shell	Shell elements	Outer shell, forward dome, and spider fixed in X-Y-Z directions at three locations to simulate ball joint suspension.
Forward and aft spiders (end enclosures)	Central hub as shell element joined to outer shell with six 3-D beam elements	Beams coupled to outer shell in X-Y-Z directions but free to rotate.
Preload screws	Shell elements in conical shape	Rigid attachment to spider; 12 compression-only spar elements at graphite shoe interface (Z direction). Coupled to graphite shoe in X-Y plane (lateral restraint).
Graphite shoes	24 shell elements	Graphite shoe - IHS interface: 12 compression-only spar elements restrained in X-Y plane to represent socket design.
IHS	12 shell elements modified to represent actual weight and stiffness	
HSHX	8 shell elements modified to represent actual weight and stiffness	Aft graphite shoe: coupled in the X-Y-Z directions. Forward graphite shoe: coupled in the X-Y plane only.

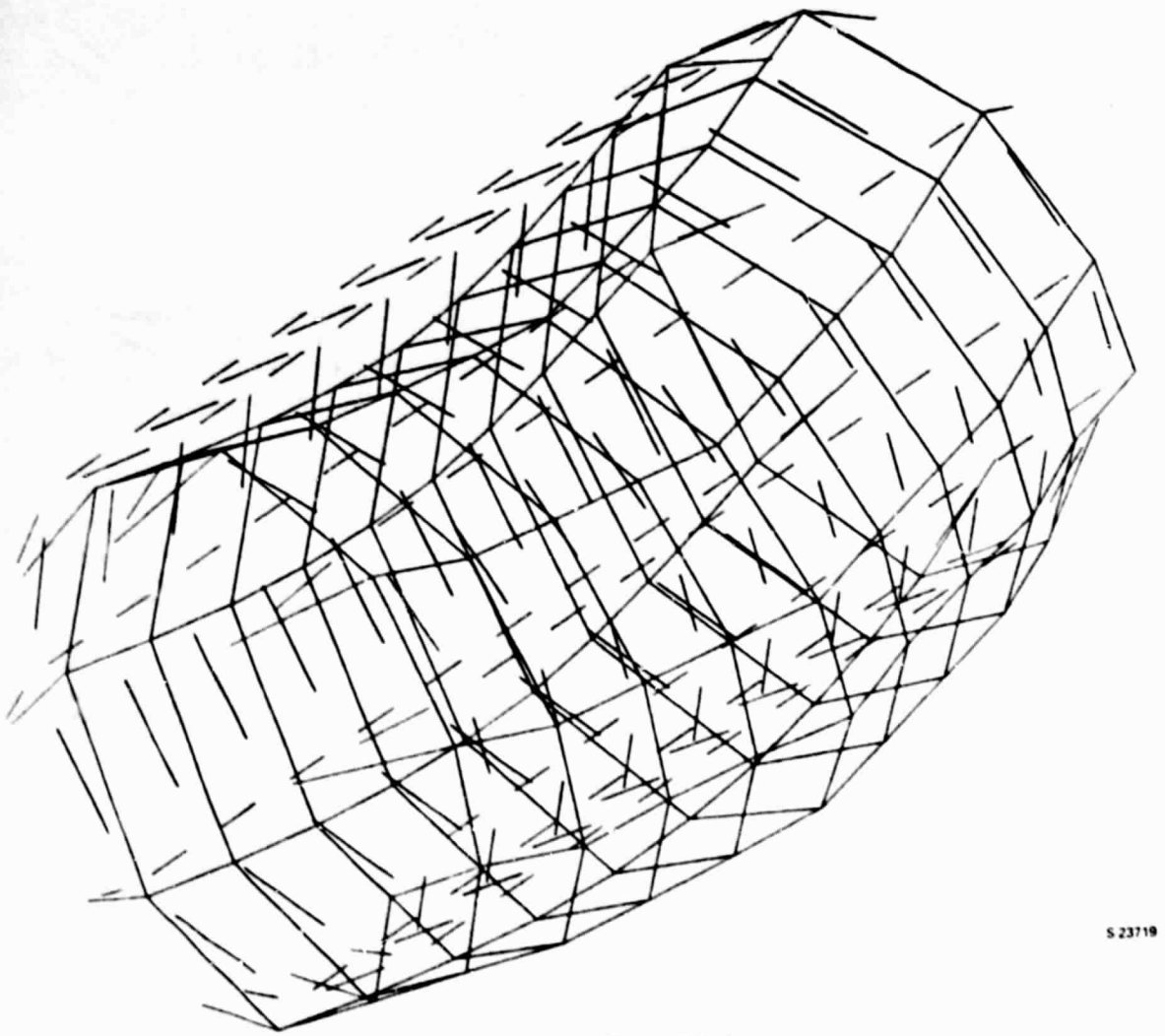

Figure 27.--HSHX Lateral Bending Mode.

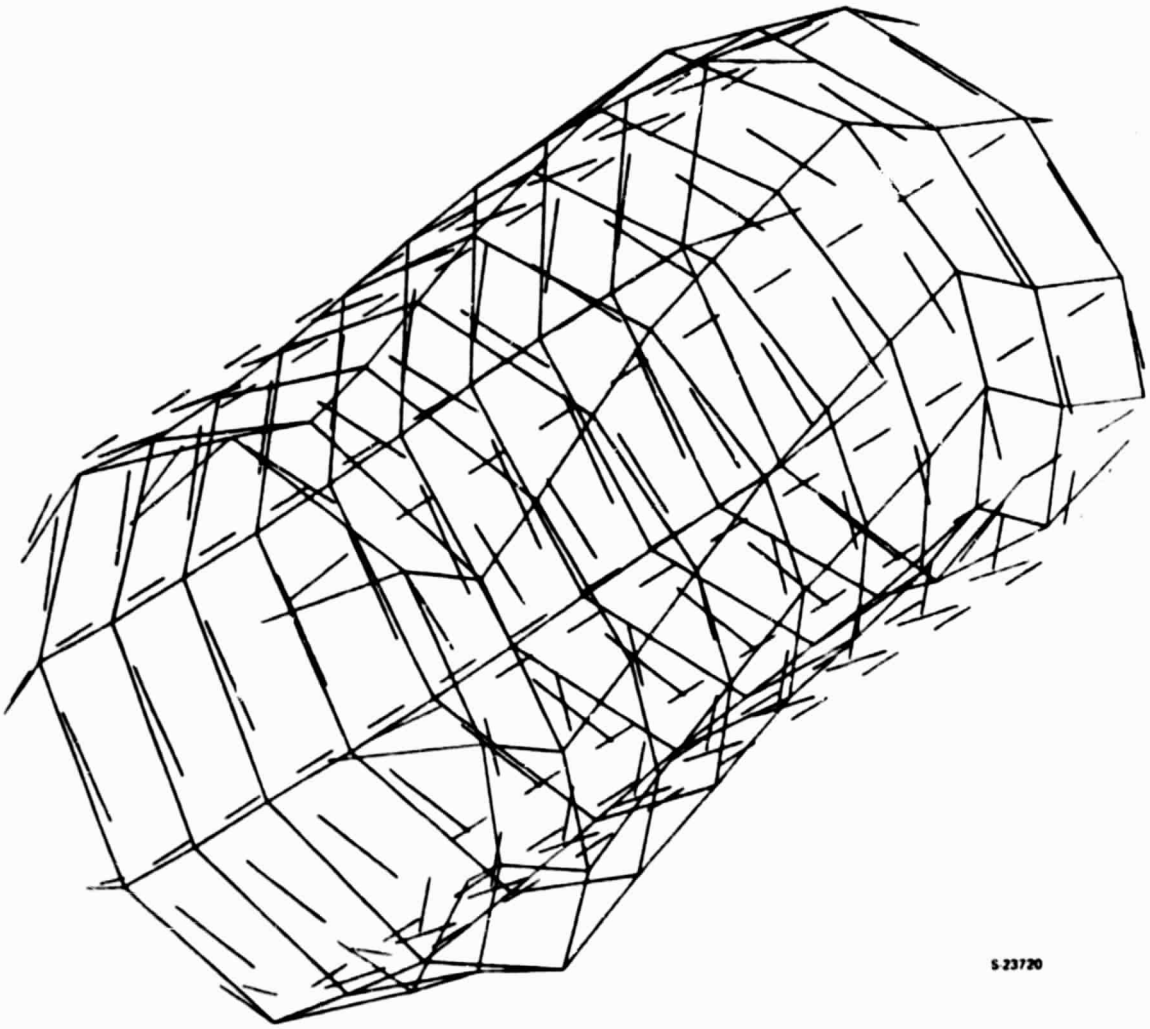

Figure 28.--HSHX Lateral Rocking Mode.

The model was run on the ANSYS computer program to determine the HSA natural frequencies at the attachment points of the HSHX to the aft (outlet) graphite support plates. The frequencies are listed in table 25.

TABLE 25

HSA NATURAL FREQUENCIES AT FT END

Mode	Frequency, Hz
Torsional mode (central mass rotating with legs of spiders acting as springs)	28
Axial mode (central mass moving axially with legs of spider acting as springs)	92
Lateral rocking mode (central mass moving laterally with trunnion action of preload screws causing spider to distort)	330
Undefined higher order modes	754

The lateral mode is illustrated in fig. 29.

The torsional mode natural frequency is below the design goal of 60 Hz. In addition, a comparison of tables 23 and 25 indicates the possibility of mode excitation of the axial mode of the HSHX (342 Hz) by the lateral rocking mode of the HSA (330 Hz). This could occur even though the two mode shapes are different. The fourth modes of the HSA (754 Hz) and the HSHX (734 Hz) are close together; however, these modes are complex and will be difficult to excite. In addition, these frequencies are above the anticipated sinusoidal excitation range for the HSA of 2 to 500 Hz. No coupling seems possible between any other modes.

To increase the natural frequency of the torsional mode of the HSA, it is proposed to add material to the spokes of the spiders (end enclosures) to increase their lateral stiffness. Analysis indicated that increasing the average width of the spokes from 1.63 cm (0.64 in.) to 2.64 cm (1.04 in.) would be sufficient to raise the natural frequency to 60 Hz. The additional material also would increase the stiffness of the spokes, and hence natural frequency, in the axial and lateral directions. The HSA natural frequencies for the modified end enclosures are presented in table 26. The unmodified HSA natural frequencies from table 25 and the HSHX natural frequencies from table 23 are included for comparison.

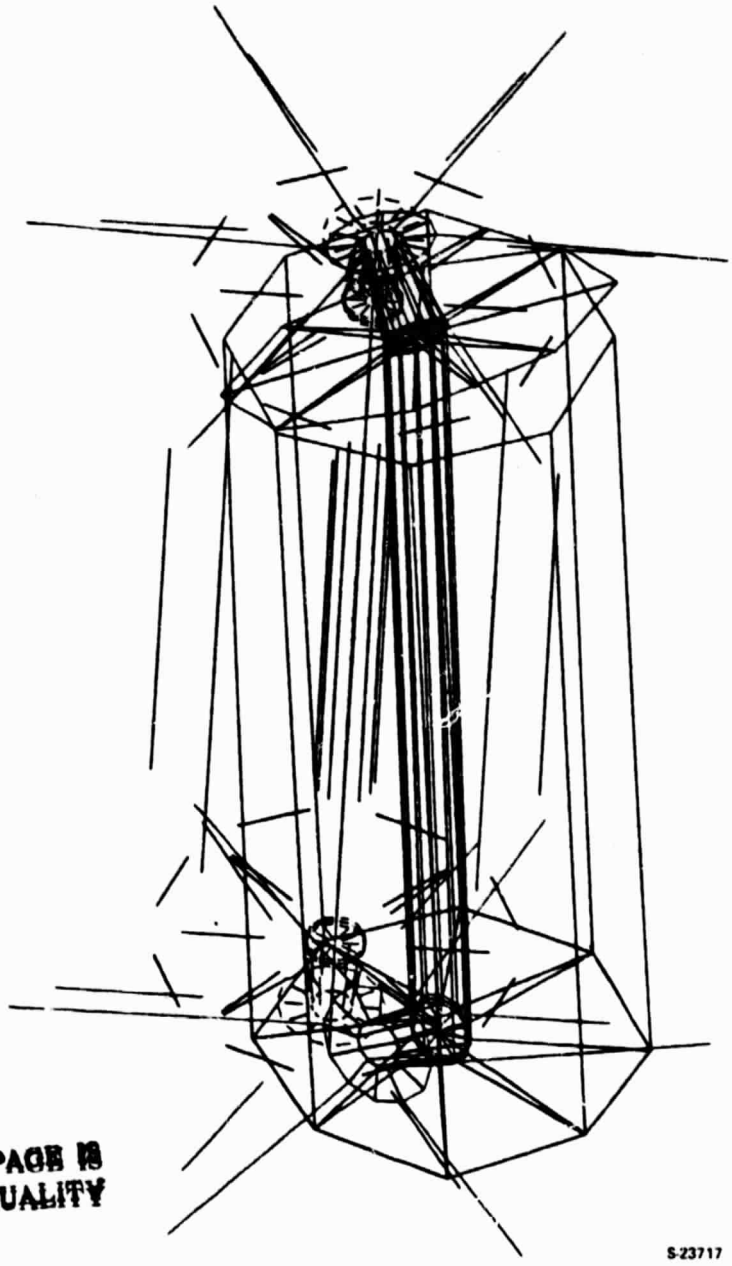

Figure 29.--HSA Lateral Rocking Mode.

TABLE 26

NATURAL FREQUENCY SUMMARY

HSA			HSHX	
Frequency, Hz		Vibration mode	Frequency Hz,	Vibration mode
Original	Modified			
28	60	Torsional	261	Lateral (bending)
92	118	Axial	342	Axial
330	420	Lateral (rocking)	648	Lateral (rocking)

Since the resonant frequency of the lateral rocking vibration mode of the HSA increased to 420 Hz, the possibility of coupling between the HSA and the HSHX has been eliminated. It is recommended that the end enclosure modification be made to the HSA design.

Dynamic Loading

The HSA must withstand launch loads of shock, vibration, and acceleration without any loss in structural integrity. The requirement for dynamic loading is MIL-STD-810B, except that the damping ratio is specified as 5 percent. To simplify the computations, an equivalent static loading in terms of g levels was assumed. A level of $\pm$50 g was used. This level was shown to be well above the maximum response from the MIL-STD-810B inputs. The temperatures used for the determination of the allowable stresses were those just prior to launch, i.e., the ACS temperatures shown in fig. 18. The 28°C (50°F) design margin was applied.

The finite-element model of the HSHX (see fig. 26) was used to determine the loads at the HSHX mount points due to the application of 50-g static loads in the axial ($\pm$Z) and two radial directions ($\pm$X and $\pm$Y). The aft (hot end) mount points for the HSHX were assumed to be restrained in the axial, radial, and tangential directions. The forward (cold end) mount points were assumed to be restrained in the radial and tangential directions only. The loads at the aft end were found to be greater than those at the forward end. The calculated loads are presented in table 27.

These loads were applied to the HSHX mount brackets and to the combined IHS and HSHX support plate in the HSA finite-element model (see table 24) to determine the structural integrity for the anticipated dynamic loading. For the support plate, it was assumed that any dynamic loading applied by the IHS would be transferred through the center portion of the plate to the preload screw without affecting the stresses in the plate produced by the HSHX loading around the outer edge of the plate.

TABLE 27

LOADS AT AFT HSHX MOUNT POINTS

Mount point	Applied mount point loads																	
	50 g + X (lateral)						50 g + Y (lateral)						50 g + Z (axial)					
	Radial		Tangential		Axial		Radial		Tangential		Axial		Radial		Tangential		Axial	
	N	lbf	N	lbf	N	lbf	N	lbf	N	lbf	N	lbf	N	lbf	N	lbf	N	lbf
1	-22	-5	734	165	627	141	405	91	-667	-150	-142	-32	307	69	320	72	823	185
2	107	24	316	71	187	42	-58	-13	49	11	-672	-151	351	79	-9	-2	649	146
3	36	8	302	68	489	110	31	7	694	156	-280	-63	329	74	-22	-5	640	144
4	-22	-5	-276	-62	507	114	36	8	721	162	178	40	294	66	-22	-5	636	143
5	-53	-12	-658	-148	214	48	-13	-3	285	64	516	116	276	62	-13	-3	648	146
6	-18	-4	-645	-145	-200	-45	-58	-13	-334	-75	565	127	214	48	13	3	609	137
7	44	10	-236	-53	-562	-128	-209	-47	-694	-156	-165	-37	316	71	-191	-43	1081	243

The calculated stresses are presented in table 28. Also shown are the design allowable stresses and the margins of safety, defined as the difference between the allowable stress and the calculated stress divided by the calculated stress. Thus, a positive margin of safety represents an adequate design.

It can be seen that the HSHX mounting brackets and the combined IHS and HSHX support plate are adequate to meet the 50-g equivalent loading.

As a check on the adequacy of the 50-g equivalent load assumption, the finite-element model of the HSA was modified to reflect the recommended modification to the end enclosures and an analysis was conducted to determine the response at the HSHX mount points with the launch, liftoff, and boost sinusoidal inputs from MIL-STD-810B applied to the HSA mounts. The frequencies of interest were 60 Hz and 118 Hz for the HSA, and 261 Hz and 342 Hz for the HSHX. The sinusoidal input at these frequencies is taken from MIL-STD-810B as ± 3.5 g. The load path from the HSA mounts to the HSHX mount points involves several joints that can provide damping. The specified damping factor of 5 percent was thought to be conservative and was used for the analysis. The response at the HSHX mount points was determined for both axial and lateral excitation. The results of this analysis are summarized in table 29.

TABLE 29

HSHX MOUNT RESPONSE TO MIL-STD-810B INPUTS

Excitation direction	Frequency, Hz,	Input to HSA, g	Response at HSHX mounts,[a] g	Amplification factor
Axial (Z)	60	3.5	5.6	1.6
	118	3.5	15.1	4.3
	261	3.5	1.8	0.5
	342	3.5	1.3	0.4
Lateral (X)	60	3.5	3.6	1.03
	118	3.5	4.0	1.15
	261	3.5	6.7	1.92
	342	3.5	7.8	2.22

[a]With 5 percent damping

The maximum amplification between the HSA mounts and the HSHX attachment points is 4.3 at the 118-Hz axial resonant frequency of the HSA. The maximum amplification at the HSHX resonant frequencies is 2.22. These amplification factors result in a 15.1-g maximum load at the HSA-HSHX interface. This load is well below the 50-g equivalent design load used for the analysis of the HSHX mount brackets and the HSA support plate (see table 28).

TABLE 28

STRESS SUMMARY FOR 50-g EQUIVALENT LOADING

Component	Type of stress	Material	Design criterion	Applied stress		Margin of safety
				MPa	psi	
Pin, 4.78 mm (0.188 in.)	Bending	Waspaloy	Endurance limit 310.3 MPa (45 000 psi)	279.6	49 560	0.11
Bracket, 4.06 mm (0.16 in.)	Bending	Hastelloy X	Bearing yield 335.4 MPa (48 640 psi)	139.1	20 180	1.41
Bracket weld 2.79 mm (0.11 in.)	Bending	Hastelloy X	Endurance limit[a] 135.1 MPa (19 600 psi)	67.1	9 730	1.01
Braze at base	Tension	Palniro 7	Endurance limit[a] 34.5 MPa (5 000 psi)	11.9	1 730	1.89
Aft support plate	Bending	Poco graphite AXF-5Q	Endurance limit[a] 77.6 MPa (11 250 psi)	56.1	8 140	0.38
Aft support plate	Bearing	Poco graphite AXF-5Q	Bearing yield[b] 103.4 MPa (15 000 psi)	47.7	6 920	1.17
Aft support plate	Shear	Poco graphite AFX-5Q	Shear yield[c] 51.7 MPa (7 500 psi)	4.8	690	High

[a]Estimated endurance limit = 0.75 x yield stress.

[b]Estimated bearing yield = yield stress.

[c]Estimated shear yield = 0.5 x yield stress.

SYSTEM DESIGN

Design Description

The design effort in this study concentrated on the HSHX and the HSHX mounts. The remainder of the HSA, except for minor modifications, was assumed to be similar to its present design as specified by the General Electric Company HSA drawings.

The key recommended HSA modification is the increase in thickness of the spokes of the end enclosures (spiders) to increase the natural frequency of the HSA at the HSHX mount points (see the structural analysis section). A sketch of the end enclosure is shown in fig. 30. No specific recommendations have been made for modification of the HSIS, presently composed of 60 layers of Multi-Foil insulation. It does appear, however, that changes will have to be made in order to meet specified PICS temperature limits for ECS operation.

The HSHX is a single-tube Hastelloy X helical coil with 10 complete turns. The tube is 3.96 cm (1.56 in.) OD with a 1.30 mm (0.051 in.) wall thickness. The reference design HSHX is surface treated (roughened and oxidized) to an emissivity of 0.8. The transition elbows between the HSHX and the BIPS ducts are short Hastelloy X sections, the same OD as the tube but of 2.54 mm (0.100 in.) wall thickness. Reinforcement strips are brazed between the last two turns at each end of the coil near the elbows to prevent excessive bending in the tubing.

The HSHX is coiled such that there is a nominal clearance between turns of 0.71 mm (0.028 in.). A continuous Hastelloy X strip, 4.83 mm (0.19 in.) wide, is positioned in the clearance region and brazed to the coil. The brazed strip adds necessary structural rigidity to the coil. A sketch of the brazed coil assembly is shown in fig. 31.

The aft HSHX mounting assembly is shown in fig. 32. The forward mounting assembly is similar but has 8 mounting brackets rather than 7. The entire mount assembly is Hastelloy X except for the pin, which is Waspaloy. Several other minor changes were recommended during a previous study for DOE and are discussed in ref. 10.

Photographs of the HSHX assembly, including the mounts, are shown in fig. 33.

A design layout for the entire HSA, with emphasis on the HSHX, has been prepared and is included as fig. 34 at the end of this report.

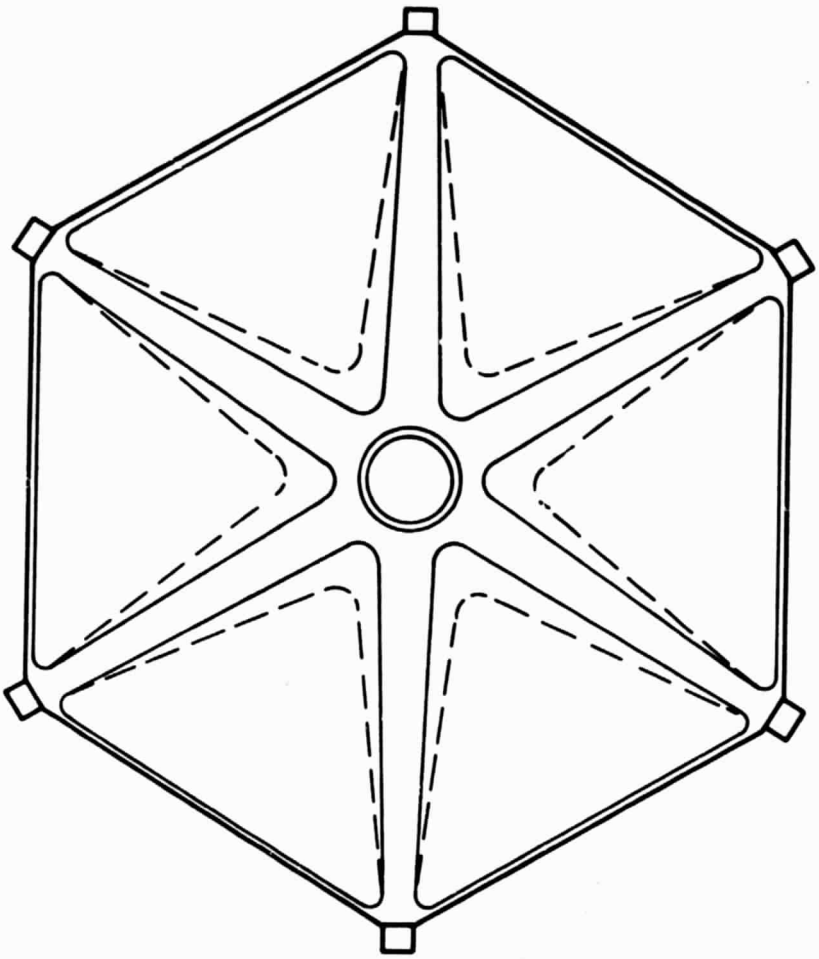

SOLID LINES: ORIGINAL DESIGN
DASHED LINES: MODIFIED DESIGN

S-26470

Figure 30.--Proposed End Enclosure Modification.

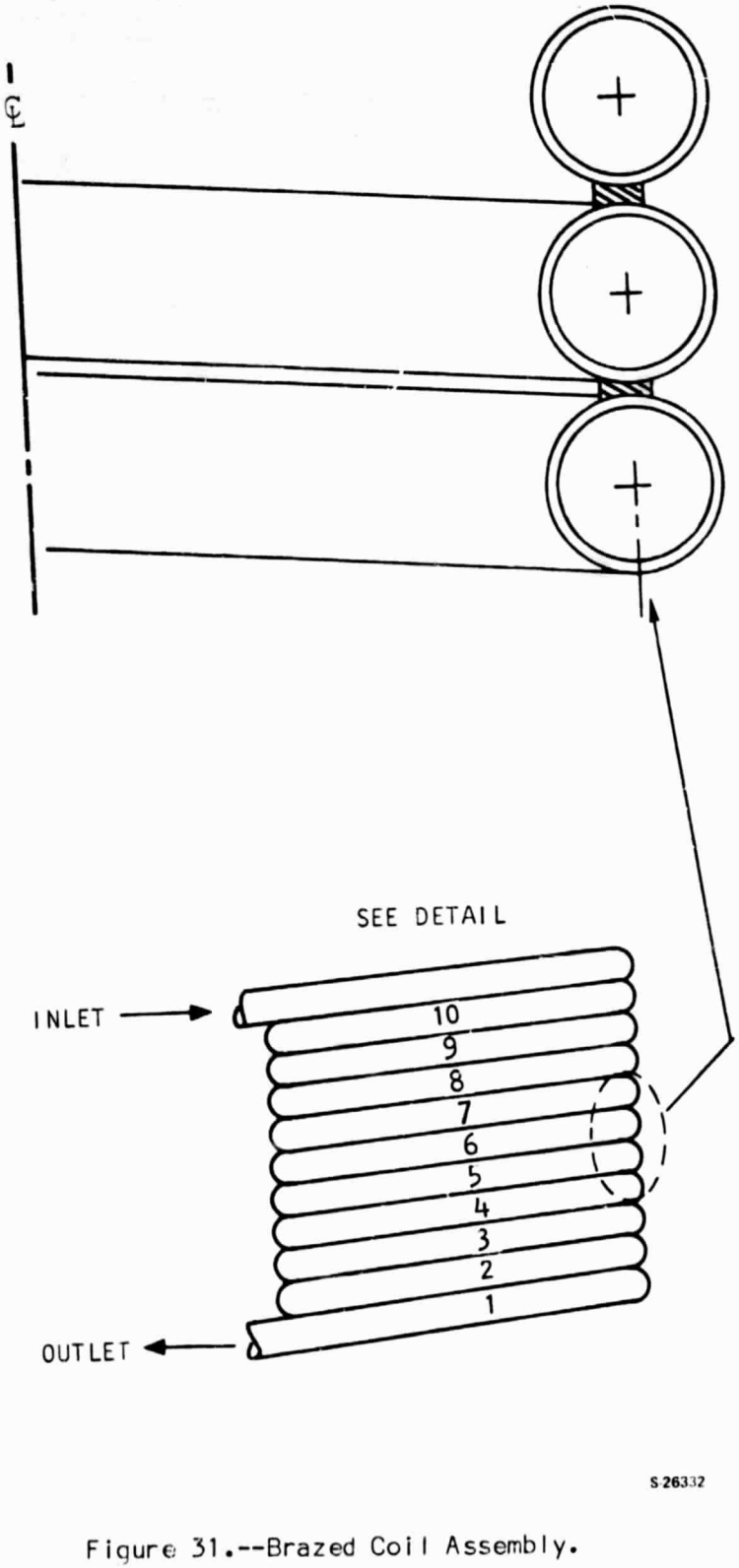

Figure 31.--Brazed Coil Assembly.

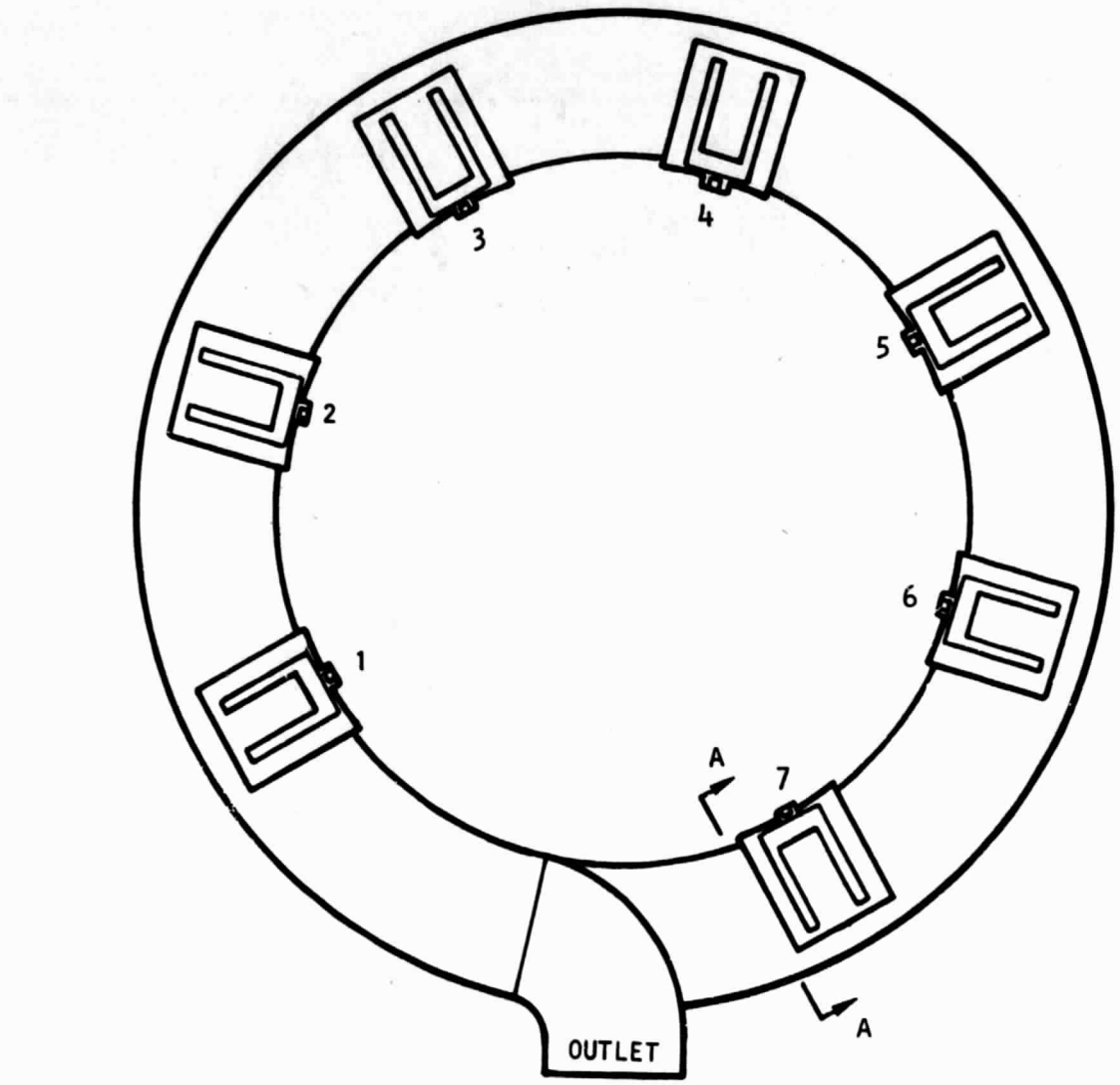

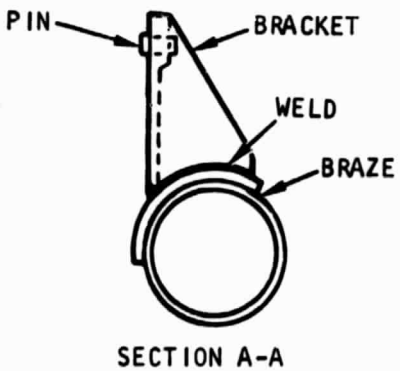

S-25250

Figure 32.--Aft HSHX Mounts.

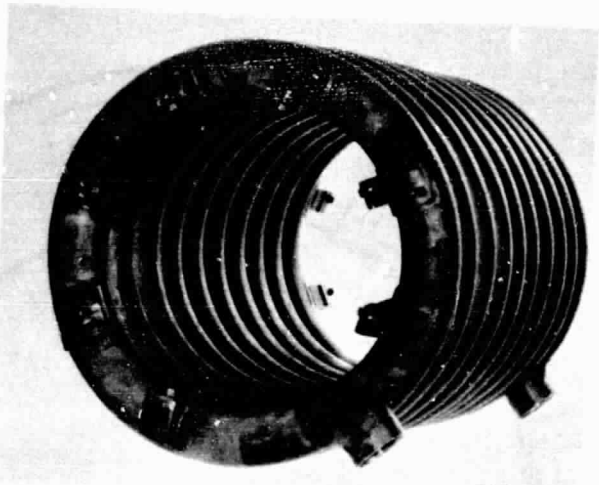

P60594-2

P60594-1 F 26929

Figure 33.--HSHX Assembly.

ORIGINAL PAGE IS OF POOR QUALITY

HSHX Manufacturing Procedure

The welded and drawn Hastelloy X tubing should be inspected visually and radiographically to ensure that there are no significant material flaws. Traceability and lot control should be established. The tube is then formed into a coil with particular attention paid to avoiding flat spots and unacceptable wall thinning due to bending. The transition elbows are then welded to the coil. Visual and radiographic inspections should be conducted to control and verify weld integrity. A helium leak test should be performed at ambient conditions to ensure integrity of the entire tube.

Assembly of the HSHX is expected to utilize two braze cycles. For the first braze, the continuous coil strip and the reinforcement strips are brazed to the tube using the gold-based brazing alloy, Palniro 1. During brazing of the coil, special fixtures should be employed to hold proper coil dimensions and maintain the continuous strip in its proper location. The brazing is performed in a vacuum furnace at around 1132°C (2070°F). The mounting brackets are joined to the coil in the second braze cycle, using another gold-based braze alloy, Palniro 7, which has a lower melting point than Palniro 1. Prior to this second braze, the bracket assembly is contoured and positioned against the coil and the brackets tack welded to ensure proper location during the braze cycle. The braze is performed at around 1052°C (1425°F).

Following the brazing operations, detailed radiographic inspections should be performed to verify braze quality. After inspection, installation of the mounting pins and final machining operations are completed. The pins are installed after brazing to avoid any changes in the Waspaloy heat treatment. The mounting pins are tack welded to the brackets.

After all manufacturing processes are complete, acceptance tests should be performed to verify unit integrity and operation. These should consist of an isothermal pressure drop test and a proof pressure test. An additional helium leak test should be performed at ambient conditions.

HSHX assemblies of this design have been fabricated for use in the BIPS ground demonstration system (GDS). The basic manufacturing feasibility has, therefore, been verified. The coil-forming process required development because of the combination of tight coil radius and multiple-turn configuration. Satisfactory parts were produced by repeatable procedures and are used in the GDS HSHX assemblies.

Heat Source Assembly Weight

The expected HSA weights are listed in table 30. The weights are for the reference design HSHX. The recommended modifications to the HSA end enclosures are included. Excluding the IHS, the heaviest components, and hence those with the greatest weight savings potential, are the HSHX and the

TABLE 30

HSA WEIGHT SUMMARY

	kg	lb
HSHX	10.07	22.20
Housing assembly	3.23	7.11
Insulation cylinder	7.03	15.49
Insulation ends	1.41	3.10
End enclosures	2.26	4.98
Preload screws	0.29	0.65
Domes	1.21	2.66
Miscellaneous hardware	3.18	7.01
Subtotal	28.68	63.20
IHS	18.82	41.50
Total	47.50	104.70

HSIS. The HSHX is designed for the three-HSA pressure containment criterion of 0.703 MPa (102 psia). The reference cycle and the expected deployment of the HSHX is for a two-HSA system, with a maximum pressure of 0.4267 MPa (61.89 psia). Although the flexibility of having a HSHX usable for either a two-HSA or three-HSA system is advantageous, it may be worthwhile to reduce the pressure containment criterion to the two-HSA working pressure. This would introduce a potential weight savings of 4.5 to 5.9 kg (10 to 13 lb) for each HSA.

The number of foil layers in the HSIS has not been optimized. A trade-off study between number of layers and HSA heat loss might suggest a fewer number of foils and hence, a weight savings. The inner and outer Hastelloy X insulation mandrels make up a significant portion of the HSIS weight. Thinning or hollowing of the mandrels could result in a reasonable weight savings.

RECOMMENDED WORK

Future work in the following areas is considered to be of importance to the final design of the HSA and the verification of system performance.

Analytical Work

Investigation of the BIPS startup transient, HSA fueling, and ECS operation for a HSHX with a surface emissivity of 0.25 (untreated).--This emissivity has been shown to be advantageous for maintenance of the PICS lower temperature requirement for normal operation and ACS deployment.

Tradeoff study to optimize the HSIS for normal operation.--HSIS weight (number of foil layers) should be varied to determine the effect on HSA heat loss. Tradeoff factors would have to be supplied by the BIPS program office. The effect of varying the number of foil layers on the other modes of system operation must be considered.

Investigation of HSA cooling prior to BIPS startup.--The latest conception of the BIPS flight system eliminates the cocoon surrounding most of the HSA and BIPS components. This results in a surface cooling requirement for the entire HSA during launch pad ACS operation to meet the exposed surface temperature limitation. In addition, a maximum heat dump limitation to the spacecraft may require cooling of the HSA both on the launch pad and in space prior to startup. The various cooling requirements need to be integrated and a heat exchanger designed to provide this cooling (probably a coil wrapped around the outside of the HSA case).

ECS operation.--The thermal analysis conducted during this study indicates that the PICS temperature limitation for the post-meltdown steady-state condition cannot be met by the present ECS. Lower melting point foil materials should be investigated in an effort to melt more of the foils. Combinations of higher and lower melting point foils might be used and the overall number of layers could be reduced. A detailed effort should include the effects of foil sublimation, which may reduce the number of foil layers remaining after an extended period of time. Revision of the thermal model to include a single mode for each foil layer may be worth the resulting cost in computer time due to the increase in accuracy.

If the PICS temperature goal cannot be met using the foil meltdown ECS, alternate ECS concepts might be investigated. This might be necessary, since essentially all of the foils must be removed to reach the steady-state PICS temperature limit. Most of the alternate systems involve the bulk removal of the foil insulation. These methods have the advantage of decoupling the HSIS and the ECS, thus allowing greater flexibility in HSA optimization. Foil removal by meltdown would act as a backup for any alternate ECS.

Investigation of other operating conditions.--A matrix of potential operating conditions for the BIPS flight system is available. Some of these

operating conditions may warrant complete thermal analysis for prediction of PICS temperatures or as inputs to a structural analysis.

Increase in turbine inlet temperature by shielding of the HSHX.--By shielding or insulating the hot end of the HSHX, more of the heat released by the fuel is absorbed in the colder regions of the heat exchanger. The total heat absorbed by the working fluid will be essentially unchanged, since the HSIS effectively determines the HSA heat losses. Thus, the HSHX outlet temperature can be increased with no increase in maximum tube wall temperature. The shielding acts as a re-radiating surface for the heat emitted by the fuel; the re-radiated energy is eventually absorbed in the colder HSHX region.

Various shielding schemes should be investigated for both physical arrangement and fluid temperature increase. The optimum situation for fluid temperature would be to distribute the heat so the entire heat exchanger surface facing the IHS is at a uniform temperature. The heat flux at the hot end of the HSHX would be very small, so that the fluid outlet temperature could be very close to the maximum wall temperature. This uniform wall temperature condition might be approached by telescoping the insulation around the HSHX, with few layers of insulation in the inlet (cold) region and a greater number of layers in the outlet region.

The shielding may have some unfavorable effects on the system, such as increasing the PICS temperature and increasing the circumferential temperature gradient in the cold end of the HSHX. These potential effects would have to be carefully investigated.

Structural analysis.--Further analytical work would appear to be necessary if a more accurate assessment of LCF life of the HSHX is desired. More detailed characterizations of the localized stresses in the HSHX coil and mount interfaces would be desirable. The thermal stresses produced during the HSA fueling transient have not been evaluated for their effect on fatigue life. In addition, structural analyses could be performed for other BIPS flight system operating modes.

The fatigue life of the remainder of the HSA has not been investigated in detail. An area of particular interest is the response of the graphite support plates during the HSA fueling. Imperfect thermal contact between the plates and the IHS may cause significant thermal gradients and stresses in the support plate. An investigation of the proposed flight system operating matrix may indicate other modes that should be studied for effect on HSA LCF life.

Experimental Effort

Stability of PICS and HSHX emissivities.--The iridium PICS is surface-treated to increase its emissivity. The stability of the surface over long periods of time should be investigated since the PICS temperature is very strongly dependent upon its emissivity.

Similarly, the HSHX temperatures are dependent upon the heat exchanger surface emissivity. The reference design HSHX calls for an emissivity of 0.8; considerable surface treatment may be necessary to attain this emissivity. To ensure that the HSHX temperatures do not exceed the requirements during the BIPS operating life, the stability of the surface must be ascertained.

HSIS heat transfer correlations.--The representation of heat transfer through the insulation could be improved. Data are especially needed for heat transfer through foils where the cold end is well above ambient temperature. An improved correlation also is necessary to account for the edge losses through the insulation joints.

PICS temperature measurement.--Direct measurement of the PICS temperature is necessary to confirm the thermal model of the IHS. Since the model is the same for steady-state and transient (including ECS) conditions, steady-state experimental results would suffice to confirm the PICS temperature prediction for all operating conditions. The IHS could be used by itself, with carefully defined boundary conditions and axial measurements of the PICS and ablation sleeve temperatures.

Structural verification.--In addition to the normal acceptance-type tests, specific testing should be performed to confirm the dynamic response and capability of the HSA and HSHX. In particular, the amplification of dynamic loads at the HSHX mount points is an important area of investigation.

SUMMARY OF RESULTS

The following itemized remarks summarize the results of the study:

(1) A Hastelloy X single-tube helical coil was selected as the design for the heat source heat exchanger (HSHX) for the Brayton isotope power system (BIPS). The material and configuration emphasizes reliability and fabricability.

(2) The feasibility of fabricating this design has been demonstrated. A heat exchanger of this configuration has been manufactured for use in the BIPS ground demonstration system under a DOE contract.

(3) The single-tube helical-coil design has been optimized with respect to weight, pressure drop, and working fluid outlet temperature. The optimized heat exchanger is a 10-turn coil made of a 3.96-cm (1.56-in.) OD and 3.703-cm (1.458-in.) ID tube. The surface should be treated to an emissivity of 0.8.

(4) The HSHX meets the steady-state performance requirements. The temperature requirements for the iridium post-impact containment shell (PICS) are not quite met. The PICS temperatures are within the required range for an HSHX surface emissivity of 0.25, the nominal value for untreated Hastelloy X.

(5) The auxiliary cooling system requirements can be met using neon as the fill gas. The neon fills the radiation gaps in the heat source assembly (HSA) and allows the heat to be transferred out of the HSA by conduction. Additional cooling of the HSA is required to meet a launch pad exposed surface temperature limitation. The PICS temperature requirements are not quite met for the reference HSHX, but are within the required range for an HSHX of 0.25 surface emissivity.

(6) The latest expected BIPS startup transient was used to predict temperatures, thermal stresses, and low-cycle fatigue life. The PICS temperatures are acceptable during the startup. The predicted fatigue life of the HSHX is 570 cycles, well over the system requirement of 100 cycles.

(7) The emergency cooling system performance is not sufficient to meet the PICS temperature requirements. Although the maximum allowable PICS temperature is not exceeded during the foil meltdown, an insufficient number of foils is melted to lower the ultimate post-meltdown PICS temperature to its required value. Analysis indicates that essentially all of the insulation foils must be removed to attain the required post-meltdown PICS temperature.

(8) With some minor modifications to the existing HSA structure, natural frequency and dynamic loading requirements can be met.

CONCLUDING REMARKS

This final report has presented the results of a study conducted by the AiResearch Manufacturing Company of California on the preliminary design of an alternate heat source assembly (HSA) for a Brayton isotope power system (BIPS). In particular, the HSA is intended for use on the BIPS now under development by the AiResearch Manufacturing Company of Arizona under a Department of Energy contract.

The heat source heat exchanger (HSHX) design for the HSA has been selected and optimized. The auxiliary cooling system has been investigated, and neon recommended for the HSA fill gas. Low-cycle fatigue life requirements are easily attained for the HSHX. Natural frequency and dynamic loading requirements can be met for the HSA.

The major problem area remaining for the HSA is the emergency cooling system (ECS) performance. An insufficient number of insulation foils is melted to lower the temperature of the iridium post-impact containment shell to an acceptable value.

Recommendations for future analytical and experimental work, with emphasis on the ECS problem, have been made. A layout drawing has been prepared for the HSA.

APPENDIX A

STEADY-STATE AND TRANSIENT THERMAL ANALYZER PROGRAM WITH COMPRESSIBLE AND INCOMPRESSIBLE PRESSURE DROP

Program Capabilities

This program, known as AiResearch thermal analysis program H0910, has the following capabilities.

Transient heat transfer calculations.--Transient heat transfer calculations are developed by an explicit finite-difference technique using an element shape with three-dimensional conduction, convection, or radiation heat transfer.

Steady-state heat transfer calculations.--Steady-state heat transfer calculations are based on a modified Gauss-Seidel solution to the simultaneous equations in the thermal model. This modified technique involves "accelerated" step substitution with monotonic deceleration until successive substitutions are convergent. A method of "lumping" areas of the problem that are slow to converge is also used to accelerate the calculation procedure. This procedure also provides for any element shape with three-dimensional conduction, convection, or radiation heat transfer.

Conduction heat transfer calculations.--Conduction heat transfer is input to the program by specifying the element numbers connected by conduction, the cross-sectional area for conduction between the elements, and the conduction length from the center of each element to the interface between them. A mechanical joint thermal contact resistance also may be specified between the elements if they are mechanically separated at the interface. The program obtains the thermal conductivity of each element from a table in which it may be specified as a constant value or as a function of temperature.

Convection heat transfer calculations.--Convection heat transfer is input to the progrm by specifying a solid element number connected to a fluid element number by convection, the cross-sectional area for convection from the solid element, and the conduction length from the center of the solid element to the convection surface. This program performs the important and often overlooked task of combining conduction heat transfer from the center of the solid element to the surface with convection from the solid surface to the fluid..

The convection heat transfer coefficient may be input to the program by nine different methods. In the first four methods, the heat transfer coefficient may be input as a constant, as a function of time in a table, as a function of the surface-to-fluid temperature difference in a table, and as a function of the "film" temperature in a table. In method five, the program calculates the natural convection heat transfer coefficient for both open and enclosed static spaces and enclosed rotating spaces. In method six the program calculates convection heat transfer coefficients for high-speed laminar or turbulent flow over external surfaces including the effects of the boundary layer. In method seven the program calculates convection heat transfer coefficients on

a free or enclosed rotating disc including the calculation of frictional "windage" heat generation. In method eight the program calculates jet impingement heat transfer coefficients for impingement from a row of holes onto a concave surface. In method nine the program calculates convection heat transfer coefficients for flow in a duct, including the heat transfer "fin effectiveness" of extended surfaces within the duct. The method utilizes tables of Colburn J-factors input as a function of Reynolds number to the program. These tables may be generated for fluid flow in round ducts, square ducts, rectangular ducts, triagular ducts, annular spaces, dimpled tubes, and curved ducts. They also may be generated for fluid flow in tube banks, plate-fin surfaces, pin-fin surfaces, screen matrix surfaces, crossed rod matrix surfaces, and corrugated ceramic surfaces. Entrance effects on heat transfer may be applied using the appropriate multiplying factor at each location. Four techniques for evaluation of the influence of temperature-dependent fluid properties are available in the program. The appropriate fluid properties may be input in tabular form as a function of temperature.

Radiation heat transfer calculations.--Radiation heat transfer is input to the program by specifying a solid element number connected to a representative surrounding element number by radiation, the cross-sectional area for radiation from the solid element, and the conduction length from the center of the solid element to the radiation surface. This section also includes the important combination of conduction to the radiation surface with radiation from the surface. The emissivity view factor for radiation may be estimated by methods given in "Radiation Heat Transfer" by Sparrow and Cess or by a computer program such as CONFAC II.

Initial temperature, boundary conditions, heat input, thermal capacitance, and thermal conductivity specification.--The initial temperature, boundary conditions, heat input, thermal capacitance, and thermal conductivity may be specified for each individual element or for blocks of elements that are identical. In transient heat transfer calculation, the initial temperature, the heat input, the density, the volume, the specific heat, and the thermal conductivity of each element is specified. For elements with negligible thermal capacitance the density, volume, and specific heat may be left blank to increase the calculation time step. For steady-state calculations, the initial temperature, the heat input, and the thermal conductivity of each element are specified. The boundary condition elements are specified by having a negative value for the density times the volume. This element is then maintained at a constant temperature or may be specified as a temperature versus time function from an input table. Any element in the network may be specified as a boundary condition (constant temperature) element and any number of elements may be connected to it by conduction, convection, or radiation. The heat input for each element may be input as zero, as a constant value, as a function of time in a table, as a function of its own temperature or another specified element temperature, specified from the frictional "windage" heat generation calculations, or calculated from the ball and roller bearing heat generation calculation computer program which can be supplied. The specific heat and thermal conductivity of each element may be specified as a constant or as a function of temperature in tables.

Fluid stream heat transfer and pressure drop calculations.--Fluid stream elements may be input with heat transfer to them by conduction, convection, or radiation. Fluid stream heat transfer calculations have provisions for preventing the outlet fluid temperature from "overshooting" the surrounding surface temperatures, a thermodynamic impossibility. The steady-state fluid stream calculations are based on thermal capacity rate calculations, while transient fluid stream calculations may be based on the thermal capacitance of each element moving in the fluid stream to simulate "lag" conditions. The energy input of rotational flow may also be added to the fluid stream.

Both steady-state compressible and incompressible fluid stream pressure drops may be calculated by the program. The pressure drop calculations include the effects of heat addition, area change, fluid friction, rotational flow, and flow addition or removal. Total head losses due to valves, bends, sharp contractions or expansions, and orifices may be included at the inlet and exit to each fluid stream.

A complete fluid stream network may be simulated with streams branching from previous streams and mixing to form new streams or even returning to a previous stream in the network. The fluid flow rate may be input as a constant, as a function of time, from a table, or as a function of specified element temperature.

Program Output

The following outputs may be obtained:

(1) Each element temperature, heat input, and thermal conductivity for steady-state calculations is printed out. Each element temperature, heat input, weight, specific heat, and thermal conductivity for each specified printing time period in transient heat transfer calculations is printed out.

(2) The fluid stream inlet temperature and the outlet temperature, the fluid stream flow rate, the fluid density, and the internal fluid heat generation for each section of each fluid stream are printed out.

(3) The "free stream" temperature, the film discharge temperature, and the effective film temperature at each location specified are printed out.

(4) The printing of the thermal resistance values for conduction, the thermal resistance values and heat transfer coefficients for convection, and the thermal resistance values and effective heat transfer coefficients for radiation may be included or deleted as specified.

(5) The fluid stream pressure drop calculations and printout may be deleted if specified. When included, the total and static pressure, the Reynolds number, the friction factor, and the Mach number for compressible flow are printed for each element in each fluid stream.

Typical Applications

Typical applications include:

(1) Both passive and active electronic cooling system analysis and design with or without heaters or cooling flow controllers.

(2) Thermal analysis and design calculations for ambient-cooled, forced-air-cooled, gas-cooled, or liquid-cooled ac or dc motors, generators, and alternators.

(3) Thermal analysis and design calculations for pumps, fans, and compressors, including the bearing temperatures, and the analysis of the motors or turbines driving them.

(4) Thermal analysis and design calculations of gas turbine engines including the axial-flow and radial-flow compressors and turbines, the bearings and seals, the anti-icing system, the lubrication cooling system, the fuel sypply system, and the accessory area cooling system. Also, the thermal analysis of cooled and uncooled turbine blades.

(5) Transient and steady-state thermal analyses of heat exchangers including air-oil coolers, fuel-oil coolers, recuperators, rotary regenerators, cryogenic heat exchangers, pool boiling heat exchangers, condensers, periodic flow regenerators, and heat exchangers with more than two fluid streams. The calculations may include the effects of axial conduction, fluid bypassing, perfectly mixed or unmixed fluids, variation of fluid properties through the heat exchanger, condensation of moisture from the air or "wet" heat transfer, and the effect of the variation of fluid-to-wall temperature difference on local heat transfer coefficients for boiling and condensing.

APPENDIX B

U-FLOW MANIFOLD DESIGN COMPUTER PROGRAM, X1000

Program X1000 determines the best manifold sizes necessary to yield uniform flow through a heat exchanger core. The solutions are valid for oblique manifold systems, i.e., the supply and discharge flow directions are perpendicular to the flow direction through the core.

Because there are an infinite number of manifold area combinations that will yield uniform flow for a given core, one of the manifolds must be selected as input. Either the inlet or outlet may be chosen, with the remaining manifold area optimized. Either constant or varying area manifolds may be selected.

The pressure distribution along the core length of the given manifold is calculated. The other manifold is sized to yield an identical pressure profile. The calculations are based on a finite-element solution of the equations of motion. Either one- or two-dimensional solutions can be specified. Both compressible and incompressible calculations can be performed. Frictional losses in the manifolds can be included by the input of appropriate friction factor versus Reynolds number tables for each manifold.

Program input comprises the following:

Fluid properties

Manifold friction factor properties

Specification of options and convergence criteria

Definition of one manifold flow area and hydraulic radius as a function of manifold length

Mass flow rate, inlet and outlet temperatures and pressures

Program outputs comprise:

Design manifold definition - flow area and hydraulic radius as a function of manifold length

Difference in manifold pressure profiles as a function of manifold length

Maximum heat exchanger core pressure drop variation for the design solution

Manifold pressure losses

APPENDIX C

ANSYS (ENGINEERING ANALYSIS SYSTEM) COMPUTER PROGRAM

This program, a general-purpose finite-element computer program for stress and vibration analysis, was developed by and is maintained by Swanson Analysis Systems, Inc. The program contains more than 60 kinds of finite elements (such as beam, plane stress, axisymmetric solid and shell, general shell, and three-dimensional solid), 17 of which have nonlinear formulations, and includes the capability of performing static or dynamic analyses, fluid flow, and heat transfer. The nonlinear capabilities include plasticity (small strain), creep (thermal and radiation induced), radiation-induced swelling, large deflection, and buckling. Therefore, it has found wide application, particularly in the analysis of nuclear power reactors. The dynamic capabilities include eigenvalue-eigenvector, steady-state harmonic response, and linear and nonlinear transient response. The materials may be either isotropic or orthotropic and may include nonlinear temperature dependency.

REFERENCES

1. Srinivasan, P.S., Nandapurkar, S.S., and Holland, F.A.: Pressure Drop and Heat Transfer in Coils. The Chemical Engineer, no. 218, May 1968, pp. 113-119.

2. Srinivasan, P.S., Nandapurkar, S.S., and Holland, F.A.: Pressure Drop and Heat Transfer in Coils. The Chemical Engineer, no. 218, May 1968, pp. 113-119. (Original source: Kubair, V. and Varrier, C.B.S.: Trans. Indian Inst. Chem. Eng., vol. 14, 1961/62, p. 93.)

3. Mori, Y. and Nakayama, W.: Study on Forced Convective Heat Transfer in Curved Pipes. Int. J. Heat and Mass Transfer, vol. 8, no. 1, Jan. 1965, pp. 67-82.

4. Seban, R.A. and McLaughlin, E.F.: Heat Transfer in Tube Coils with Laminar and Turbulent Flow. Int. J. Heat and Mass Transfer, vol. 6, no. 5, May 1963, pp. 387-395.

5. Itō, H.: Friction Factors for Turbulent Flow in Curved Pipes. Trans. ASME, J. Basic Eng., vol. 81, June 1959, pp. 123-134.

6. Anon.: Aerospace Fluid Component Designers' Handbook. TRW Rept. no. RPL-TDR-64-25, vol. 1, Feb. 1970, p. 3.9.2-4.

7. Anon.: Meltdown Analysis of Multi-Foil Assemblies. Thermo Electron Corp. Rept. no. 4219-65-77, Dec. 1976.

8. Anon.: NASA TM X-71895, 1976.

9. Moon, D.P., Simon, R.C., and Favor, R.J.: The Elevated-Temperature Properties of Selected Superalloys. ASTM Data Series DS 7-S1, 1968.

10. Anon.: Design Study of an Alternate Heat Source Heat Exchanger for the Brayton Isotope Power System. AiResearch Manufacturing Company of California Rept. no. 78-15009, May 1978.

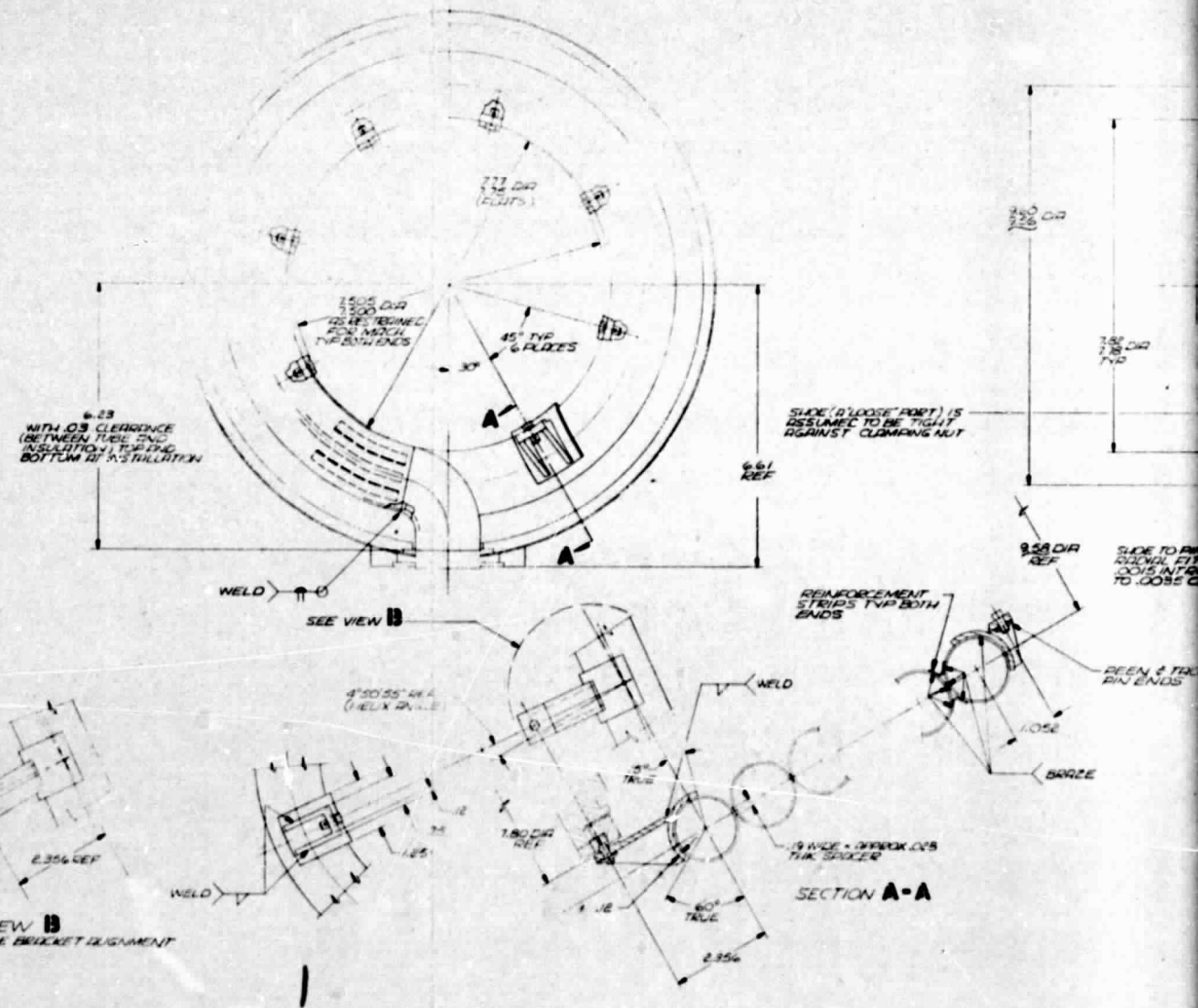

FOLDOUT FRAME

FOLDO

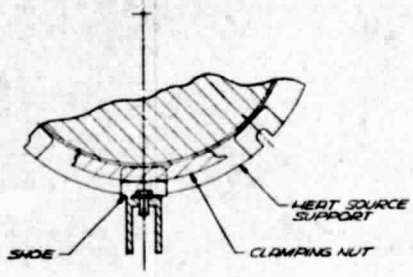

SECTION **D-D**
TYP 7 PLACES

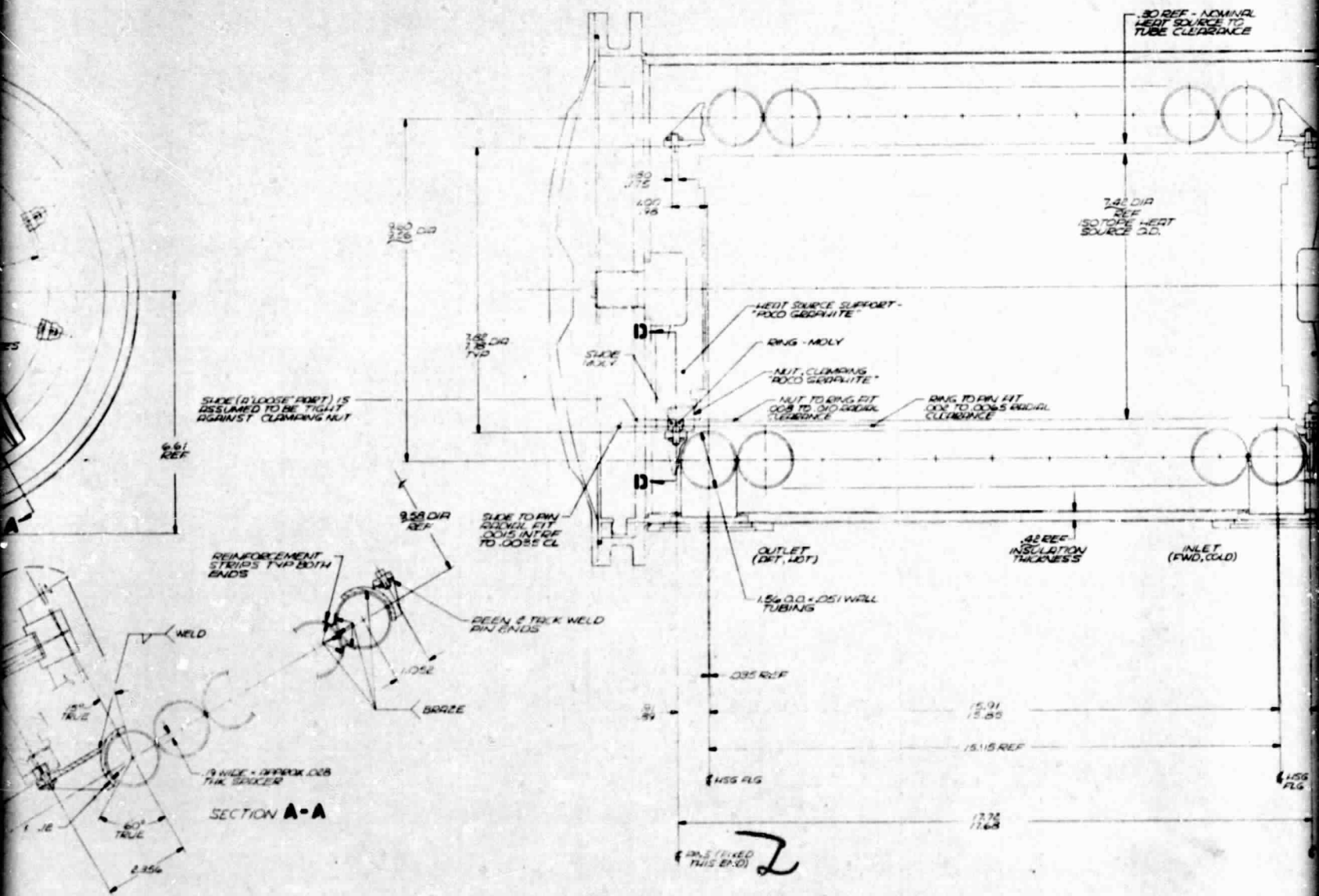

FOLDOUT FRAME

ORIGINAL PAGE IS
OF POOR QUALITY

FOL

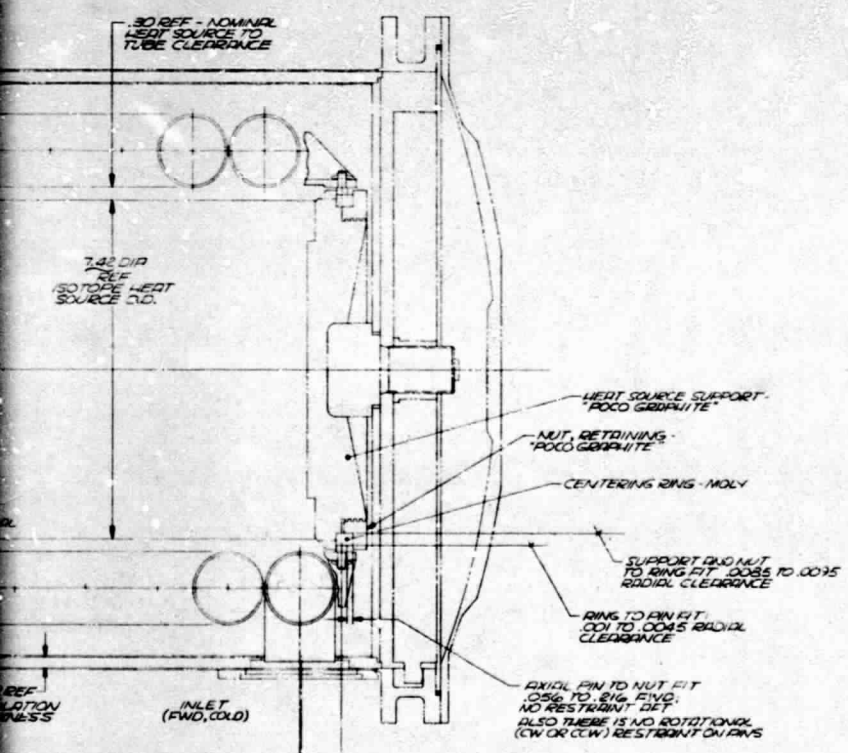

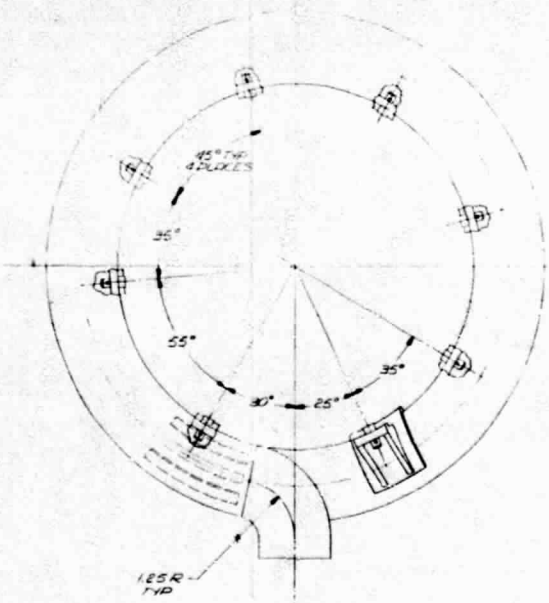

7 UNIT IS PRESSURE TESTED PRIOR TO LEAK TEST TO 365 PSIA AT ROOM TEMPERATURE.

6 LEAKAGE WILL NOT EXCEED 6×10^{-10} SCC/SEC OF HELIUM AT ROOM TEMPERATURE AND ATMOSPHERE DELTA PRESSURE

5 IDENTIFICATION AND TRACEABILITY IS REQUIRED. LOT CONTROL IS ESTABLISHED FOR RAW MATERIAL.

4 ALL WELD AND BRAZE JOINTS ARE RADIOGRAPHIC INSPECTED PER MIL-STD-453

3 ALL WELD AND BRAZE JOINTS ARE VISUALLY INSPECTED UNDER 20 X MAGNIFICATION

2 HEAT EXCHANGER FABRICATED ENTIRELY FROM HASTELLOY 'X'. EXTERNAL SURFACE TREATED TO INCREASE EMISSIVITY (ROUGHENED BY GRIT BLASTING FOLLOWED BY HEATING IN AIR TO OXIDIZE SURFACE)

1 ALL FITS CALCULATED AT ROOM TEMPERATURE

NOTES: UNLESS OTHERWISE SPECIFIED

3

FOLDOUT FRAME

Fig

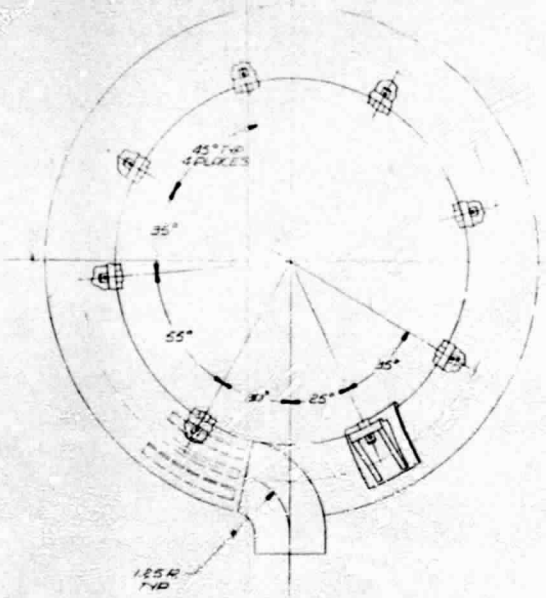

7 UNIT IS PRESSURE TESTED PRIOR TO LEAK TEST TO 365 PSIA AT ROOM TEMPERATURE

6 LEAKAGE WILL NOT EXCEED 6×10^{-10} SCC/SEC OF HELIUM AT ROOM TEMPERATURE AND ATMOSPHERE DELTA PRESSURE

5 IDENTIFICATION AND TRACEABILITY IS REQUIRED. LOT CONTROL IS ESTABLISHED FOR RAW MATERIAL

4 ALL WELD AND BRAZE JOINTS ARE RADIOGRAPHIC INSPECTED PER MIL-STD-453

3 ALL WELD AND BRAZE JOINTS ARE VISUALLY INSPECTED UNDER 20 X MAGNIFICATION

2 HEAT EXCHANGER FABRICATED ENTIRELY FROM HASTELLOY X. EXTERNAL SURFACE TREATED TO INCREASE EMISSIVITY (ROUGHENED BY GRIT BLASTING FOLLOWED BY HEATING IN AIR TO OXIDIZE SURFACE)

1 ALL FITS CALCULATED AT ROOM TEMPERATURE

NOTES: UNLESS OTHERWISE SPECIFIED

LAYOUT

HEAT SOURCE HEAT EXCHANGER, BIPS-HSA

70210 L/97509

Figure 34. HSA Design Layout Drawing.